Crystallization phenomena in germanium antimony phase-change films

Gert Eising

Zernike Institute PhD thesis series 2013-24
ISSN: 1570-1530
ISBN: 978-90-367-6626-5 (printed version)
ISBN: 978-90-367-6625-8 (electronic version)

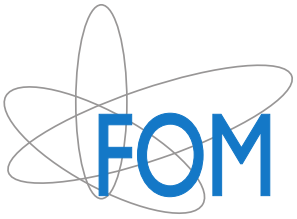

This research was carried out under project number M62.7.08SDMP03 in the framework of the Industrial Partnership Program on Size Dependent Material Properties of the Materials innovation institute M2i (www.m2i.nl) and the Foundation of Fundamental Research on Matter (FOM) (www.fom.nl), which is part of the Netherlands Organisation for Scientific Research (www.nwo.nl).

university of groningen / faculty of mathematics and natural sciences / zernike institute for advanced materials

The work presented in this thesis was performed in the Nanostructured Materials and Interfaces research group at the Zernike Institute for Advanced Materials of the Rijksuniversiteit Groningen, The Netherlands.

rijksuniversiteit
groningen

Crystallization phenomena in germanium antimony phase-change films

Proefschrift

ter verkrijging van het doctoraat in de
Wiskunde en Natuurwetenschappen
aan de Rijksuniversiteit Groningen
op gezag van de
Rector Magnificus, dr. E. Sterken,
in het openbaar te verdedigen op
vrijdag 13 december 2013
om 12:45 uur

door

Gert Eising

geboren op 30 augustus 1986
te Meppel

Promotor:	Prof. dr. ir. B.J. Kooi
Copromotor:	Dr. G. Palasantzas
Beoordelingscommissie:	Prof. dr. A.L. Greer Prof. dr. B. Noheda Pinuaga Prof. dr. ir. P.R. Onck

Voor pa en ma

Contents

Chapter 1

Introduction

Abstract. Phase-change materials have been intensively studied since the beginning of the 1960s and have seen many developments in the areas of scientific progress and industrial applications. These developments were strongly linked to the progress in (sub)micron and nanotechnology. The goal of this chapter is to provide insights into the achievements within the last 50 years. An overview will be given of the remarkable properties of phase-change materials, which made them very suitable as active media in rewritable optical disks, well-known from the CD, DVD and Blu-ray Disk formats, and makes them excellent candidates for replacing flash-memory in the near future. At the end of the chapter an outline of this thesis is given.

1.1 Phase-change materials

1.1.1 History

The first mentioning of a material with electrical phase-change properties is found in an article by Waterman in 1923. [1] While his work was focused on the thermionic emission of molybdenite (MoS_2), a large negative coefficient of resistivity was found during heating, as well as a threshold level for conduction when heated using an electric current; typical properties of currently used phase-change materials. As the digital computer had yet to be invented, no digital memory application was associated with these first findings. After the invention of the electronic computer in the 1939 by Atanasoff, the junction transistor in 1948 [2] and the integrated circuit in 1958 [3] the limit of memory devices was quickly reached and a faster, smaller and more reliable way of non-volatile computer memory was needed. Several new techniques were investigated. Chalcogenide materials, alloys with, in general, elements from group 16 from the periodic table (of which S, Se and Te are nowadays commonly used in phase-change materials), proved to be good candidates. The ability to switch was reported for AsTeI in 1962. [4]

In 1968 Ovshinsky published a paper demonstrating a reversible switching memory cells with a $Te_{48}As_{30}Si_{12}Ge_{10}$ composition. [5] Based on this alloy Shanefield built the first working memory device including a controlling circuit for reliable cell programming. [6] Promising memory devices were developed by several groups: a 16x16 array by Neale and Moore in

1970 [7] and a 1024-bit device in 1978 by Shanks and Davis. [8] However, due to the large phase-change cell sizes, the memories devices had a high power consumption compared to the competing techniques. This, combined with data reliability problems, resulted in a loss of interest in phase-change memories and halted the research for memory applications. It would take about 20 years before phase-change materials were found again in commercial memory devices.

In 1982 the Compact Disk-Read Only Memory (CD-ROM) was introduced. A memory where data is stored on a disk in a spiral track using reflective bumps and non-reflective holes. Using an infrared (780 nm) laser diode this difference in reflectivity is measured and zeros and ones are represented. The only-once recordable CD-R was introduced in 1988 and allowed to write marks in a photo-sensitive dye using a laser diode with a higher output power. Once the information has been written it could not be erased again. The development of rewritable CDs started shortly after the introduction of the CD-ROM [9, 10] but it took till 1997 before the CD-RW was commercially introduced. In the CD-RW a layer of phase-change material acts as the data layer. Initially in a crystalline state, amorphous marks, with a different reflectivity than the crystal phase, can be written in the data layer by locally melting the phase-change material with a short laser pulse. Rapid cooling causes this liquid state to be frozen, resulting in a melt-quenched amorphous mark. If the mark is heated again using a longer laser pulse, but with a lower laser power, the amorphous mark recrystallizes. Advancements in data capacity were mostly gained by moving to a shorter laser wavelength (650 nm for DVD and 405 nm for Blu-ray) and increasing the numerical aperture of the employed lens, resulting in smaller marks. By using double layered discs the capacity was further increased from ~780 MB to ~50 GB.

With the enhancements in lithography, especially the reduction in minimum feature size, electrical phase-change memory (PCM) became of interest again in the early 2000s. Based on phase-change compositions used for DVD±RW (mainly $Ag_5In_5Sb_{60}Te_{30}$), [11] new alloys were developed suitable for fast electric cells. The first commercial available memories arrived in 2008 [12] and are now used, although still on a small scale, in mobile phones. [13] Additionally germanium-doped antimony based alloys are becoming more popular and look like good candidates for future devices. [14, 15]

1.1.2 Remarkable properties

Phase-change materials based on (doped) germanium, tellurium and antimony alloys show some truly remarkable properties suitable for memory purposes. The large change in optical contrast between the amorphous and crystalline phase can be easily detected, which is why they are widely employed for the application in rewriteable optical media, like CD-RW, DVD±RW

and Blu-ray RE. For electrical memories the large difference (several orders of magnitude) in electrical conductivity between the amorphous and crystalline phase is exploited to store information.

The usability of phase-change materials in a memory device originates from several favorable properties. The first is the low energy needed to switch between the amorphous and crystalline phase. Heating to a temperature above the glass transition temperature, ~150 °C [16] for the commonly used phase-change material $Ge_2Sb_2Te_5$, is enough for fast crystallization. Switching to the amorphous phase needs heating to above the melting temperature, which is relatively low for $Ge_2Sb_2Te_5$(~600 °C). In optical discs the heating is provided by a laser pulse, a (semi-transparent) heat-absorption layer is present to provide enough cooling for freezing the liquid phase into a solid amorphous phase (melt-quenching). In electric memory devices the phase-change cells are heated by exploiting Joule heating: the current flowing through the cell when a voltage is applied over the cell will heat the phase-change material to the desired temperature. When the cell is in the crystalline phase, and thus in the low resistance state of typically several kΩs, a short voltage pulse is already enough to melt the cell and quench it in the amorphous phase afterwards. For a typical line-cell it has been shown that a pulse with a 30 ns pulse width and an amplitude of 1.4 V will amorphize the phase-change cell. [17] To crystallize the amorphous cell a lower temperature is needed, between the glass transition temperature and melting temperature. However, due to the high resistance state of the cell, typically ~100 kΩ–10 MΩ, a much higher voltage, with respect to the crystalline cell, would be needed to generate a current that is high enough. The reason phase-change materials remain useable is due to the threshold switching behavior they exhibit. When a sufficient large electric field is applied over the amorphous cell the electrical resistance will drop significantly, allowing a large enough current to flow that will heat the cell above the glass transition temperature. [18, 19] A pulse width of 30 ns with an amplitude of ~1.1 V is enough to crystallize a typical line-cell. [17] It has already been shown that phase-materials are able to switch to the crystalline state with even shorter pulses of 1–30 ns. [20] These short electrical pulses are sufficient, because of the extreme crystallization speeds of more than a few meters per second that are possible in phase-change materials. Amorphization can be done even faster, and it has been shown that femtosecond pulses are able to amorphize a crystalline $Ge_2Sb_2Te_5$-film. [21]

The second property, making phase-change materials suitable for memory applications, is the capability to switch at a short time scale between the two phases, while at the same time both phases are stable for a long time at operational temperatures. The short pulses used for switching are in strong contrast with the retention time of the amorphous phase at operational temperatures (maximum 80 °C for consumer products). Current materials are stable for more than 10 years (more than 15 orders of magnitude higher than the switching time!) at these

temperatures before losing their information due to unwanted crystallization.

Apart from being stable at elevated temperatures, it is also important that the phase-change cells are able to switch often, while remaining reliable. For optical applications, like CD-RW and DVD±RW, the phase-change materials can be switched up to 1000 times. Electrical phase change memories have already been switched up to 10^{11} times. [22] The PCM cells fail when they get stuck in either one of the two states and are unable to switch back under normal writing conditions. Set-stuck, when the cell stays crystalline, is typically caused by compositional (stoichiometric) changes. Reset-stuck, the cell stays amorphous, is typically caused by void formation. The high electric field needed to switch a phase-change cells induces electric field- or current-induced atomic transport and electromigration which in turn cause compositional changes and void formation. [23] The compositions of the phase-change materials are crucial for their functionality. Changing the composition with only several percent will already change the crystallization properties significantly. This will also be shown in chapter 3.

1.1.3 Memory applications

The next step for phase-change memory is the commercial application in electric solid state memory devices. Compared to traditional hard disk drives (HDDs), which employ a thin ferromagnetic film for data storage, PCM memories are faster due a reduced access time and higher data throughput, and provide true random access. Additionally, a HDD uses mechanical parts, for spinning the magnetic disks and moving the read and writing heads, which can cause mechanical wear. For mass storage a HDD is still preferable as the price per GB is still favorable due to the lower production costs per GB.

Flash memories (in particular NOR flash) will be most likely replaced sooner than HDDs by PCM. Both Flash and PCM technologies provide a solid state memory solution. However, PCM has some significant benefits. Flash memory derives its name from the writing method it employs: it "flashes" whole blocks when erasing data as it cannot write and erase a single cell at a time. PCM does not have this drawback and provides much faster bit-wise programming and reading. Additionally, PCM has lower latency and higher writing and erasing speeds; [24] and also provides better downscaling of the phase-change cell size than the flash cells. Where for flash memory the programming of the cell becomes more difficult with decreasing sizes and reaches fundamental limits soon, [25, 26] it has been shown for PCM that the cells remain switchable and that, additionally, the programming currents also go down. [27] However, flash memory can write many bits parallel due to its low power consumption. If PCM wants to be really competitive to flash memory the power requirements of PCM need to be reduced.

Next to replacing non-volatile memories, it might be possible to replace the volatile dy-

namic random-access memory (DRAM) with PCM. Currently, PCM already has a similar latency and write speeds as DRAM. [24] Moreover, DRAM is reaching its limits in scalability at a feature size of ∼30 nm while PCM remains scalable below ∼10 nm and is capable of having a smaller feature size when using diode switches. [28] Additionally, PCM is a more energy efficient technology than DRAM which, inherent to its reading and writing procedures, requires relatively much energy. [19] It has been demonstrated for single cells that the endurance of PCM (the amount of times a cell can switch between the crystalline and amorphous phase) can match that of DRAM. [29] Large scale PCM devices currently reach $\sim 10^8$ cycles, which will result in an estimated lifetime of the PCM devices of 5 to 6 years, [30] whereas DRAM has a practical infinite lifetime.

In conclusion, the scalability and fast switching times makes phase-change memories an excellent replacement for current hard disks and solid state drives solutions. If the endurance and reliability can be further improved it can also replace DRAM in the future to form a universal memory. This would additionally require new software architectures and memory concepts as the traditional boundary between RAM and data storage will fade.

1.1.4 Germanium-doped antimony alloys

The research presented in this thesis was started with the aim to investigate (the presence of) so-called explosive crystallization (EC) phenomena in phase-change films. Upon crystallization of the amorphous phase, induced by an external energy source, the entropy decreases as the system goes from the randomly ordered amorphous phase (high in configurational entropy) to the highly ordered crystalline phase (lower in configurational entropy). The latent heat released during crystallization can be used to create a self-sustaining crystallization process under certain conditions. This process is known as explosive crystallization (EC). The first report (from 1869) of explosive crystallization can be found for antimony layers with a thickness of "at least half a sixpence up to half an inch" (0.5 – 12.7 mm). [31] It was found that if these layers are "struck gently or rubbed" an explosion occurs with a flash of light and significant heat production. Later experiments showed the presence of explosive crystallization in films of other pure elements as silicon and germanium [32, 33] and (In,Ga)Sb alloys [34] where extremely fast crystal growth rates have been reported ($>10\,\mathrm{m\,s^{-1}}$). However, literature does not provide systematic experimental studies on EC in phase-change material alloys.

Explosive crystallization is not present in optical discs, as the heat absorption control layer present in these discs, needed to write the amorphous marks, is expected to prevent the occurrence of EC. Moreover, optical discs are in the crystalline phase before first usage, and therefore, EC would not reach neighboring amorphous marks. The initialization of an as-deposited

amorphous disc to the crystalline phase could possibly benefit from EC as it only would need a single energy pulse. In PCM applications each data bit is an individual cell embedded in SiO_2 and therefore explosive crystallization could be exploited to speed up the relatively slow crystallization process. Additionally, the energy requirements for crystallization can be lowered as only an initial energy pulse is needed to start the process, instead of continuously heating the cell until it has been crystallized. PCM cells are often embedded in poorly heat-conducting silicon oxide which may allow explosive crystallization to take place. To study these phenomena we choose to use Ge-doped and Ga-doped Sb-rich phase-change compositions. These alloys were selected as they are directly of interest in PCM applications and the pure elements all show explosive crystallization. [31–34] Antimony already shows EC at room temperature and is stabilized by germanium or gallium doping. A condition for explosive crystallization is that enough latent heat has to be locally released upon crystallization. Data found in literature often uses thick films (>1 μm) where enough latent heat is released for explosive crystallization. However, for application in PCM cells the phase-change films/cells have to be downscaled to the nanometer regime. Below a critical thickness explosive crystallization does not occur anymore. Therefore, we tested a range of film thicknesses (50 nm – 2000 nm) on the presence of EC. To initiate EC any energy pulse can be used. Reports have shown EC after a mechanical, electrical, electron beam or laser impulses. [33–36] The latter was used for our study. However, no explosive crystallization was found in both alloys for different film thicknesses and different compositions. However, the Ge-doped Sb alloys did exhibit many interesting crystallization and material properties, which we studied in more detail.

One of the initial experiments was the observation of the crystallization process in Ge_7Sb_{93} films with a thickness of 200 nm on a polycarbonate substrate. From previously obtained results we expected to find near isotropic crystal growth in the amorphous film. However, star-shaped crystals with an increased crystal growth rate of the tips were observed (∼5 times faster than expected from isothermal growth), see Fig. 1.1. Additionally, the amorphous surfaces show buckling parallel to the crystal tips. In the crystalline areas buckling perpendicular to the growth direction is observed. By further investigating the crystallization properties, as is done in chapters 3 and 5, we will be able to explain many details regarding the observed crystallization process in Ge-doped Sb films.

1.2 Thesis outline

This thesis can be divided into two parts. The first part, chapters 2 to 6, is concerned with the research on different crystallization properties and material properties of the used GeSb films with various thicknesses and compositions. A description of the measurement setup and

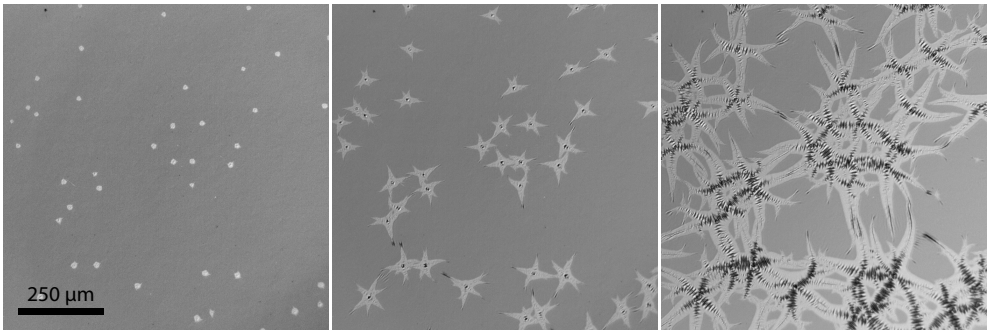

Figure 1.1 | Frames from an optical recording of crystallization in 200 nm thick Ge_7Sb_{93} phase-change films on a polycarbonate substrate at 180 °C. After initially isotropic growth, star shaped crystals form. The recording was taken at 60 frames per second. The time between the frames displayed here is 4.8 s.

techniques used for sample preparation and analysis is given in chapter 2. Chapter 3 focusses on the crystal growth during isothermal measurements. The effects of small changes in the phase-change composition on the growth rate, but also the crystal structure, are shown. Interestingly, for some compositions competing, i.e. simultaneously occurring growth modes have been observed. Using additional laser heating the crystal growth is studied at temperatures not available in isothermal experiments and the results are shown in chapter 4. Mechanical stresses play an important role in the small confined PCM cells. The effects of in-plane stresses on the crystal growth in thin films are investigated in chapter 5. The differences in surface potential between the crystalline and amorphous phase and the presence of a Schottky barrier on the crystalline-amorphous interface are scrutinized in chapter 6. Nucleation plays an important role in the phase-change process from amorphous to crystalline. In the second part, chapter 7, the growth and decay of the nuclei is studied within a two dimensional Ising model. Using Monte Carlo simulations and numerical enumerations of so-called lattice animals the critical nuclei needed for growth on square and triangular lattices are determined, compared and evaluated.

References

[1] A. T. Waterman, *Physical Review* **21**, 540 (1923).

[2] J. Bardeen, W. H. Brattain, *Physical Review* **74**, 230 (1948).

[3] J. S. Kilby (1967), Integrated semiconductive circuit structure, Patent, U.S. Classification: 327/220; 257/532; 257/539; 257/586; 257/724; 257/E21.537; 257/E27.038; 257/E27.039; 327/221; 327/565; 365/179.

[4] A. Pearson, W. Northover, J. Dewald, W. Peck Jr, *Advances in Glass Technology* **2**, 357–365 (1962).

[5] S. R. Ovshinsky, *Physical Review Letters* **21**, 1450 (1968).

[6] D. J. Shanefield (1969), Operating circuit for phase change memory devices, Patent, U.S. Classification: 327/583; 257/1; 315/133; 315/136.

[7] R. Neale, D. Nelson, G. E. Moore, *Electronics* **43**, 56–60 (1970).

[8] R. Shanks, C. Davis, A 1024-bit nonvolatile 15ns bipolar read-write memory, *Solid-State Circuits Conference. Digest of Technical Papers. 1978 IEEE International* (1978), vol. XXI, pp. 112–113.

[9] M. Chen, K. A. Rubin, R. W. Barton, *Applied Physics Letters* **49**, 502 (1986).

[10] N. Yamada, E. Ohno, N. Akahira, K. Nishiuchi, K. Nagata, M. Takao, *Japanese Journal of Applied Physics* **26S4**, 61 (1987).

[11] H. Iwasaki, M. Harigaya, O. Nonoyama, Y. Kageyama, M. Takahashi, K. Yamada, H. Deguchi, Y. Ide, *Japanese Journal of Applied Physics* **32**, 5241 (1993).

[12] Intel, STMicroelectronics (2008), Intel, STMicroelectronics deliver industry's first phase change memory prototypes, Press release, http://www.intel.com/pressroom/archive/releases/2008/20080206corp.htm.

[13] Micron Technology (2012), Micron extends portfolio of phase change memory for mobile devices, Press release, http://news.micron.com/releaseDetail.cfm?releaseid=726075.

[14] C. N. Afonso, J. Solis, F. Catalina, C. Kalpouzos, *Applied Physics Letters* **60**, 3123 (1992).

[15] Y. Hajime, I. Hiroyuki, K. Yujiro, GeSbSnMn for high speed BD-RE media, *Phase Change Optical Information Storage* (2005).

[16] S. Raoux, J. L. Jordan-Sweet, A. J. Kellock, *Journal of Applied Physics* **103**, 114310 (2008).

[17] M. H. R. Lankhorst, B. W. S. M. M. Ketelaars, R. a. M. Wolters, *Nature Materials* **4**, 347 (2005).

[18] M. Wuttig, N. Yamada, *Nature Materials* **6**, 824 (2007).

[19] G. W. Burr, M. J. Breitwisch, M. Franceschini, D. Garetto, K. Gopalakrishnan, B. Jackson, B. Kurdi, C. Lam, L. A. Lastras, A. Padilla, B. Rajendran, S. Raoux, R. S. Shenoy, *Journal of Vacuum Science & Technology B: Microelectronics and Nanometer Structures* **28**, 223 (2010).

[20] G. Bruns, P. Merkelbach, C. Schlockermann, M. Salinga, M. Wuttig, T. D. Happ, J. B. Philipp, M. Kund, *Applied Physics Letters* **95**, 043108 (2009).

[21] J. Siegel, W. Gawelda, D. Puerto, C. Dorronsoro, J. Solis, C. N. Afonso, J. C. G. de Sande, R. Bez, A. Pirovano, C. Wiemer, *Journal of Applied Physics* **103**, 023516 (2008).

[22] A. Pirovano, A. Redaelli, F. Pellizzer, F. Ottogalli, M. Tosi, D. Ielmini, A. Lacaita, R. Bez, *IEEE Transactions on Device and Materials Reliability* **4**, 422 (2004).

[23] S. Lee, J.-h. Jeong, T.-S. Lee, W.-M. Kim, B.-k. Cheong, *IEEE Electron Device Letters* **30**, 448 (2009).

[24] W. J. Wang, L. P. Shi, R. Zhao, K. G. Lim, H. K. Lee, T. C. Chong, Y. H. Wu, *Applied Physics Letters* **93**, 043121 (2008).

[25] M. Kryder, C. S. Kim, *IEEE Transactions on Magnetics* **45**, 3406 (2009).

[26] O. Zilberberg, S. Weiss, S. Toledo, *ACM Computing Surveys* **45**, 29:1–29:33 (2013).

[27] S. Raoux, G. Burr, M. Breitwisch, C. Rettner, Y. Chen, R. Shelby, M. Salinga, D. Krebs, S.-H. Chen, H. L. Lung, C. Lam, *IBM Journal of Research and Development* **52**, 465 (2008).

[28] K.-J. Lee, B.-H. Cho, W.-Y. Cho, S. Kang, B.-G. Choi, H.-R. Oh, C.-S. Lee, H.-J. Kim, J.-m. Park, Q. Wang, M.-H. Park, Y.-H. Ro, J.-Y. Choi, K.-S. Kim, Y.-R. Kim, I.-C. Shin, K.-w. Lim, H.-K. Cho, C.-H. Choi, W.-r. Chung, D.-E. Kim, Y.-J. Yoon, K.-S. Yu, G.-T. Jeong, H.-S. Jeong, C.-K. Kwak, C.-H. Kim, K. Kim, *IEEE Journal of Solid-State Circuits* **43**, 150 (2008).

[29] I. S. Kim, S. Cho, D. H. Im, E. H. Cho, D. H. Kim, G. Oh, D. Ahn, S. Park, S. Nam, J. Moon, C. Chung, High performance PRAM cell scalable to sub-20nm technology with below 4F2 cell size, extendable to DRAM applications, *2010 Symposium on VLSI Technology (VLSIT)* (2010), pp. 203–204.

[30] B. C. Lee, E. Ipek, O. Mutlu, D. Burger, *SIGARCH Comput. Archit. News* **37**, 2–13 (2009).

[31] G. Gore, *Philosophical Magazine Series 4* **9**, 73 (1855).

[32] M. O. Thompson, G. J. Galvin, J. W. Mayer, P. S. Peercy, J. M. Poate, D. C. Jacobson, A. G. Cullis, N. G. Chew, *Physical Review Letters* **52**, 2360 (1984).

[33] T. Takamori, R. Messier, R. Roy, *Journal of Materials Science* **8**, 1809 (1973).

[34] C. Wickersham, G. Bajor, J. Greene, *Solid State Communications* **27**, 17 (1978).

[35] V. D. Das, P. J. Lakshmi, *Physical Review B* **37**, 720 (1988).

[36] O. Bostanjoglo, G. Schlotzhauer, *Physica Status Solidi (a)* **68**, 555–560 (1981).

Chapter 2

Experimental techniques

Abstract. This chapter describes the general experimental and analytical techniques we used to produce the samples, measure material and crystallization properties of the phase-change films and analyze the results. The methods mentioned here will serve as a base for the experiments performed in the next chapters. Deviations from the standard experimental practice and the additional instruments used will be mentioned in each chapter separately.

2.1 Sample preparation

The samples used for the experiments described throughout this thesis, consist of a 200 nm thick phase-change film with a Ge_xSb_{100-x} composition (with $x = 6$, 7, 8, 9, 10 and 11) on a 1.3 mm thick 30 mm × 30 mm glass substrate or on a polycarbonate disc. A schematic overview of a sample is depicted in Fig. 2.1. The phase-change films were deposited using co-sputtering with a Unaxis Sputter coater. This was done simultaneously on both substrates with a deposition rate of 2.5 nm s^{-1}. To prevent oxidation of the phase-change film, all the phase-change films were, without breaking the vacuum, directly capped with a 5 nm layer of $ZnS{-}SiO_2$. The composition was selected by varying the powers for the germanium and antimony targets. For Ge_7Sb_{93} and Ge_9Sb_{91} additional film thicknesses were deposited: 50 nm, 100 nm, 400 nm and 800 nm. The same deposition speed and capping layer were used for these films.

To be able to cut the samples with a glass substrate into smaller pieces, the films were coated with a thin (∼µm) layer of PMMA, after which the glass plates were cut into 5 mm × 5 mm samples using a diamond-tipped glass cutter. After cutting, the PMMA layer was removed by rinsing the samples in acetone and then rinsing the samples in isopropyl alcohol. The isopropyl alcohol was removed from the surface by blow-drying using nitrogen.

The polycarbonate discs were cut into smaller samples using a tungsten hot-wire. Due to the melting temperature of polycarbonate being between ∼220 and ∼260 °C, [1] in the same range as the crystallization temperatures of the phase-change materials (see chapter 3), crystallization of the phase-change film occurred at the edges of the samples while cutting. Therefore, it was made sure that the samples were large enough and the crystallization experiments in

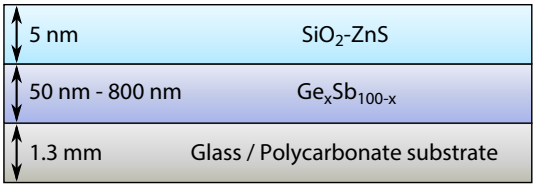

Figure 2.1 | Schematic layout of the samples used. With $x = 6, 7, 8, 9, 10$ and 11.

these samples were observed in the center of these samples, eliminating the influences of the crystals already formed at the edges and possible annealing of the sample on the crystallization properties.

2.2 Measurement setup

The crystallization in the phase-change films was observed using a Photron Fastcam 1024 PCI high-speed optical camera with a Navitar Zoom 6000 objective. The objective was extended with a 3 mm fine focus and a light source input for coaxial illumination. The latter allows for direct lightning of the sample. Direct lightning is crucial for observing crystals in an amorphous film, as it greatly enhances the contrast due to the specular nature of the observed films.

Samples were placed on a Watlow Ultramic 600 ceramic heater, capable of heating the sample up to 400 °C with a maximum ramp rate of 100 °C s^{-1}. The hot plate is mounted in an aluminum holder which is placed on insulating Teflon legs on a stack of three Standa 8MT167-25LS motorized translation stages for X–Y movement.

For writing crystalline marks in the amorphous films, and to locally induce additional heating in the phase-change film, a 100 mW 640 nm diode laser (OBIS 640LX) is used. Different optics are installed allowing the laser to be focused to a sub-micrometer spot for writing and erasing marks, as well as heating the film in an elliptical area with radii of $a \approx 250\,\mu m$ and $b \approx 110\,\mu m$. In chapter 4 the laser setup will be described in more detail.

The whole setup is computer controlled using custom written software. This allows, for example, to simultaneously record the crystal growth and apply a laser pulse to the film. A PID algorithm is used to control the power supply of the hot plate and keeps the temperature stable within ± 0.1 °C. The images obtained from the high speed camera are all saved and analyzed offline as described in the next section.

2.3 Image Analysis

Due to the difference in optical contrast between the amorphous and crystalline phase, the crystal growth in phase-change film can be followed in great detail using the optical high speed camera. The crystal growth rate was obtained quantitatively by analyzing typically 100 – 300 images obtained from the optical recordings, based on a procedure developed by Oosthoek. [2] The processing of a typical isothermal measurement at a temperature of 110 °C for a 200 nm thick Ge_6Sb_{94} film is shown in Fig. 2.2. Figure 2.2a shows an unprocessed image as obtained from the optical recordings with the as-recorded optical contrast between the amorphous (gray) and crystalline (white) phases. From the unprocessed image the amorphous background is removed by subtracting an image recorded of the amorphous sample before crystal nucleation occurs (Fig. 2.2b). To clearly distinguish the crystal from the background a threshold level is calculated using a minimum cross entropy thresholding algorithm. [3] This creates a binary image (Fig. 2.2c) with 0 corresponding to the amorphous phase and 1 to the crystalline phase. Noise is removed from the tresholded image by binary open and close operations (Fig. 2.2d). Using Sobel edge detection, the crystalline-amorphous interfaces are determined. The steps in Figs 2.2a–e are repeated for each of the recorded images and the results for all recorded images are stored. The edges (amorphous-crystalline interfaces) found in all separate images are combined into one time mapping, where the pixels pertaining to each edge receive a value corresponding to the recording time of the image it originated from; see Fig. 2.2f. For displaying purposes, the number of interfaces shown is strongly reduced with their corresponding time in the color coding and 160 s between successive growth fronts. For this purpose they are also thickened to more than one pixel wide.

2.3.1 Uniform growth

Fitting a plane (typically a circle with a diameter of 8 pixels) to the nonzero data points around each pixel of the time mapping image gives us the derivative at each pixel, which is a direct measure of the inverse growth rate. By inversing each value, the crystal growth rate is obtained for each pixel (Fig. 2.2g). Note that the nonzero data points in Fig. 2.2f correspond to pixels that are on any of the growth fronts in the 100 – 300 images analyzed. The zero data points correspond to pixels that are in between successive growth fronts. These zero data points should not be included in the fitting procedure, because this would lead to errors in the growth rate values. In the growth rate image (Fig. 2.2g), it can also be verified whether the growth rate is constant in time or that a significant time dependence is present. For the displayed sample, apart from the singularities at the final edges and center of the crystals, a constant growth rate holds. A growth rate histogram is produced by combining all pixel values for the growth rate (Fig. 2.2h).

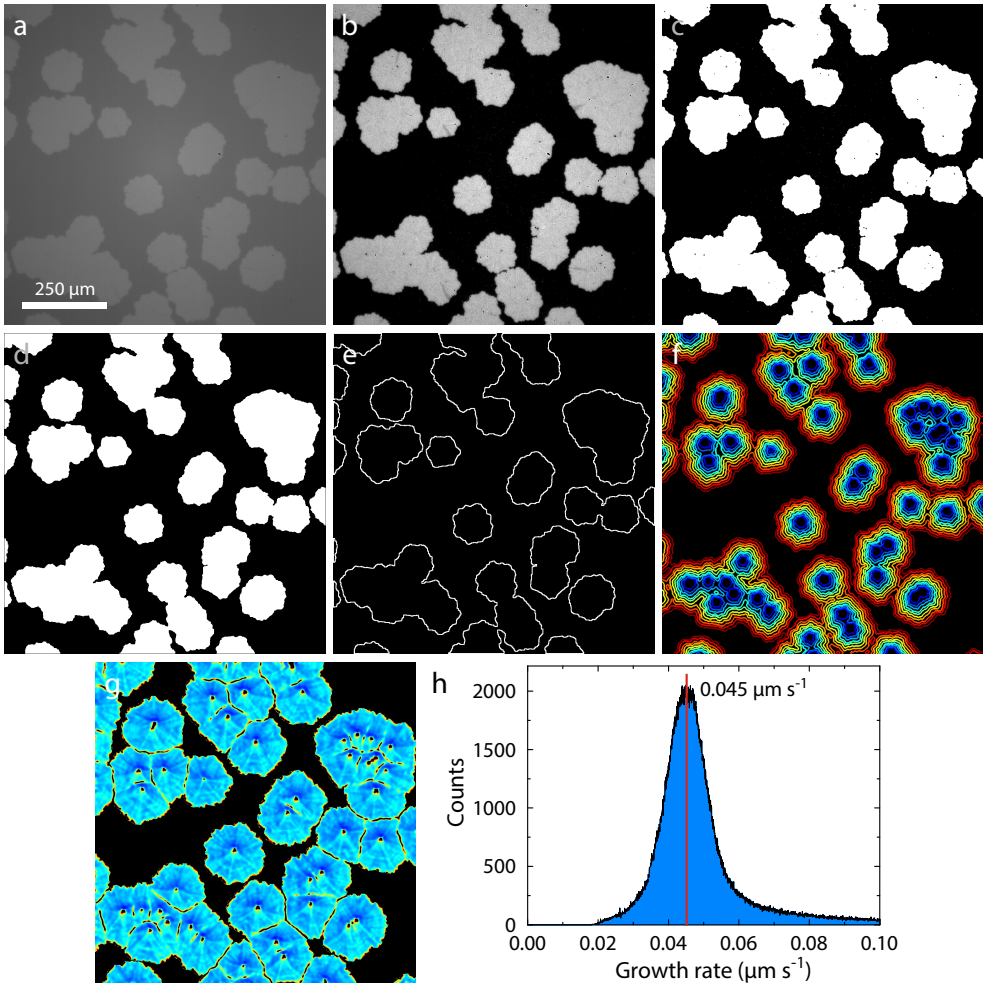

Figure 2.2 | Image analysis performed to obtain the time mapping and crystal growth rate from a series of images obtained using optical microscopy. **a** Example image showing the as-recorded contrast between the amorphous (dark gray) and crystalline (light gray) phases as obtained after isothermal crystallization. **b** The amorphous background is removed by subtracting an image recorded before the isothermal heating started. **c** Thresholding results in a binary image creating in a clear contrast between amorphous and crystalline. **d** Binary open and close operations are used to remove speckles and noise in the image and to close holes inside crystals. **e** Using edge detection the crystalline-amorphous interfaces is retrieved. **f** Time mapping of the crystalline-amorphous interface by combining the results of steps **a**–**e** for all recorded images (for displaying purposes, the number of interfaces shown is strongly reduced with 160 s between successive growth fronts, and they are also thickened to more than one pixel wide). **g** Growth rate mapping as obtained by applying planar fits (circles with a typical radius of 4 pixels centered on each pixel) to the time mapping. **h** Growth rate histogram obtained from the growth rate mapping.

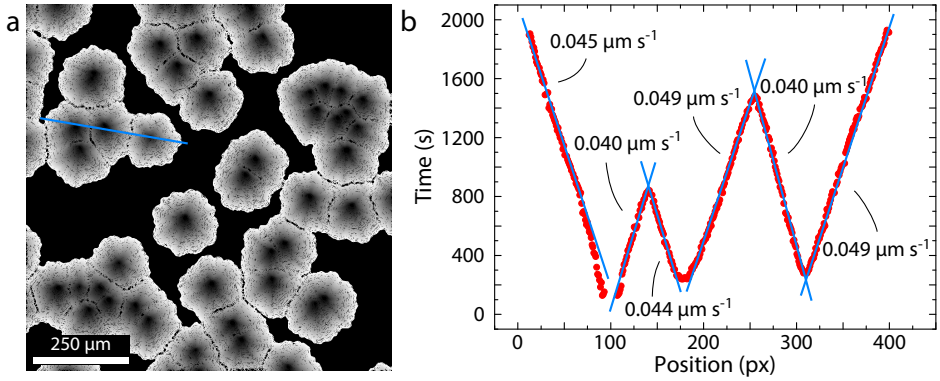

Figure 2.3 | Line profile analysis. **a** Time mapping showing at what time the crystalline-amorphous interface passed each position. The straight red line indicates the position where the line profile was taken. **b** Line profile (red circles) obtained from the time mapping in **a**, the slopes of the (blue) linear fits are the inverse speed of the crystalline-amorphous interface.

The growth rate pertaining to the most prevalent value in the histogram is considered the relevant growth rate for the crystallization process, 0.045 µm s^{-1} for this specific sample. The error for the growth rate is determined to be 5 % of the measured growth rate value.

2.3.2 Non-uniform growth

In cases where the crystal growth is not two dimensional, or strongly favors one direction, as will be shown in chapter 5, the growth rate is determined using an alternative method. The first steps are identical to the steps **a**–**f** displayed in Fig. 2.2. Instead of applying a two dimensional fit to the time mapping, as is done in step **g**, a line profile over a crystal is taken from the time mapping. Along the obtained data points, linear fits are applied from which the inverse growth rate is obtained from the slopes of the fits. When possible, this is done for multiple crystals and the obtained growth rates are averaged, as is shown in Fig. 2.3. In this case, we find an average of 0.44 ± 0.04 µm s^{-1}, close to the growth rate obtained using the histogram obtained from the growth rate mapping. The disadvantage of this method is the reduced statistics. However, it does work for all crystal shapes and gives the possibility to easily quantify non-uniform crystal growth rates.

References

[1] W. Martienssen, H. Warlimont, eds., *Springer Handbook of Condensed Matter and Materials Data* (Springer, 2005), Har/Cdr edn.

[2] J. L. Oosthoek, B. J. Kooi, J. T. De Hosson, R. A. Wolters, D. J. Gravesteijn, K. Attenborough, *Microscopy and Microanalysis* **16**, 291 (2010).

[3] C. Li, P. Tam, *Pattern Recognition Letters* **19**, 771 (1998).

Chapter 3

Isothermal crystal growth

Abstract. Analysis of crystal growth in thin films of phase-change materials can provide deeper insights in the extraordinary phase transformation kinetics of these materials excellently suited for data storage applications. In this chapter isothermal crystal growth in Ge_xSb_{100-x} thin films with $x = 6$, 7, 8, 9 and 10 is studied in detail, demonstrating that the crystallization temperature increases from ∼80 °C for Ge_6Sb_{94} to ∼200 °C for $Ge_{10}Sb_{90}$ and simultaneously the activation energy for crystal growth also significantly increases from 1.7 eV to 5.5 eV. The most interesting new finding is that in the thin films containing 8, 9 and 10 at.% Ge two competing growth modes occur, which can have several orders of magnitude difference in growth rate at a single external temperature: an initial mode with isotropic slow growth producing circular crystals with smooth surfaces and growth fronts and a fast growth mode producing crystals with triangular shape having rough surfaces and growth fronts indicative of dendritic-like growth. The slow-growth mode becomes increasingly dominant for crystallization at low temperatures when the Ge concentration is increased from 8 to 10 at.% Ge. For a certain Ge concentration the slow growth mode becomes increasingly dominant at lower temperatures and the fast growth mode at higher temperatures. Latent heat produced during crystallization is considered a principal factor explaining the observations. The fast growth mode is associated with (eutectic) decomposition generating more latent heat and instable growth fronts and the slow growth mode is associated with thermodynamically less stable homogeneously alloyed crystals generating less latent heat, but stable growth fronts.

3.1 Introduction

Crystallization associated with solidification or from supersaturated solutions is omnipresent, playing a central role in materials production (particularly of metals and polymers), but also in geological processes (e.g. solidification of lava), [1] ice formation, [2, 3] biomineralization, [4] etc. Within living systems, under special conditions, crystals with, for instance, magnetic functionality are formed. [5] Crystallization of amorphous films or marks is important for various

Based on *Competing Crystal Growth in Ge-Sb Phase-Change Films*,
G. Eising, B. Niebuur, A Pauza and B. J. Kooi, *Advanced Functional Materials* **volnr**, page (2013)

applications such as thin film solar cells [6] and rewritable optical disks. [7] Due to the importance of crystallization, the kinetics and morphology of crystal growth have been studied for a long time. Most emphasis has been on crystal growth from the melt or from solutions, where undercooling or supersaturation is the important driver of crystal growth. Crystallization in solid amorphous materials generally requires heating to temperatures above the glass transition temperature and below the melting temperature. Depending on, for example, the sample composition, temperature, contaminations and heating or cooling rates, many crystallization mechanisms leading to various growth rates and morphologies have been observed, for instance planar-front or faceted growth, dendritic growth, spherulitic growth, seaweed growth or growth with dense branching morphology and fractal growth. [8–12] These morphologies largely influence the properties of crystalline materials, for instance metals and polymers. The present work focuses on phase-change materials which are of importance for data storage applications where their working principle is based on the reversible fast switching of small volumes between amorphous and crystalline phases which show distinct differences in optical and electrical properties.

The pronounced temperature dependence of crystal-growth speed recently found in phase-change materials not only rationalizes their favorable characteristics for non-volatile memory applications, but also suggested new insight into their fundamental properties. [13, 14] The kinetic coefficient for crystal growth (which is the limiting growth velocity when the thermodynamic factor is one) was shown to have a non-Arrhenius temperature dependence for the important phase-change material $Ge_2Sb_2Te_5$, indicating a high kinetic fragility of the liquid ($m \approx 90$). Furthermore, there was evidence for substantial decoupling of crystal growth from viscous flow on cooling towards the glass transition temperature T_g: the growth rate extrapolated to $T_g$was found to be 10^5 times faster than would be calculated from the viscosity of 10^{12} Pa s at the glass transition. [14] Still, this work and other recent work [15] suggest that the growth rate in-between the glass transition temperature and the melting temperature is a continuous function of temperature. Here, we show that this physical picture is in general too simplified. We demonstrate that crystallization in phase-change materials can proceed in different temperature regimes via different growth modes with different temperature dependences of the growth rate. Moreover, in this study we present evidence of crystal growth in amorphous Ge_xSb_{100-x} thin films with $x = 6$, 7, 8, 9 and 10 showing both plane-front growth and dendritic-like growth at a single external temperature within one sample. Clear evolutions of these competing crystal growth modes are observed as a function of temperature for a certain composition and also as a function of composition x. Transition regimes in composition and temperature are found where both crystallization modes proceed at the same time (i.e. for the same composition and temperature). These different modes show different growth

rates and morphologies and correspond to different optical contrasts due to the difference in microstructure. The fast growth mode shows a growth mechanism that favorable couples to a crystallization mechanism recently found by molecular dynamics simulations in the phase-change material AgInSbTe. [2]

Crystallization processes, i.e. transformations from amorphous to crystalline phases, are intrinsically exothermic in nature. Inherent to the decrease in entropy upon crystallization and the high crystal growth rates observed for phase-change materials is the probability that explosive crystallization (EC) occurs, implying that the latent heat, released during the initial crystallization induced locally, is used for a self-sustained propagation of the crystallization front. Indeed, EC has been observed in Si, Ge, pure Sb and Sb-alloy films (the latter being of direct importance for PC applications). [16–18] In the alloys from Ge_6Sb_{94} to $Ge_{10}Sb_{90}$ investigated in this chapter we did not observe EC for layer thicknesses up to 400 nm. However, this does not mean that latent heat is not produced. Still, latent heat raises the local crystal growth front temperature during crystallization, accelerates crystal growth and contributes to interesting novel crystal growth phenomena presented here.

3.2 Experimental

3.2.1 Samples

Samples investigated consist of 50, 200 or 400 nm thin films with a Ge_xSb_{100-x} composition (with $x = 6$, 7, 8, 9 and 10) on a 1.3 mm thick glass substrate. The films were deposited and further processed as described in section 2.1.

3.2.2 Film characterization

The topography was measured using a Veeco PicoForce Multimode atomic force microscope (AFM) with Nanoscope V controller. The samples were grounded using silver paste to limit the effect of surface charging on the AFM image. The film composition was confirmed using energy-dispersive X-ray spectroscopy (EDAX) connected to a scanning electron microscope (SEM) (Philips XL30 FEG-ESEM). Transmission electron microscopy (TEM) was performed using a JEOL2010F operating at 200 kV.

3.2.3 Crystal growth characterization

Isothermal measurements were performed on the samples between $T = 80\,°C$ and $T = 210\,°C$. These temperatures were chosen for each composition such that the resulting growth rates could

be properly recorded in limited time by the optical technique outlined below and in section 2.3. The samples were heated to the desired temperature at a rate of 20 °C min^{-1}. The temperatures were stable within 0.2 °C during the isothermal measurements. The duration of the isothermal experiments ranged from several minutes to hours. Snapshots were taken at regular intervals for analysis. With typically 100 to 300 of these snapshots the image analysis described in section 2.3 was performed.

3.3 Results

Samples with 200 nm thick phase-change films deposited on glass substrates were placed on a hot plate for isothermal measurements. Figs 3.1a and 3.1b show optical recordings taken during isothermal heating at 185 °C of an amorphous Ge_9Sb_{91} film. The crystal nucleation starts after an incubation time of 270 ± 30 s, after which the nucleated crystals grow in a more or less isotropic manner and form crystals with circular shapes, see the inset in Fig. 3.1a. The nucleation rate in these materials is low and only a few additional nuclei are formed during the measurement after the initial nucleation has started. 600 ± 50 s after the annealing temperature has been reached triangular shaped crystals nucleate and start to grow as seen in Fig. 3.1. Most of these crystals grow at the edge of the already formed round crystals, that is, the already present crystals act as a nucleation sites, but nucleation is also found at new sites in the amorphous film. The triangular shaped crystals have a rougher crystal growth front and show faster crystal growth than the circular crystals. Due to the faster growth of the triangular shaped crystals they grow around the slower circular isotropic growing crystals, see Fig. 3.1b. In time additional fast growth crystals nucleate until the sample is fully crystallized.

Time and growth rate mappings, displaying the crystalline-amorphous interface as function of time and the crystal growth rate as function of position, are obtained from the raw images using the method described in section 2.3, and are shown in Figs 3.2a and b. From the time mapping (Fig. 3.2a) it can be clearly seen that if the crystalline boundary of the fast growth crosses slow growth, the latter will be embedded in the fast growth crystal with little disturbance in the fast growth crystal boundary once the growth front has passed the slowly growing crystal. In Fig. 3.2b the difference in growth rate between the two crystal growth modes is clearly visible. For example, for $T = 185$ °C, the slow growth mode crystals grow at a rate of $\sim$0.06 μm s^{-1} while the fast growth shows a growth rate of $\sim$1.1 μm s^{-1}, i.e. almost twenty times faster.

This analysis has been repeated for different temperatures in the range of 180 °C to 188 °C. For each temperature the two most occurring speeds in the histogram of the growth rate mapping have been taken and plotted in an Arrhenius plot, see Fig. 3.3a. Clearly two regimes of growth can be identified, and when fitted using an Arrhenius dependence we obtain two acti-

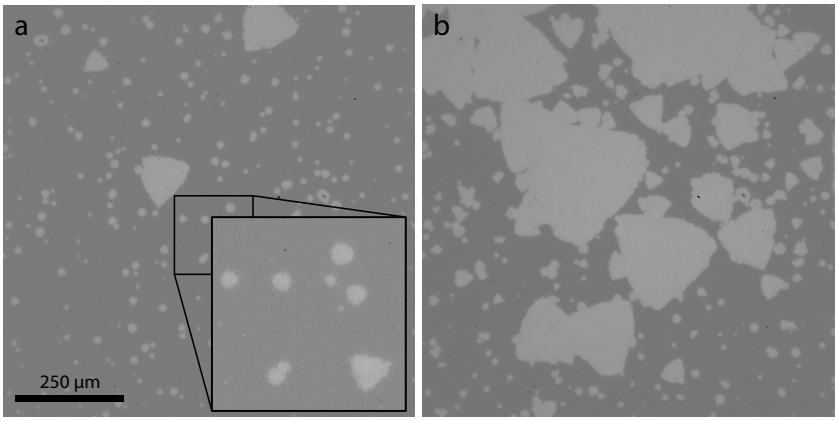

Figure 3.1 | **a** and **b** Crystal growth as observed in-situ using optical microscopy in a 200 nm thick Ge_9Sb_{91} film at 185 °C. **a** 570 s and **b** 650 s after reaching the isothermal annealing temperature indicating an initial slow growth mode followed by a later fast growth mode.

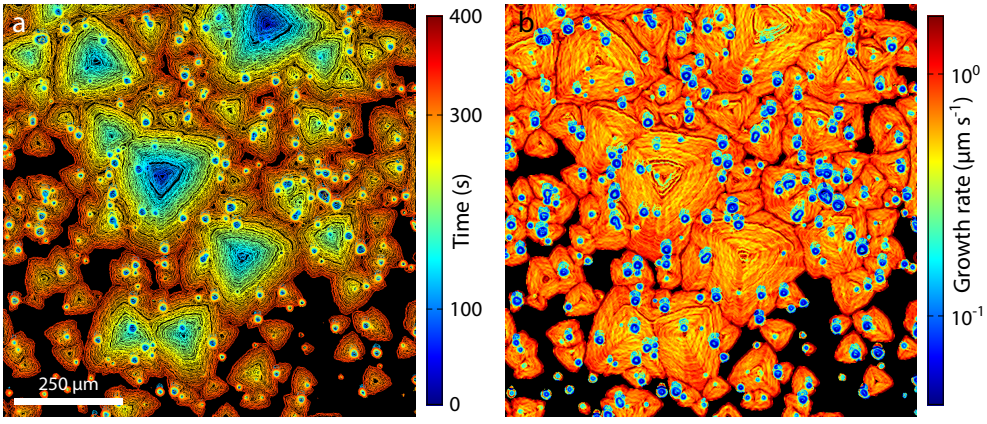

Figure 3.2 | **a** Time mapping of an isothermal experiment at 185 °C for a 200 nm thick Ge_9Sb_{91} film showing the crystalline-amorphous interface as function of time. **b** Crystal growth rate image obtained from the time mapping showing the growth front velocity at each position.

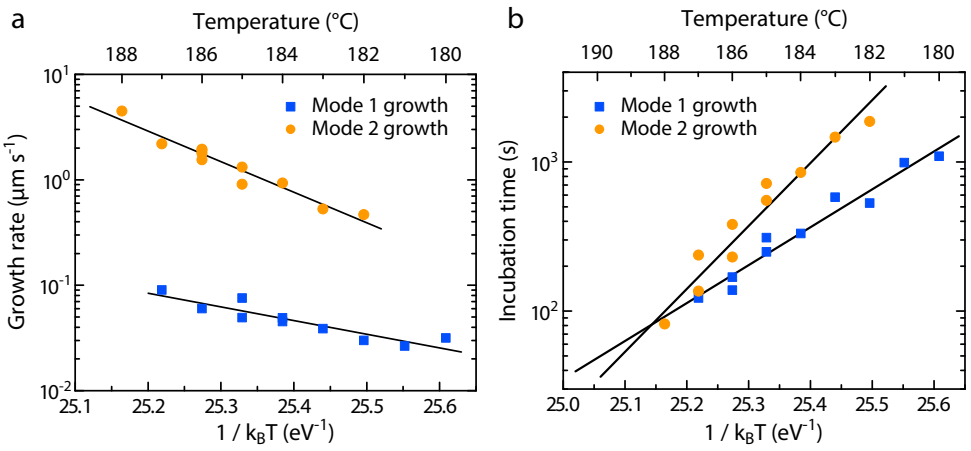

Figure 3.3 | a Growth rate versus and **b** incubation time for crystallization versus reciprocal temperature for the slow (blue squares) and fast (orange circles) crystal growth modes.

vation energies for growth: 3.0 ± 0.1 eV for the slow growth mode and 6.6 ± 0.2 eV for the fast growth mode. Interesting to note that these crystallization temperatures are very close to the estimated glass transition temperature for Ge_9Sb_{91} of ~181 °C based on calculations by Raoux et al. [19]

The incubation times for both crystal morphologies found in Ge_9Sb_{91} as function of temperature are shown in Fig. 3.3b. For the highest annealing temperature used (188 °C) it was found that only fast growth crystals are visible, as its incubation time has become shorter than or equal to the incubation time for slow growth. For annealing temperatures below 181 °C the sample is fully crystallized by isotropic slow growth within the incubation time pertaining to the fast growth mode, therefore, no fast growth is found.

A more detailed optical image of both crystal modes is shown in Fig. 3.4. From the image it can be clearly seen that the surface of the faster growing triangular shaped crystal is rougher than the isotropic growing crystals, which exhibit a smooth surface. It also shows that there is a difference in height between the crystalline and amorphous phases as expected, [20] but also a difference in height between the two crystalline phases. A dendritic/seaweed-like structure with a threefold symmetric structure can be seen in the fast growing crystals.

Additionally, the crystal morphologies grown at different temperatures were investigated. For this, the samples were first annealed at 186 °C until both crystal morphologies developed. Once both morphologies were clearly present and a growth rate could be determined for both, the sample was rapidly cooled down to 170 °C after which the temperature was again increased

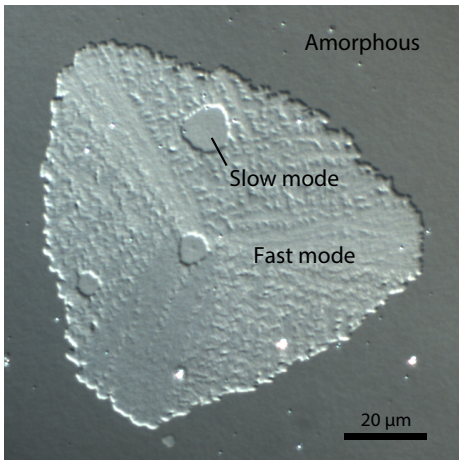

Figure 3.4 | Optical micrograph of a fast mode crystal growing around slow mode crystals in an amorphous background for a 200 nm thick Ge_9Sb_{91} film crystallized at 186 °C

to 182 °C. After a short incubation time slow growth occurred again with fast growth occurring after a longer incubation time. The resulting crystalline structure is shown in Fig. 3.5a. The applied annealing temperature does not only change the dominant growth mode, it also influences the optical reflectivity (of the slow growing crystals) and the density of the branches in the dendritic-like structure (of the fast growing crystals).

When comparing the two slow growth morphologies in Fig. 3.5a, the one grown at lower temperature is darker gray and thus less reflective. Additionally, the contrast at the interfaces between two slow growing crystals is an indication for a height difference. For the dendritic-like growth in the fast growing crystals we see a denser dendritic-like structure at 182 °C than at 186 °C. Atomic force microscopy (AFM) measurements confirm the change in density for the different temperatures, see Fig. 3.5b. A height difference of 2–3 nm is found between the amorphous phase and slow growth at 182 °C. Between the two slow growth morphologies a similar height difference is measured. The fast growth has on average the same height as slow growth at the same temperature. The average roughness of fast growth (∼0.8 nm RMS) is twice the average roughness of the slow growth morphologies (∼0.4 nm RMS).

Also SEM-EDX analyses were performed to determine the local chemical compositions of crystals formed by the slow growth mode and the fast growth mode in comparison to the initial amorphous phase. Within the limited excitation volume probed with SEM-EDX in the 200 nm films no relevant composition differences were found between all the phases or morphologies. Figs. 3.4 and 3.5 may give the impression that the slow and fast growth modes can be associated

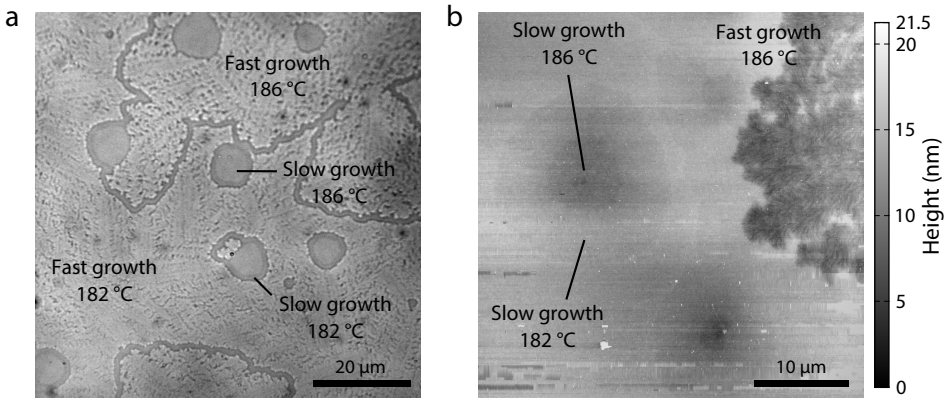

Figure 3.5 | Slow and fast crystal growth morphologies in a 200 nm thick Ge_9Sb_{91} film grown at two temperatures. **a** Optical micrograph showing both growth modes at 182 °C and 186 °C. **b** AFM image showing the height difference between the amorphous phase, the slow growth mode at 182 °C and at 186 °C and the fast growth mode at 186 °C.

with phase separation, which may be expected for Ge-Sb alloys, because according to the phase diagram Ge and Sb are hardly miscible and a eutectic occurs at a composition of $Ge_{15}Sb_{85}$. [21] However, the SEM-EDX measurements thus clearly indicate that the crystals formed by the slow growth mode or the fast growth mode have the same overall composition equal to the composition of the initial amorphous phase. Moreover, we have another proof that this has to be the case, because both the slow and fast-growth modes can be responsible for the complete crystallization of the phase-change film. The slow growth mode occurs at lower temperatures ($\leq$ 181 °C) and the fast-growth mode at higher temperatures ($\geq$ 188 °C) and only at the intermediate temperatures both growth modes occur simultaneously and compete. This is, by itself, a proof that crystals grown by the slow mode cannot be the second phase due to the phase separation, because the second phase alone cannot be responsible for the complete crystallization of the whole film.

Experiments, described in detail above for Ge_9Sb_{91} films, were repeated for compositions in the range from Ge_6Sb_{94} to $Ge_{10}Sb_{90}$; see Fig. 3.6 for an overview of all results. Directly evident from Fig. 3.6 is that the crystallization temperature strongly increases with increasing Ge concentration. Actually this implies that the same crystal growth rate is found for strongly increasing temperatures when the Ge concentration increases, i.e. from about 80 °C for Ge_6Sb_{94} to about 200 °C for $Ge_{10}Sb_{90}$. Moreover, the activation energy for crystal growth is also significantly increasing, i.e. from 1.7 eV for Ge_6Sb_{94} to 5.5 eV for $Ge_{10}Sb_{90}$. For Ge_6Sb_{94} and Ge_7Sb_{93} only a single growth mode is observed. For Ge_8Sb_{92} and $Ge_{10}Sb_{90}$ the same two types

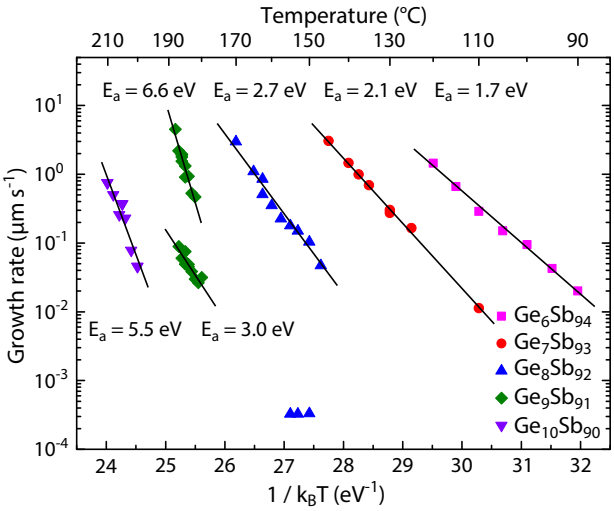

Figure 3.6 | Crystal growth rate as function of reciprocal temperature for compositions ranging from Ge_6Sb_{94} to $Ge_{10}Sb_{90}$. The black lines are Arrhenius fits to the data points and their slopes provide the indicated values for the activation energies for growth.

of growth modes occur as observed for Ge_9Sb_{91}. However, there is a significant development from Ge_8Sb_{92} to $Ge_{10}Sb_{90}$ as can be seen in Fig. 3.6 and is explained in detail below.

For Ge_8Sb_{92} under usual isothermal growth conditions only the fast growth mode is readily observed. In order to detect the slow growth mode first crystals were grown for some limited time with the fast growth mode at 160 °C. Then the temperature was abruptly decreased to about 140 °C after which the sample is heated to temperatures in the range 150–156 °C. At these lower temperatures still for a relatively long time the slow growth mode occurs after which a natural (i.e. non-induced) transition to the fast growth mode occurs. An explicit example is shown in Fig. 3.7. Upon heating to 160 °C the fast growth mode occurs after an incubation time of ∼2 min with a growth rate of 0.4 µm s^{-1}. After cooling to 150 °C the growth mode becomes slow and its growth rate becomes 0.3 nm s^{-1}. Note the more than three orders of magnitude reduction in growth rate when we only cool from 160 °C to 150 °C! After a subsequent incubation time of about 3 h at 150 °C, during which the slow growth mode occurred, the transition to the fast growth mode occurs leading to a growth rate of 0.1 µm s^{-1}, i.e. again 300 times faster than the rate of the slow growth mode at the same temperature! This procedure resulted in a slow growth mode that does not seem to be thermally activated. It is likely that the procedure to first heat to higher temperatures and then to observe slow growth at lower temperatures primes the amorphous film in such a (relaxed) state that the growth rate of the slow growth mode loses

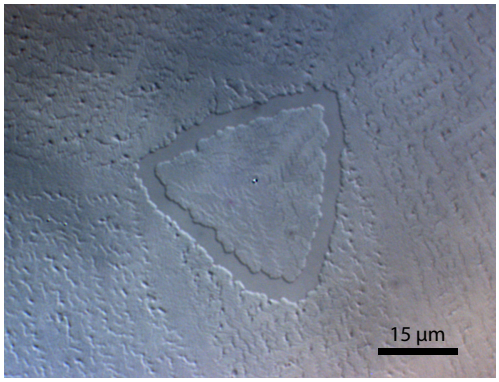

Figure 3.7 | Optical micrograph of the slow and fast crystal growth modes in a 200 nm Ge_8Sb_{92} film. The inner fast growth occurred at 160 °C, the slow growth and outer fast growth at 150 °C.

its temperature dependence in this small temperature range.

For $Ge_{10}Sb_{90}$ under usual isothermal growth conditions only the slow growth mode is readily observed. The fast growth mode can be detected, but only after most of the thin film has been crystallized. The remaining amorphous area then has become that small that it prevents a reasonably accurate determination of the growth rate of the fast growth mode. Still it is clear, similar as for Ge_8Sb_{92} and Ge_9Sb_{91}, that the fast growth mode becomes more dominant at relatively higher temperatures and the slow growth mode at relatively lower temperatures. The single growth mode observed for Ge_6Sb_{94} and Ge_7Sb_{93} actually corresponds to the fast growth mode as can be readily deduced from (i) the overall triangular crystal shape, (ii) the dendrite-like structure directly associated with the surface topography and (iii) the observed trends in growth rates when increasing the Ge concentration.

Using transmission electron microscopy (TEM) the crystal structure of the fast growth mode was studied in more detail for 50 nm thick Ge_7Sb_{93} films. The obtained diffraction patterns, with a few examples shown in Fig. 3.8, hold for the $R\bar{3}m$ crystal structure that can be described with a hexagonal lattice with a and c lattice parameters of 4.30 ± 0.06 Å and 11.0 ± 0.3 Å, respectively. Diffraction patterns taken at several locations along the growth path, from the center of the crystal (where it actually nucleated) towards the crystal tips at the growth front show a rotation of the crystal structure. In the center, point **a** in Fig. 3.8, the [0001] axis of the crystal is parallel to the film normal, i.e. crystals tend to nucleate with the (0001) plane parallel to the surface to minimize surface energy. [22, 23] However, during subsequent lateral growth of the crystals the crystal orientation at the three tips of the triangular shaped crystals gradually becomes tilted. At a distance of about 7 µm from the center of the crystal the [0001] axis is tilted in the direction of growth with an angle of about 53°, such that the $[20\bar{2}1]$ becomes

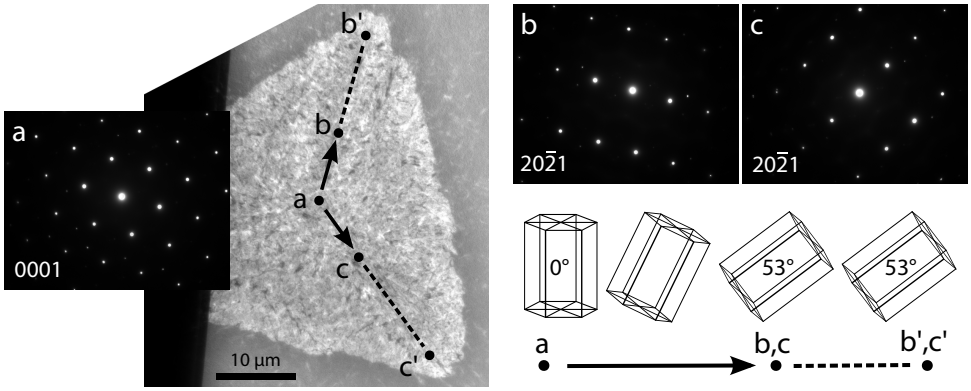

Figure 3.8 | Overview TEM image of a representative crystal with the common triangular shape in a 50 nm thick Ge_7Sb_{93} film where the diffraction patterns are shown for a few decisive locations, i.e. at the center (point **a**) and along two of the principal growth axes (points **b** and **c**). In the center (**a**) were nucleation occurred the crystal is oriented with the [0001] perpendicular to the surface. Along each growth axis the structure rotates continuously around an axis perpendicular to the growth direction such that the [20$\bar{2}$1] becomes perpendicular to the surface in **b** or **c** and this orientation is maintained during growth to **b'** or **c'** as schematically illustrated in the lower right panel.

oriented normal to the film; see point **b** and **c** in Fig. 3.8. This tilted orientation appears then to be stable during further lateral growth and the same tilted orientations are found for the points **b'** and **c'** . The same result with tilting from the [0001] axis normal to the film in the center of the crystals to the [20$\bar{2}$1] axis normal to the film at the crystal tips was observed for several crystals analyzed with TEM and seems to hold in general for all crystals (with triangular shape) in Ge_7Sb_{93}. Apart from selected area electron diffraction patterns, we also performed TEM-EDX analyses using a probe with a diameter of ∼5 nm to locally measure compositions in the crystals (with triangular shape) in Ge_7Sb_{93}. Clear indications of decomposition could not be found, although this cannot be ruled out, because its detection is strongly hampered by the complex (transrotational) structure of the crystals and by the projective nature of the TEM analysis which cannot observe decomposition in the projection direction. Moreover, the type of morphology of these crystals strongly suggests that decomposition on a nanoscale is expected to play a role in contrast to the slow growth mode where crystals are completely homogeneous.

In Fig. 3.9 the results of XRD measurements (in Bragg-Brentano geometry) are shown for 400 nm thick Ge9Sb91 films, where one film was completely crystallized (at 180 °C) by the slow growth mode (red marks and line) and another film was completely crystallized (at 190 °C) by the fast growth mode (blue marks and line). The slow growth mode can be associated with a strong texture with the [0001] axis perpendicular to the surface and the fast growth

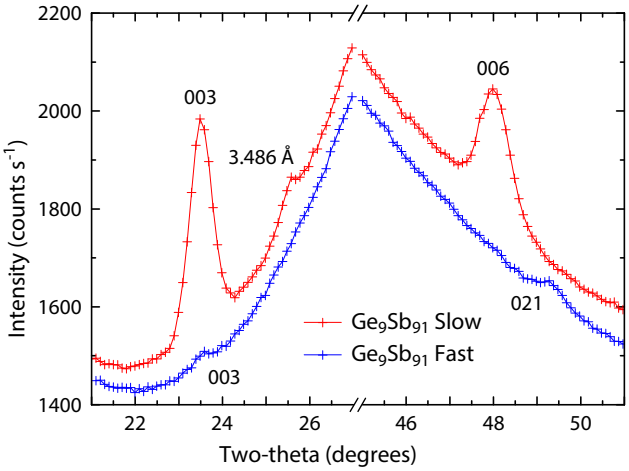

Figure 3.9 | XRD measurements (Bragg-Brentano geometry) for 400 nm thick Ge_9Sb_{91} films, where one film was completely crystallized (at 180 °C) by the slow growth mode (red marks and line) and another film was completely crystallized (at 190 °C) by the fast growth mode (blue marks and line).

mode results in hardly measurable diffraction peaks, where the (0003) and the $(20\bar{2}1)$ peaks are just discernible. The relatively steep backgrounds originate from the amorphous glass substrate. The strong difference in diffracted intensity in the (*hkl*) peaks between the slow and fast growth modes can be attributed to the transrotational crystals being present in the fast growth mode (see also TEM results of main article) and absence of transrotational effects in the slow growth mode. In crystals showing severe transrotational effects the effective sizes of crystals only showing translational symmetry (without severe bending of crystal planes) becomes very small and explains the dramatic decrease in the diffracted intensity in the (*hkl*) peaks for the fast growth mode. Still, the weak presence of the (0003) and the $(20\bar{2}1)$ peaks indicate the rotation from [0001] to $[20\bar{2}1]$ perpendicular to the surface as was also observed by TEM for crystals grown by the fast mode in 50 nm thick Ge_7Sb_{93} films. The XRD date pertaining to the slow growth mode indicates a *c* lattice parameter (of the $R\bar{3}m$ structure that can be described with hexagonal lattice parameters) of 11.355 Å (based on three peaks). The XRD date pertaining to the fast growth mode indicates a *c* lattice parameter of 11.340 Å based on the (0003) peak and then the $(20\bar{2})$ peak indicates an a lattice parameter of 4.318 Å. These results compare well with the $R\bar{3}m$ lattice parameters of pure Sb, which are $a = 4.3084$ Å. and $c = 11.274$ Å.

Since Ge-Sb alloys have a strong tendency to phase seperate into (nearly) pure Sb and Ge, additional peaks due to decomposed Ge can be present. However, the XRD results do not show any discernible peak that can be ascribed to Ge. This not necessarily means that decomposed

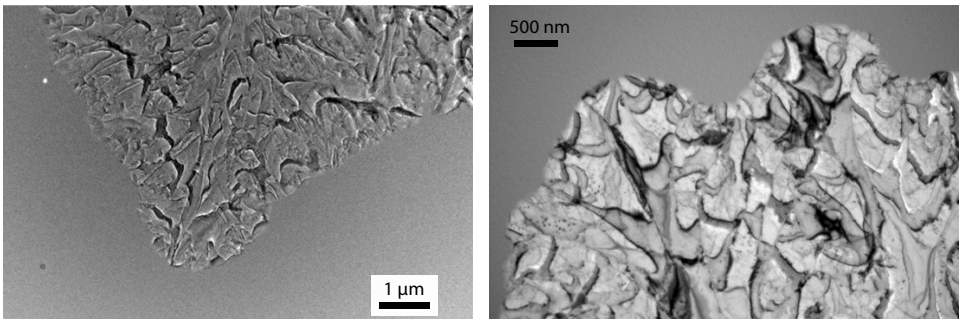

Figure 3.10 | Bright-field TEM images for a 50 nm thick Ge_7Sb_{93} film on a (20 nm thick) silicon nitride membrane partially crystallized at 130 °C, showing the crystal growth fronts at the corners of the crystals with a triangular shape as produced by the fast growth mode. Note the severe bending contour contrast within the crystals that is connected to the transrotational structure of the crystals grown by the fast growth mode.

Ge is absent, because at these low temperatures used for crystallization it is likely, that when Ge phase separates into sufficient large volumes it still remains an amorphous phase that cannot be detected by XRD. However, based on all results we obtained we expect that Ge phase separates only within the fast growth mode as extremely thin (nearly atomic thick) platelets on the (001) planes of the $R\bar{3}m$ structure. Such platelets might be observable by HRTEM, but the strong transrotational effects in the crystals formed by the fast growth mode makes such observations hardly possible (see also TEM images in Fig. 3.10).

3.4 Discussion

All the above results can be casted in a kind of unifying physical picture. We start with the fact that, in the solid state, GeSb alloys are (thermodynamically) not stable in a homogeneous state, because they want to decompose in almost pure Ge and Sb with a eutectic at a composition of $Ge_{15}Sb_{85}$. Direct crystallization in such a decomposed (eutectic) state generates most enthalpy. However, at low temperatures, near the crystallization temperature, which is also very close to the glass transition temperature (as explained in the previous section), the driving force for crystallization is high, but the atomic mobility very low (viscosity high). Therefore, such decomposition is often suppressed. For pure Sb this does not hold and amorphous Sb already (after some incubation time) crystallizes at room temperature, where also explosive crystallization (EC) can be ignited, indicating the importance of enthalpy release on crystal growth. With increasing Ge concentration, amorphous GeSb becomes stable at room temperature and shows strongly increasing crystallization temperatures as our current work shows when the

Ge concentration increases from 6 to 10 at.%. This can be expected, because the more Ge is added to Sb the more crystallization is frustrated. [22,24,25] Also the potential decomposition of the alloy into the pure phases is increasingly frustrated at low temperatures. Therefore, it can be anticipated that below a certain Ge concentration at relatively low temperatures decomposition is still possible and beyond this concentration decomposition is suppressed (but of course decomposition at higher temperatures is still possible in agreement with observations for temperatures beyond 300 °C). [25–27]

Our results show that this transition in growth mode is not sharp, but that two coexisting growth modes are observed for Ge_8Sb_{92}, Ge_9Sb_{91} and $Ge_{10}Sb_{90}$. The lower temperature branch (slow growth) corresponds to circular crystals with very smooth surfaces and the higher temperature branch (fast growth) to crystals with overall triangular shape and rough surfaces and crystal-growth fronts indicating dendritic-like growth. The explanation we propose here for these two growth modes is that the dendritic-like mode corresponds to (partial) phase separation such that most latent heat is released during crystallization. In the slow growth mode crystals are formed in which Ge and Sb are still homogeneously alloyed. Because these alloyed crystals exhibit a considerable amount of configurational entropy ($x \ln x + (1 - x) \ln(1 - x)$ in a regular solution model, with x the Ge-concentration), less latent heat is released. In the dendritic-like case the latent heat increases the crystal growth front temperature and provides temperature gradients across the growth-front stimulating this dendritic-like growth. Moreover, impurities are generated which are also considered an important cause for crystal growth front instability. [8,10] In the slow growth mode the lower amount of latent heat released leads to lower growth rates and the absence of decomposition and impurities in combination with the lower growth rate leads to a stable growth front.

The above explanation is consistent with the experimental observations:
(1) It explains that with increasing Ge concentration, which increasingly leads to frustration of crystallization and to higher crystallization temperatures, at relatively low temperatures the slow growth mode is introduced and becomes increasingly dominant, because the configurational entropy of the homogeneously alloyed crystal becomes larger, allowing the opening of this new crystal growth branch. The relative increase in configurational entropy for alloyed crystals with increasing Ge concentration is obvious when considering the $x \ln x + (1-x) \ln(1-x)$ term of a regular solution model (with x the Ge-concentration). It explains why for Ge_8Sb_{92} the fast growth mode is still dominant; that for Ge_9Sb_{91} both growth branches are naturally coexisting and that for $Ge_{10}Sb_{90}$ the slow growth mode becomes dominant (when with normal heating rates isothermal crystallization temperatures are approached showing crystallization after incubation times of typically less than tens of minutes).
(2) This explanation is also consistent with the observation that for a certain Ge concentration

the fast growth mode is becoming increasingly dominant at higher temperatures and the slow growth mode at lower temperatures, because decomposition is suppressed at the lower temperatures. Moreover, it also explains that a natural transition from the slow to fast growth mode is possible, when still after sufficient time the slow mode is able to produce sufficient latent heat to generate (i) a higher growth front temperature allowing more atomic mobility required for decomposition and (ii) a temperature gradient across the growth-front (with higher temperature ahead of the front in the amorphous phase) such that the growth front loses it stability against perturbations. Then, the transition to the dendritic-like growth mode occurs. On the other hand, a transition from the fast growth mode to the slow growth mode is not directly possible. Only by a decrease in external temperature the fast growth mode can be halted and turned into the slow growth mode, which after a certain incubation time then still at these lower temperatures can switch to the faster growth mode.

(3) Obviously, it explains why the faster growth mode is actually faster, but it also partly explains the exceptionally high activation energies for growth found and why this is higher for the fast growth mode. The role played by latent heat is crucial. At higher temperatures with higher growth rates more latent heat per unit of time is produced leading to increasing discrepancies between the actual growth front temperature and the externally applied temperature, where the latter is used for the Arrhenius plots to determine the activation energy for growth. This results in an apparent larger slope (and thus activation energy for growth) in the Arrhenius plots than when the actual growth front temperatures would be used. Note for instance that the temperature interval in Fig. 3.3a used to determine the activation energy for growth for both modes is only 5 K. If the actual temperature interval is 10 K the activation energies for growth would be a factor two lower. Such a relatively subtle additional increase of 5 K for the temperature difference between the lowest and fastest growth rate measured per growth mode can be readily introduced, because the growth rates differ at least a factor three. Note that explosive crystallization can lead to an increase in growth-front temperature, such that a liquid layer is formed at the growth front. This is for instance possible for amorphous Si and Ge films. [28,29] Therefore the temperature increases at the growth front proposed in this chapter can be considered very modest and highly likely. Moreover, this explanation directly indicates that the activation energies for growth and for overall crystallization determined experimentally have to be considered with care.

(4) It explains the difference in growth morphologies observed. The dendrite-like structure can actually be typified as a mixture of a dendrite, seaweed and transrotational crystal structure. Gránásy et al. elegantly showed transitions from single crystal dendritic to polycrystalline seaweed structures. [10] In our case the structure is not single crystalline in the sense of only a translational repeating units in the structure, but it is also not polycrystalline with decou-

pled orientations of neighboring grains. Actually, during lateral crystal growth also a certain amount of rotation (generally around an in-plane rotation axis tangential to the growth front) couples the newly formed crystal region to the crystal region that was just before at the growth front. [22, 30] However, the present transrotational crystals also show important differences with the transrotational crystals found earlier. [22] The earlier ones still showed smooth (apart from the curvature due to the overall shape) planar growth fronts, whereas in the present case the growth fronts are more rough with single or double parabolic tips, see Fig. 3.10, which are typical for dendritic or doublonic growth. [9, 11] The transition from dendritic to seaweed growth can have a few origins, such as impurities and reducing the orientational-translational mobility ratio, like nicely demonstrated by the work of Gránásy et al. [10] where the role played by impurities was earlier put forward in Ref. [8]. Also in the fast growing crystals impurities, like introduced intrinsically by the strong driving force for decomposition of the Ge-Sb phase, will contribute to development of the observed mixture of dendritic, seaweed and transrotational crystals. Although there is some disorder in tip splitting and side branching, which is the basis for the seaweed morphology, still, images, like shown in Figs 3.4, 3.5a and 3.7, clearly indicate that the various branches have preferential mutual orientations (angles) indicative of dendritic growth.

Based on Molecular Dynamics simulations of the phase-change material AgInSbTe (AIST) a proposal for an avalanche-type crystal growth mode was recently put forward. [2] Interestingly, this proposed growth mode appears to couple favorably to the fast growth mode that is observed in the present work. In Ref. [2] a bond-interchange model has been proposed, where crystallization of amorphous AIST can be viewed as a rapid succession of diffusionless events in such a way that the 3+3 octahedra (i.e. with 3 shorter strong bonds and 3 longer weaker bonds also typical for pure Sb) are aligned along the crystalline *c* axis imposed by the surrounding crystal. Based on reduction of surface (interfacial) energy the crystal nucleus develops with the *c* axis perpendicular to the surface. Since AIST and the present Ge-Sb alloys are so-called fast-growth type materials having difficulty to nucleate, this favorable orientation is crucial for enabling nucleation. However, this is apparently an unfavorable orientation for growth. Based on the initial symmetry therefore the 3+3 octahedra tend to rotate the *c* axis in such a way that three main branches develop out of the nucleus with an in-plane mutual angle of 120°. Our work shows that a favorable growth orientation is with the *c* axis inclined 53° towards the growth direction of each of the three main branches, i.e. the $[20\bar{2}1]$ becomes oriented normal to the film surface. This latter result can of course not be predicted from the bond-interchange model proposed in Ref. [2], but the three-fold growth symmetry (cf. Figs. 3 and 6) can be understood well on the basis of this model. The favorable comparison thus holds for the crystallography and the avalanche type crystal growth mode, but a difference is that

we expect some nanoscale phase separation between Ge and Sb during the fast growth mode, whereas the bond-interchange model is basically a diffusionless model.

The present explanation thus holds for phase-change materials typified as fast-growth materials (FGM) and in principle only for systems where one or more solutes (like Ge) are added to a solvent (like Sb). However, there is nice analogy with so-called nucleation dominant materials (NDM), typically on or near the GeTe–Sb_2Te_3 tie line. These materials, when crystallized, first form at lower temperatures a meta-stable NaCl-type structure and at higher temperatures a stable trigonal-type crystal structure closely resembling the $R\bar{3}m$ structure of Sb. Although these two crystal growth modes in NDM do not coexist, they correspond to the same solution as found here for FGM, i.e. with two growth modes, where one is forming a more random (higher configurational entropic) system at lower temperatures and the other a more ordered system at higher temperatures. In the meta-stable NaCl type structure, Te atoms are on the Cl-sublattice sites and Ge and Sb are (together with structural vacancies) more or less randomly distributed over the Na-sublattice sites. [31] In the stable rhombohedral crystal structure all the atoms keep their (distorted) octahedrally coordinated position, but Ge and Sb now take an ordered position such that an ordered layered structure is developed. For instance the stable structure of $Ge_2Sb_2Te_5$ can be described by a hexagonal lattice, where the a–b–c stacking of the basal planes in this lattice corresponds to Te–Ge–Te–Sb–Te–Te–Sb–Te–Ge and then repetition of this nine layer basic building block. [32] This clearly demonstrates the more ordered structure at higher temperatures and a more random meta-stable crystal structure at intermediate temperatures. A very similar solution as found here.

The present physical picture can potentially also be related to the observation that the growth rate extrapolated to T_g was found to be 10^5 times faster than would be calculated from the viscosity of 10^{12} Pa s at the glass transition. [14] The reason is that the viscosity is correlated with the actual glass transition temperature, but that the growth rate due to the release of latent heat corresponds to an actually higher temperature at the crystal growth front.

3.5 Conclusions

Crystal growth has been studied in detail for Ge_xSb_{100-x} thin films with $x = 6$, 7, 8, 9 and 10 for film thicknesses ranging from 50 to 400 nm. The crystallization temperature increases from about 80 °C for Ge_6Sb_{94} to about 200 °C for $Ge_{10}Sb_{90}$ and simultaneously the activation energy for crystal growth also largely increases from 1.7 eV to 5.5 eV. For Ge_6Sb_{94} and Ge_7Sb_{93} a single growth mode was observed, but in the three alloys with higher Ge concentration two competing growth modes were observed. A slow growth mode produces circular crystals, having smooth crystal growth fronts and surfaces and a fast growth mode produces crystals with a

triangular shape, having clearly rougher growth fronts and surfaces corresponding to a growth morphology which is a mixture of dendritic/seaweed/transrotational growth. Crystals formed by both growth modes have the same overall composition, remaining equal to the initial composition of the amorphous phase. The slow growth mode can only be invoked with difficulty in Ge_8Sb_{92} (and is absent in Ge_6Sb_{94} and Ge_7Sb_{93}), is generally only initially dominant in Ge_9Sb_{91} after which it is overrun by the fast growth mode, but becomes dominant in $Ge_{10}Sb_{90}$, where only in the latest stages of crystallization the fast mode appears. For a certain Ge concentration the slow growth mode is dominant at the lower temperatures and the fast growth mode at higher temperatures, but there is an overlapping temperature interval where the initial slow growth mode is naturally overtaken by the fast growth mode. These observations demonstrate that the common view that the growth rate in-between the glass transition temperature and the melting temperature is a continuous function of temperature is not correct, because there can be orders of magnitude differences in growth rate at a single temperature for the different growth modes. For instance, data retention of phase-change memory is predicted erroneously when measurement data is extrapolated to lower temperatures, but where the growth mode also changes when going to lower temperatures.

Latent heat released upon crystallization is considered a crucial element explaining the above results. In the fast growth mode more latent heat is generated than in the slow growth mode and we attribute this to (partial) decomposition of the GeSb phase in case of fast growth and absence of decomposition in case of slow growth. In this way the growth velocity can be much faster than would be calculated from the viscosity at the external temperature, because latent heat raises the crystal growth front temperature. For Ge_8Sb_{92} orders of magnitude differences in growth rate between the slow and fast growth mode are observed at the same external temperature, which are attributed to differences in enthalpy release and to differences in growth front temperature.

The fast-growth mode observed in this chapter shows interesting correspondence with a recently proposed bond-interchange model predicting an avalanche-type crystal growth mode in AgInSbTe phase-change alloys.

References

[1] a) S. Labrosse, J. W. Hernlund, N. Coltice, *Nature* **450**, 866 (2007); b) H. B. Mattsson, L. Caricchi, B. S. G. Almqvist, M. J. Caddick, S. A. Bosshard, G. Hetényi, A. M. Hirt, *Nature Communications* **2**, 299 (2011); c) H. S. C. O'Neill, F. E. Jenner, *Nature* **491**, 698 (2012); d) L. Stixrude, N. de Koker, N. Sun, M. Mookherjee, B. B. Karki, *Earth and Planetary Science Letters* **278**, 226 (2009).

[2] T. Matsunaga, J. Akola, S. Kohara, T. Honma, K. Kobayashi, E. Ikenaga, R. O. Jones, N. Yamada, M. Takata, R. Kojima, *Nature Materials* **10**, 129 (2011).

[3] A. Shibkov, Y. Golovin, M. Zheltov, A. Korolev, A. Leonov, *Physica A: Statistical Mechanics and its Applications* **319**, 65 (2003).

[4] a) W. J. E. M. Habraken, J. Tao, L. J. Brylka, H. Friedrich, L. Bertinetti, A. S. Schenk, A. Verch, V. Dmitrovic, P. H. H. Bomans, P. M. Frederik, J. Laven, P. van der Schoot, B. Aichmayer, G. de With, J. J. DeYoreo, N. A. J. M. Sommerdijk, *Nature Communications* **4**, 1507 (2013); b) H. Li, H. L. Xin, M. E. Kunitake, E. C. Keene, D. A. Muller, L. A. Estroff, *Advanced Functional Materials* **21**, 2028–2034 (2011).

[5] a) A. Komeili, Z. Li, D. K. Newman, G. J. Jensen, *Science* **311**, 242 (2006); b) A. Scheffel, M. Gruska, D. Faivre, A. Linaroudis, J. M. Plitzko, D. Schüler, *Nature* **440**, 110 (2006).

[6] S. Sriraman, S. Agarwal, E. S. Aydil, D. Maroudas, *Nature* **418**, 62 (2002).

[7] a) A. V. Kolobov, P. Fons, A. I. Frenkel, A. L. Ankudinov, J. Tominaga, T. Uruga, *Nature Materials* **3**, 703 (2004); b) M. Wuttig, N. Yamada, *Nature Materials* **6**, 824 (2007).

[8] a) H. D. Keith, F. J. Padden, *Journal of Applied Physics* **34**, 2409 (1963); b) N. Goldenfeld, *Journal of Crystal Growth* **84**, 601 (1987).

[9] H. M. Singer, J. H. Bilgram, *Physical Review E* **70**, 031601 (2004).

[10] L. Gránásy, T. Pusztai, T. Börzsönyi, J. A. Warren, J. F. Douglas, *Nature Materials* **3**, 645 (2004).

[11] B. Utter, E. Bodenschatz, *Physical Review E* **72**, 011601 (2005).

[12] B. C. Okerberg, H. Marand, *Journal of Materials Science* **42**, 4521 (2007).

[13] M. Wuttig, M. Salinga, *Nature Materials* **11**, 270 (2012).

[14] J. Orava, A. L. Greer, B. Gholipour, D. W. Hewak, C. E. Smith, *Nature Materials* **11**, 279 (2012).

[15] G. W. Burr, P. Tchoulfian, T. Topuria, C. Nyffeler, K. Virwani, A. Padilla, R. M. Shelby, M. Eskandari, B. Jackson, B.-S. Lee, *Journal of Applied Physics* **111**, 104308 (2012).

[16] D. A. Kurtze, W. van Saarloos, J. D. Weeks, *Physical Review B* **30**, 1398 (1984).

[17] M. O. Thompson, G. J. Galvin, J. W. Mayer, P. S. Peercy, J. M. Poate, D. C. Jacobson, A. G. Cullis, N. G. Chew, *Physical Review Letters* **52**, 2360 (1984).

[18] C. Wickersham, G. Bajor, J. Greene, *Solid State Communications* **27**, 17 (1978).

[19] S. Raoux, M. Salinga, J. L. Jordan-Sweet, A. Kellock, *Journal of Applied Physics* **101**, 044909 (2007).

[20] W. K. Njoroge, H.-W. Woltgens, M. Wuttig, *Journal of Vacuum Science & Technology A: Vacuum, Surfaces, and Films* **20**, 230 (2002).

[21] R. W. Olesinski, G. J. Abbaschian, *Bulletin of Alloy Phase Diagrams* **7**, 219 (1986).

[22] B. J. Kooi, J. T. M. De Hosson, *Journal of Applied Physics* **95**, 4714 (2004).

[23] A. K. Petford-Long, R. C. Doole, C. N. Afonso, J. Solís, *Journal of Applied Physics* **77**, 607 (1995).

[24] M. Lankhorst, *Journal of Non-Crystalline Solids* **297**, 210 (2002).

[25] S. Raoux, C. Cabral, L. Krusin-Elbaum, J. L. Jordan-Sweet, K. Virwani, M. Hitzbleck, M. Salinga, A. Madan, T. L. Pinto, *Journal of Applied Physics* **105**, 064918 (2009).

[26] T. Okabe, S. Endo, S. Saito, *Journal of Non-Crystalline Solids* **117–118, Part 1**, 222 (1990).

[27] L. Krusin-Elbaum, D. Shakhvorostov, C. Cabral, S. Raoux, J. L. Jordan-Sweet, *Applied Physics Letters* **96**, 121906 (2010).

[28] H.-D. Geiler, E. Glaser, G. Götz, M. Wagner, *Journal of Applied Physics* **59**, 3091 (1986).

[29] a) C. Grigoropoulos, M. Rogers, S. H. Ko, A. A. Golovin, B. J. Matkowsky, *Physical Review B* **73**, 184125 (2006); b) L. Nikolova, T. LaGrange, M. J. Stern, J. M. MacLeod, B. W. Reed, H. Ibrahim, G. H. Campbell, F. Rosei, B. J. Siwick, *Physical Review B* **87**, 064105 (2013).

[30] V. Kolosov, A. Thölén, *Acta Materialia* **48**, 1829 (2000).

[31] a) T. Nonaka, G. Ohbayashi, Y. Toriumi, Y. Mori, H. Hashimoto, *Thin Solid Films* **370**, 258 (2000); b) N. Yamada, T. Matsunaga, *Journal of Applied Physics* **88**, 7020 (2000).

[32] a) B. J. Kooi, J. T. M. De Hosson, *Journal of Applied Physics* **92**, 3584 (2002); b) J. Kim, J. Kim, S.-H. Jhi, *Physical Review B* **82**, 201312 (2010).

Chapter 4

Laser accelerated crystallization

Abstract. For a proper understanding of crystallization kinetics it is preferred that isothermal studies are performed over a wide range of temperatures. However, such studies are generally confined to relatively low temperatures due to limitations in heating ramp rates, where crystallization should not start before the sample has become equilibrated at the desired isothermal temperature. For this reason the temperature range that could be studied in the previous chapter 3 was relatively small, also because of the high activation energies for growth that hold for the studied phase-change materials. In the present chapter we extend the temperature range by applying laser-pulse heating in addition to isothermal heating of the phase-change film. We are able to optically study crystal growth at elevated temperatures not reachable using standard isothermal techniques. Still, laser pulses with durations of typically one second are used and this time is much longer than the time (less than 1 ms) required by the film to equilibrate at a certain laser-induced temperature. This way the crystal growth rates of several GeSb alloys are observed in a direct manner over six orders of magnitude. We find a non-Arrhenius temperature dependence for crystal growth and show that the growth can be well described based on a viscosity model incorporating the fragility of the supercooled liquid (glass) as an important parameter.

4.1 Introduction

Crystal growth in phase-change films is a temperature activated process. Methods for studying the crystal growth properties from room temperature up to and slightly above the glass-transition temperature are well established, and can be applied by, for example, placing a phase-change film on a hot plate or in a heating holder or furnace and using optical, atomic force or electron microscopy to study the crystal growth. [1, 2] Only microscopy-based techniques are able to directly determine crystal growth rates, because many other techniques like resistance measurements, differential scanning calorimetry, X-ray diffraction, etc. can be used to monitor the overall crystallized fraction, but cannot make a distinction between nucleation and growth. These techniques are generally also combined with isochronal (for a range of heating rates)

In preparation as *Laser Accelerated Isothermal Crystal Growth in Ge-Sb Phase-Change Films*, G. Eising, T. Van Damme, A Pauza and B. J. Kooi

instead of isothermal (for a range of temperatures) measurements making the analysis of the crystallization kinetics somewhat more approximate. Still, a drawback of isothermal measurements is that they generally limit the maximum growth rate that can be accurately measured in-situ (in our case for the optical method applied in the present thesis this is $\sim$5 μm s^{-1}). The reason for this limitations is mostly imposed by the (relatively slow) heating rates used to reach the isothermal temperature in combination with the requirement that crystallization only starts when the sample has become stabilized at the isothermal temperature.

In this chapter we will make an effort to optically observe crystal growth at higher temperatures, and thus higher growth rates, by using a laser to additionally heat the film and by monitoring the growth using a high speed camera. As explained, the benefit of optical microscopy over other methods to measure crystal growth at high temperatures, [3, 4] is that we can easily distinguish between the contribution of nucleation and growth. Moreover, phase-change materials are renowned for their excellent optical contrast between the amorphous and crystalline phase as exploited in rewritable optical disks (CD, DVD), making optical studies particularly suited. The assumption of Arrhenius-type growth behavior at temperatures higher than reachable with the standard isothermal experiments, like performed in the previous chapter 3, will be tested. In order to do so, we still have to assume that we can measure isothermal crystal growth during the laser heating. This assumption holds, because (i) the duration of the laser pulse of the order of one second (where the laser reaches its set power level in $\sim$2 ns) is clearly longer than required by the sample to become equilibrated with respect to the laser heating (less than a ms) and (ii) we actually can measure (in a confined region) constant crystal growth velocities which is a clear indication of a constant temperature, because the growth rate is strongly temperature dependent.

4.2 Experimental

4.2.1 Samples

The samples used in this chapter consist of 200 nm thin films with a Ge_xSb_{100-x} composition (with $x = 6, 7, 8$ and 9) on a 1.3 mm thick glass substrate. The films were deposited and further processed as described in section 2.1.

4.2.2 Setup

Additional heating in the sample during isothermal heating was induced by focusing a 640 nm diode laser (Coherent Obis 640-100) with variable output power (40 to 110 mW) on the sample. The onset time to reach this power is less than 2 ns. The laser beam is at an incidence angle equal

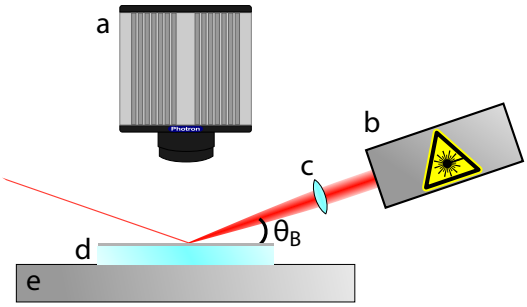

Figure 4.1 | Schematic overview of the laser setup. **a** High speed optical camera. **b** Diode laser. **c** Focusing optics. **d** Sample with a 200 nm thick GeSb film on a 1.3 mm thick glass substrate. **e** Ceramic heater. The angle between the incident laser and the sample surface should be close to the Brewster's angle, guaranteeing a maximum absorption in the film and minimum reflection.

to Brewster's angle θ_B (≈13° for the used films) [5] to minimize the reflection of the laser on the film, [6] see Fig. 4.1. Due to the angle, the circular laser beam creates a spot on the film with an elliptical shape with radii of $a \approx 250\,\mu m$ and $b \approx 110\,\mu m$ (spot size 1). By using different optics a second, larger, spot size was created with radii of $a \approx 1000\,\mu m$ and $b \approx 450\,\mu m$ (spot size 2). Optical recordings of the film were taken using a Photron 1024 PCI high speed camera, capable of recording up to 100 000 frames per second (fps). However, due to the limited resolution available at the maximum frame rate, we used recording rates of 1000 fps with a resolution of 1024×1024 pixels and 3000 fps with a resolution of 512×512 pixels. The duration of the laser pulse was 1 s to 1.4 s. This duration was long enough to obtain a constant growth rate around the center of the laser spot.

4.2.3 Image analysis

The recordings were analyzed using line profiles as outlined in section 2.3 due to the local nature of the temperature increase. Additionally, the laser spot has a Gaussian power profile and therefore the crystal growth rates were determined around the center of the laser spot parallel to the long axis of the elliptical laser spot.

4.2.4 Local temperature estimation

An important part of the performed experiment is the determination of the local temperature at the laser spot. Direct measurement of the temperature proves to be difficult and therefore, we use an estimation of the temperature. For this, we assume that the crystal growth in the Ge_6Sb_{94} films shows Arrhenius behavior and follows the fit obtained in chapter 3 also in the

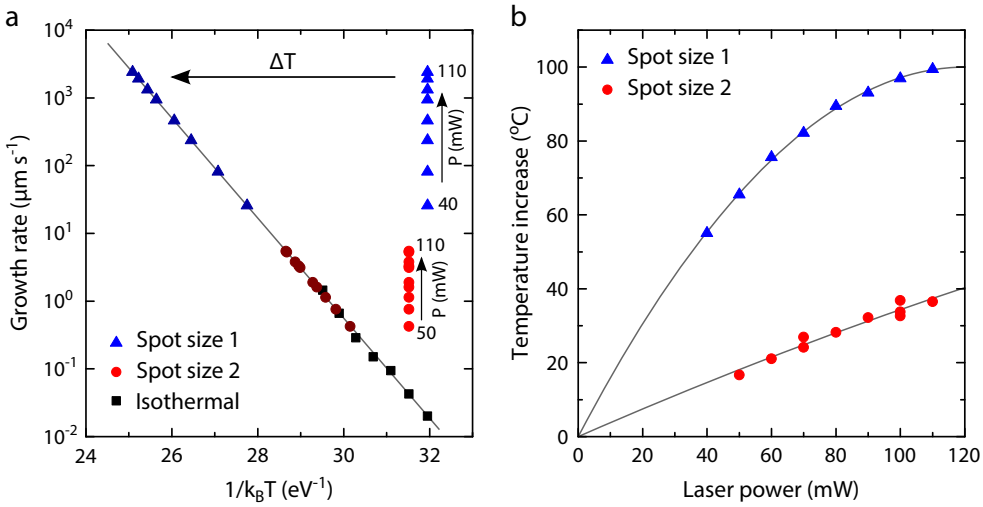

Figure 4.2 | Calibration of the temperature increase for given laser power. **a** Growth rate as function of laser power. By assuming Arrhenius-type growth behavior (gray line) for the Ge_6Sb_{94} alloy film, the temperature increase ΔT due to the laser pulse is determined. **b** Temperature differences, as determined based on the method in **a**, are plotted against laser power.

temperature range used in this chapter. As we will explain later, there is a good reason to make this assumption. In this way we can calculate the local temperature once we measure the crystal growth rate, see Fig 4.2. The growth rates are measured for different laser powers with the substrate at a fixed temperature of 90 °C (spot size 1) or 95 °C (spot size 2), see Fig. 4.2a. Using the Arrhenius fit obtained from isothermal experiments the temperature increase due to the laser pulse is determined (ΔT in Fig. 4.2a) and plotted as function of the laser power, see Fig. 4.2b. This was done for both spot sizes. For spot size 2 we find a nearly linear relation between the temperature increase and the laser power. For spot size 1 we find a decrease in the slope. This is attributed to increased heat dissipation due to an increased temperature difference with the surroundings. Second-order polynomial fits are used to interpolate the temperature increase. It is noted that, for laser-heating temperatures significantly higher than the temperature at which the calibrations were performed, the temperature increase for a given laser power is reduced (due to an increasing temperature difference with the surrounding and thus an increasing energy dissipation). The calibration thus provides an upper boundary of the temperature increase due to laser heating, whereas the extrapolation of the Arrhenius fit from the lower temperature region without laser heating (to higher temperatures) provides a lower boundary.

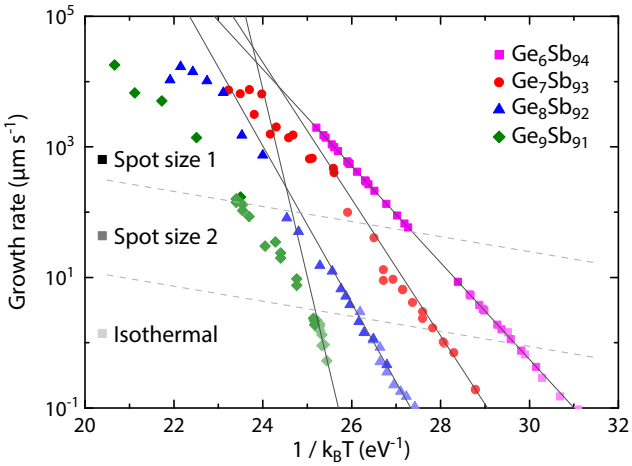

Figure 4.3 | Local crystal growth rates for standard isothermal heating with additional laser heating for compositions Ge_6Sb_{94} to Ge_9Sb_{91} versus the reciprocal temperature. Using the small spot size (spot size 1) the highest crystal growth rates are obtained. The standard isothermal results without laser heating are also included for reference, where the Arrhenius fits to these data are shown as (thin) solid black lines.

4.3 Results and discussion

The obtained crystal growth rates for the different alloys for both laser spot sizes together with the standard results from chapter 3 are shown in Fig. 4.3. With these standard isothermal experiments crystal growth rates up to $\sim 5\,\mu m\,s^{-1}$ could be obtained. Growth rates of up to $\sim 20\,mm\,s^{-1}$, i.e. 4000 times faster, are reached using the smallest laser spot size. The Ge_6Sb_{94} films show, by assumption, no deviation from the isothermal fit. For Ge_7Sb_{93} and Ge_8Sb_{92} we initially see that the data points are following the isothermal Arrhenius fit, but at higher temperatures the growth rate becomes lower than expected from extrapolating the Arrhenius fit. For Ge_9Sb_{91} this deviation is already observed at $\sim 10\,\mu m\,s^{-1}$. The change in slope of growth rate indicates a temperature dependence of the activation energy for growth.

The Arrhenius fits obtained from the crystal growth rates below $10\,\mu m\,s^{-1}$ show, when extrapolated to higher temperatures, that Ge_9Sb_{91} reaches higher crystal growth rates than Ge_6Sb_{94} (see Fig. 4.3). This is unexpected behavior, because it is well-established that GeSb alloys with a higher antimony concentration show higher maximum crystallization speeds. [7] This indicates that the slope of the measured growth rates of Ge_9Sb_{91} has to decrease at higher temperatures to lower the crystal growth rates (compared to the Arrhenius fit extrapolated from the region with growth rates below $10\,\mu m\,s^{-1}$) such that they remain below the crystal growth

rates of Ge_8Sb_{92}, which in turn should remain below the ones of Ge_7Sb_{93} and Ge_6Sb_{94}. Indeed, by applying our method to determine the temperature increase due to laser heating, we measure crystal growth rates showing this natural evolution with the ones of Ge_9Sb_{91} remaining below Ge_8Sb_{92}, etc. (see Fig. 4.3). In this way Ge_9Sb_{91} shows most pronounced non-Arrhenius behavior, whereas Ge_6Sb_{94} has to show most pronounced Arrhenius behavior. Actually, this is also our justification for making the explicit assumption that Ge_6Sb_{94} keeps its Arrhenius behavior also during laser heating. Otherwise we were not able to estimate the temperature increase due to laser heating. This whole scheme seems like a circle reasoning, but the combined results in Fig. 4.3 for the various GeSb alloys show that there is in principle no alternative solution, i.e. the result has to be that Ge_9Sb_{91} shows most pronounced non-Arrhenius behavior, whereas Ge_6Sb_{94} has to show most pronounced Arrhenius behavior. Interesting to note is that only in the last few years crystal growth rates at sufficiently different temperatures have been determined for phase-change films (although generally indirectly), such that non-Arrhenius behavior could be established. [3, 8] In this respect, the result for Ge_9Sb_{91} is not unexpected, but it is the first microscopy-based result, where crystal growth has been measured directly and shows non-Arrhenius behavior. On the other hand, very recently a smart method was demonstrated, showing that the crystal growth rate for the AgInSbTe phase-change material (that is also a well-known fast-growth-type PCM, like our GeSb alloys) follows strict Arrhenius behavior for over eight orders of magnitude (from $\sim$10 nm s^{-1} to $\sim$1 m s^{-1}). [4] In this respect, the assumption that Ge_6Sb_{94} follows strict Arrhenius behavior between 100 nm s^{-1} and 3 mm s^{-1} (over four orders of magnitude) is also certainly possible.

4.3.1 Viscosity and fragility

Recently, interesting work has been done on studying the crystal growth rate, viscosity, and coupled, the fragility of phase-change materials at high temperatures, relevant to phase-change memory applications. [3, 4] Using Flash Differential Scanning Calorimeter (DSC) Orava et al. studied the widely used, nucleation-dominated, phase-change material $Ge_2Sb_2Te_5$over a large temperature range, making it possible to study the crystallization at high crystal growth rates. [3] The downside of using this method is that several assumptions were needed to extract the crystal growth rates from the DSC measurements, where it is particularly difficult to distinguish between the contribution of nucleation and growth. However, they showed nicely that using the new Flash DSC technique it is well possible to study a phase-change material at high temperatures and that $Ge_2Sb_2Te_5$exhibits a strongly non-Arrhenius growth dependence and high fragility above the glass transition temperature. [3] A more direct approach was done by Salinga et al. using laser-based time-resolved reflectivity measurements. [4] They showed

that the fast-growth material AgInSbTe exhibits a strong Arrhenius behavior over eight order of magnitude, also close to the maximum growth rate. Their whole analysis indicated that AgInSbTe should have an extremely high fragility. Both articles derive the viscosity from the measurement data to study the crystallization properties near the melting temperature.

To calculate the viscosity $\eta(T)$ from the crystal growth rate $u(T)$ we use the following equation: [4, 9]

$$\eta(T) = \frac{4 r_{\text{atom}} k_{\text{B}} T}{3\pi\lambda^2 R_{\text{hyd}} u(T)} \left(1 - \exp\left(-\frac{\Delta G(T)}{k_{\text{B}} T}\right)\right) \tag{4.1}$$

with r_{atom} the atomic radius (∼1.5 Å), λ the diffusional jump distance (∼1 Å), R_{hyd} the hydrodynamic radius (∼0.5 Å) and k_{B} the Boltzmann constant. These values are based on those reported for AgInSbTe. [4] The Thomson-Spaepen approximation is used to estimate the gain in Gibbs free energy $\Delta G(T)$: [10]

$$\Delta G(T) = \Delta H_{\text{m}} \frac{T_{\text{m}} - T}{T_{\text{m}}} \left(\frac{2T}{T_{\text{m}} + T}\right) \tag{4.2}$$

with ΔH_{m} the heat of fusion (∼0.22 eV at^{-1}) [11] and T_{m} the melting temperature (∼882 K for Ge_8Sb_{92} and ∼878 K for Ge_9Sb_{91}). [12]

The viscosity of glass-forming liquids can be modeled by: [13]

$$\log_{10}\eta(T) = \log_{10}\eta_\infty + (12 - \log_{10}\eta_\infty)\frac{T_{\text{g}}}{T} \exp\left[\left(\frac{m}{12 - \log_{10}\eta_\infty} - 1\right)\left(\frac{T_{\text{g}}}{T} - 1\right)\right] \tag{4.3}$$

with η_∞ the infinite temperature viscosity ($\log_{10}\eta_\infty \approx -3$), T_g the glass transition temperature and m the fragility.

The crystal growth rates measured for Ge_8Sb_{92} and Ge_9Sb_{91}, shown in Fig. 4.3, were used to calculate the viscosity as function of temperature using Eq. (4.1). The results are shown in Fig. 4.4. Using the model proposed by Mauro et al. (Eq. (4.3)) the data is fitted and the fragility m is obtained for both alloys. For Ge_8Sb_{92} $m \approx 61$ and $m \approx 59$ for Ge_9Sb_{91}. To obtain a good fit the glass transition temperature was set to ∼382 K for Ge_8Sb_{92} and ∼395 K for Ge_9Sb_{91}.

Compared with AgInSbTe [4] and $Ge_2Sb_2Te_5$ [3] the fragility is significantly lower, indicating that these GeSb alloys are a stronger liquid than $Ge_2Sb_2Te_5$and AgInSbTe. No literature data could be found for the $T_g$of Ge_8Sb_{92} and Ge_9Sb_{91}. Comparing with $Ge_{12}Sb_{88}$, for which a $T_g$of ∼466 K has been reported, [11] the obtained values seem plausible.

4.3.2 Extrapolating crystal growth rates

The popular Arrhenius model, also applied in this thesis, is often not valid for the entire temperature regime of interest for a specific material. As shown in Fig. 4.3, if Arrhenius-type

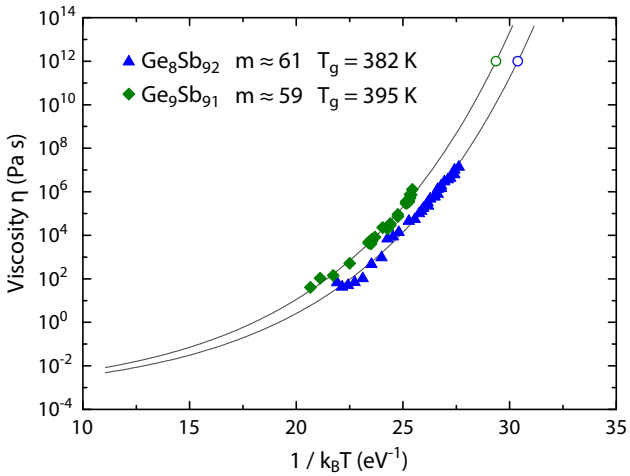

Figure 4.4 | Viscosity as function of reciprocal temperature for Ge_8Sb_{92} (blue symbols) and Ge_9Sb_{91} (green symbols). Using Eq. (4.1) the viscosity is calculated from the crystal growth rates as shown in Fig. 4.3 (diamond and triangles). The viscosity is fitted with Eq. (4.3) (gray solid lines). The glass transition temperatures obtained from the fits for Ge_8Sb_{92} and Ge_9Sb_{91} are ∼382 K and ∼395 K, respectively (open circles).

growth behavior would hold up to the melting temperature, Ge_9Sb_{91} should have a higher crystal growth rate at ∼200 °C than the other three measured GeSb compositions. From literature we expect a tendency that GeSb compositions with less germanium show higher maximum growth rates instead. [7] Indeed, using the laser induced crystallization measurements we do find non-Arrhenius growth behavior for crystal growth rates above the range probed with standard isothermal measurements. This does, however, mean that the growth rates cannot be extrapolated toward the melting temperatures, of interest for applications, using Arrhenius fits.

The viscosity model does give a good fit for the combined isothermal and laser measurements, and is therefore a good candidate model for extrapolating the crystal growth rates to higher temperatures. By reversing Eq. (4.1) and plugging in Eq. (4.3) with the parameters m and T_g obtained for Ge_8Sb_{92} and Ge_9Sb_{91} a prediction is made for the crystal growth rate at temperatures approaching the melting temperature and additionally maximum growth rates are found for both alloys (see Fig. 4.5). The maximum growth rate found in this way for Ge_8Sb_{92} is $u_{max} = 15\,\mathrm{m\,s^{-1}}$.

The obtained maximum growth rate is lower than what could be expected from ref. [7] where a growth rate of ∼58 m s^{-1} was measured for $Ge_{10}Sb_{90}$ films, which should have a lower maximum crystal growth rate due to the higher concentration of germanium. The experiments present in ref. [7] were, however, done on melt-quenched films, whereas our experiments are

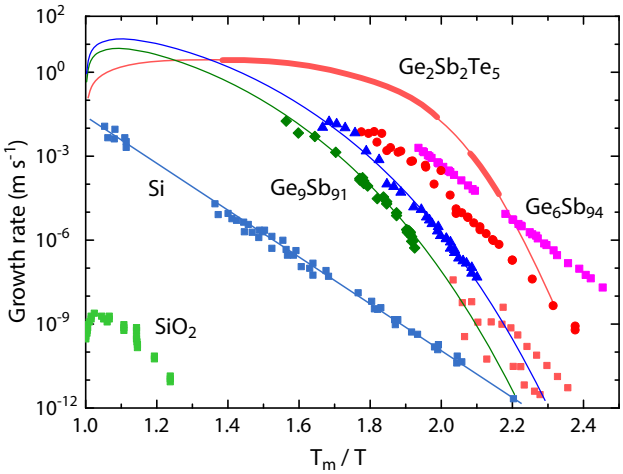

Figure 4.5 | Crystal growth rates a function of reciprocal temperature for different materials. The results for Ge_6Sb_{94} to Ge_9Sb_{91} obtained in the previous and current chapter are compared with the crystal growth rates for $Ge_2Sb_2Te_5$, Si and SiO_2. Like $Ge_2Sb_2Te_5$, the Ge_8Sb_{92} and Ge_9Sb_{91} alloys show fragile behavior. On the other hand, Si shows rather non-fragile behavior. The solid green and blue lines are the growth rates extracted from the viscosity fit by reversing Eq. (4.1) for Ge_8Sb_{92} and Ge_9Sb_{91}. The data for $Ge_2Sb_2Te_5$, Si and SiO_2 was adapted from [16].

done on as-deposited material. In general, a shift to a lower crystallization temperature can be expected when going from an as-deposited film to a melt-quenched film. For example, for $Ge_{15}Sb_{85}$ a decrease of 42 K has been reported. [14] Earlier work from our group for Ge and In doped SbTe alloys showed that the same crystal growth rates occurred at temperatures about 25 K lower for melt-quenched than for as-deposited materials. [15]. Such shifts to lower temperatures make it possible to reach, by our model, the maximum growth rate like the 58 m s^{-1} reported.

For phase-change materials it is desirable to have as high as possible maximum crystal growth rates allowing fast switching of the memory, but also crystal growth rates that become extremely slow at the maximum allowed operating temperature of the memory (like 100 °C) to give good data retention to the memory. Comparing the different materials in Fig. 4.5, these conflicting requirements seem to be best met by the Ge_8Sb_{92} and Ge_9Sb_{91} alloys. For the most popular phase-change material $Ge_2Sb_2Te_5$ it is indeed known that both its retention behavior and its switching speeds are rather modest, inspiring strong attempts to find materials with improved phase-change properties. Fig. 4.5 of course only shows a (small) part of the story, because for instance (i) it is known that GeSb alloys are more prone to phase separation than $Ge_2Sb_2Te_5$ and therefore cell endurance (cyclability) is clearly more an issue for the

former alloys and (ii) the results for all the phase-change materials shown in Fig. 4.5 hold for as-deposited films and have limited value, because in practice always melt-quenched materials are used which generally show different behavior (e.g. lower crystallization temperature as explained above).

4.4 Conclusions

We have successfully demonstrated a method to optically study crystal growth rates at high temperatures, almost four orders of magnitude higher than reachable with previous standard isothermal measurements, by combining laser and isothermal heating with high speed optical microscopy. The local temperature increase due to the laser pulse was estimated providing an upper and lower bound for the temperature at a certain growth rate. After transposing the crystal growth rate versus temperature to the viscosity versus temperature a good fit was obtained for the fragile behavior of the viscosity ($m \approx 60$), also allowing for a prediction of the crystal growth rates with a certain maximum rate ($15\,\mathrm{m\,s^{-1}}$) at temperatures near the melting temperature.

References

[1] V. Weidenhof, I. Friedrich, S. Ziegler, M. Wuttig, *Journal of Applied Physics* **89**, 3168 (2001).

[2] B. J. Kooi, J. T. M. De Hosson, *Journal of Applied Physics* **95**, 4714 (2004).

[3] J. Orava, A. L. Greer, B. Gholipour, D. W. Hewak, C. E. Smith, *Nature Materials* **11**, 279 (2012).

[4] M. Salinga, E. Carria, A. Kaldenbach, M. Bornhöfft, J. Benke, J. Mayer, M. Wuttig, *Nature Communications* **4** (2013).

[5] D. Z. Dimitrov, C. Babevab, S.-T. Chenga, W.-C. Hsua, M.-H. Hsieha, S.-Y. Tsaia, High-speed reversible phase-change optical recording in GeSb – based alloys, *European\Phase Change and Ovonics Symposium* (2004).

[6] Brewster, D., *Philosophical Transactions of the Royal Society of London* (1815), vol. 105, pp. 125–159.

[7] D. J. Adelerhof, Media development for DVD+RW phase change recording, *European\Phase Change and Ovonics Symposium* (2004).

[8] N. Ciocchini, D. Ielmini, Crystallization phenomena in phase change memories: non-arrhenius kinetics, modeling and novel applications, *European\Phase Change and Ovonics Symposium* (2013).

[9] D. Turnbull, J. C. Fisher, *The Journal of Chemical Physics* **17**, 71 (1949).

[10] C. V. Thompson, F. Spaepen, *Acta Metallurgica* **27**, 1855 (1979).

[11] J. A. Kalb, Crystallization kinetics in antimony and tellurium alloys used for phase change recording, Ph.D. thesis, RWTH Aachen University, Aachen (2006).

[12] R. W. Olesinski, G. J. Abbaschian, *Bulletin of Alloy Phase Diagrams* **7**, 219 (1986).

[13] J. C. Mauro, Y. Yue, A. J. Ellison, P. K. Gupta, D. C. Allan, *Proceedings of the National Academy of Sciences* **106**, 19780 (2009). PMID: 19903878.

[14] L. van Pieterson, M. H. R. Lankhorst, M. van Schijndel, A. E. T. Kuiper, J. H. J. Roosen, *Journal of Applied Physics* **97**, 083520 (2005).

[15] J. L. Oosthoek, B. J. Kooi, J. T. De Hosson, D. J. Gravesteijn, K. Attenborough, R. A. Wolters, M. Verheijen, Crystallization studies of doped SbTe phase-change thin films and PRAM line cells: Growth rate determination by automated TEM image analysis, *European\Phase Change and Ovonics Symposium* (2009).

[16] M. Wuttig, M. Salinga, *Nature Materials* **11**, 270 (2012).

Chapter 5

Stress-induced crystallization

Abstract. In this chapter we demonstrate the large effects of moderate stresses on the crystal growth rate in Ge-doped Sb phase-change thin films using direct optical imaging. For Ge_6Sb_{94} and Ge_7Sb_{93} phase-change films, a large increase in crystallization temperature is found when using a polycarbonate substrate instead of a glass substrate. This increase is attributed to the tensile thermal stress induced in the phase-change film due to a difference in thermal expansion coefficient between the film and the polycarbonate substrate. By applying a uniaxial compressive stress to a phase-change film, we show and explain that isotropic crystal growth becomes unidirectional (perpendicular to the uniaxial stress) with a strongly enhanced growth rate. This is a direct proof that modest stresses can have large consequences for the amorphous phase stability and for the crystal growth rates, and these stresses are thus highly relevant for memories based on phase-change materials.

5.1 Introduction

Phase-change materials (PCMs) have aroused strong interest due to their suitability for electrical nonvolatile memory devices. [1–4] The ability to switch in tens of nanoseconds between the amorphous and crystalline phases at elevated temperatures used for switching while still having a long retention at the basic operating temperatures (e.g., $< 100\,°C$) in combination with the excellent prospects for downscaling makes PCM devices promising for next-generation memory devices and as a replacement for flash memory. [4] The stability and electrical resistance of the PCM cells are affected by stresses present in the cell, [5, 6] and it is, therefore, of great importance to understand how these stresses influence the stability of the amorphous phase and the (re)crystallization process. Here, we show for the first time direct proofs that modest compressive stresses (e.g., 70 MPa) applied to PCM thin films can accelerate the crystal growth rate at a given temperature by a factor of 60. These results are highly relevant for memory devices because such modest stresses are easily introduced in the PCM in the devices and may even vary with this magnitude on a single bit level.

Based on *Stress-Induced Crystallization of Ge-Doped Sb Phase-Change Thin Films*, G. Eising, A. Pauza and B.J. Kooi, *Crystal Growth & Design* **13**, 220 (2013)

The switching of a PCM from amorphous to crystalline is, depending on the PCM composition, accompanied by a decrease in volume of typically 5–10 %. [7] When the PCM has no degrees of freedom to expand or contract (for instance, in a memory cell) and the volume change is accommodated fully elastically, this would result in a (hydrostatic) stress on the order of GPa's. Most studied PCMs are, however, present in thin film form with a free surface, and then there is little constraint toward a dimensional change perpendicular to the surface. Only in-plane stresses on the order of a GPa can be expected. However, generally much smaller in-plane stresses are found, indicating that only a relatively small fraction of the volume change is accommodated elastically. The missing stress is thus relaxed by plastic deformation or viscous flow in the amorphous phase. For instance, approximately 9 % of the total volume decrease upon crystallization (of various SbTe alloys with a film thickness of around 50 nm) was found to be transformed into elastic in-plane stress. [8] Nevertheless, this still leads to significant in-plane stresses of 100–200 MPa.

The decrease in volume upon crystallization suggests that a compressive stress aids the crystallization process. Indeed, under hydrostatic pressure, an amorphous $Ge_2Sb_2Te_5$ film was even crystallized at room temperature. [9] However, it was also found that, when capping layers exert an in-plane compressive stress on a thin $Ge_2Sb_2Te_5$ film, the crystallization temperature was increased. [10] However, the effect of capping layers on the stress state in the PCM was not determined in these cases, only showing the direct effect that capping layers can increase the crystallization temperature, particularly for extremely thin PCM films with a thickness below 10 nm. In contrast, there is clearly more convincing evidence that, upon crystallization, always tensile stresses develop in $Ge_2Sb_2Te_5$ films and that capping layers strongly increase the magnitude of the tensile stress. [11, 12] Microcantilevers were used to act as sensors for measuring crystallization-induced density changes and stresses. [12] Still, these measurements only determine the response of the material system, but do not apply and systematically vary stresses to measure their influence on PCM properties. Here, we show for the first time the influence of applied stresses on the crystal growth in PCM films by employing a four-point bending stage and direct optical detection of the effect of applied compressive stresses. Additionally, we will show the effect softening of the substrate has on the crystal growth properties.

5.2 Experimental section

5.2.1 Samples

Samples investigated consist of 200 nm thin films with a Ge_6Sb_{94} or Ge_7Sb_{93} on a 1.3 mm thick glass or polycarbonate substrate. The films were deposited and further processed as described

in section 2.1. For the bending experiment the polycarbonate samples were cut to dimensions of 5 mm × 25 mm. For the isothermal experiments, samples with dimensions of 5 mm × 5 mm were used.

5.2.2 Four-point bending stage

To apply a uniform stress to the phase-change film a four-point bending stage was developed, see Fig. 5.1. By applying a certain deflection to the two inner supports of the four-point bending setup, a uniform moment is created in between these two inner supports. This results in a constant curvature $1/R$ of the beam within the two inner supports. For our work, only the region in between these two inner beams is relevant. Next, it is important to note that we have a (200 nm) thin film on a (1.3 mm) thick substrate. Therefore, the gradient in stress over the thickness of the whole sample during bending, which ranges from compressive on one side to tensile on the other side of the sample, can be neglected for the thin film. This results in a uniform unidirectional stress being applied in the thin film perpendicular to the bending axis. The in-plane stress σ_{bending} in a thin film on a substrate with thickness h is given by

$$\begin{aligned} \sigma_{\text{bending}} &= \frac{Md}{I}, \\ M = \frac{EI}{R},\ d &= \frac{h}{2}, \\ \Rightarrow \sigma_{bending} &= \frac{Eh}{2R}, \end{aligned} \tag{5.1}$$

with M the bending moment, d the vertical distance between the film and center of the beam, I the moment of inertia, E the Young's modulus of the polycarbonate substrate (2.3 GPa [13]), h the thickness of the beam and $1/R$ the curvature of the beam in between the two inner supports. By measuring the deflection at the center relative to the two inner beams using a vernier caliper, the curvature of the substrate is calculated from which the stress in the film can be calculated, see equation (5.1). Different stresses ranging between 10 and 120 MPa were applied by using different deflection distances. In the bending experiments, we used samples with a polycarbonate substrate.

5.3 Results and discussion

Ge_6Sb_{94} and Ge_7Sb_{93} were selected as the phase-change materials to study, since they have a crystallization temperature around 100–140 °C, [14] well below the glass transition temperature of the polycarbonate substrate of 150 °C, but still they have a stable amorphous phase at room temperature. Moreover, Ge_6Sb_{94} and Ge_7Sb_{93} are fast-growth materials having a very

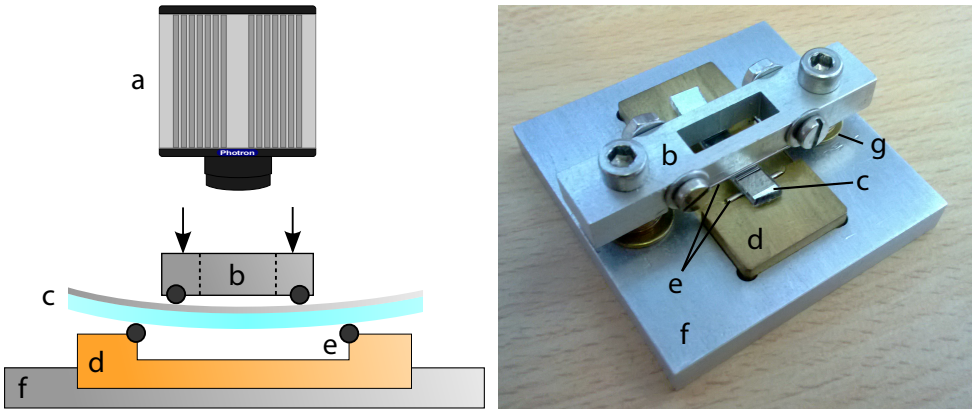

Figure 5.1 | Schematic overview of the bending stage (left) and an image of the actual bending stage (right). **a** High speed optical camera. **b** Aluminum top bar to define a certain deflection of the sample. A hole is present in the center of the bar to allow observation of the sample. Two steel rollers are the contact points with the sample to allow the sample to slide freely along the bar while bending. **c** Sample with a 200 nm thick Ge_7Sb_{93} film on a 1.3 mm thick polycarbonate substrate. **d** Brass bottom plate with two steel rollers to allow the sample to move freely. **e** Steel rollers reducing friction of the sample with the stage. **f** Aluminum mounts for the bottom plate and top plate. **g** Washers to limit the maximum deflection distance.

low nucleation rate, resulting in large crystals, whose growth can be easily monitored optically. Isothermal crystallization experiments were performed in situ for both substrates, see Fig. 5.2a. Crystal nucleation only occurred sufficiently long after the isothermal annealing temperature is reached, and therefore, the growth rates correspond to truly isothermal processes. From the recorded images, it was evident that the crystal growth rate at a certain temperature is independent of time.

Isothermal measurements for the Ge_6Sb_{94} films were performed for the glass substrates for $T = 90\,°C$ up to $T = 120\,°C$ and for the polycarbonate substrates for $T = 100\,°C$ up to $T = 135\,°C$ with steps of 5 °C. The samples were heated to the desired temperature at a rate of $20\,°C\,min^{-1}$. The temperatures were stable within 0.2 °C. For each temperature, the crystal growth rate was determined and plotted in an Arrhenius plot (see Fig. 5.2b), where linear fits provided the activation energy for growth. For both substrates similar activation energies are found: $E_g = 1.68 \pm 0.07$ eV and $E_g = 1.70 \pm 0.07$ eV for the polycarbonate and glass substrates, respectively. The intercepts are at $\ln(G) = 47.9 \pm 1.0$ and $\ln(G) = 50.5 \pm 1.0$, with G the growth rate in $\mu m\,s^{-1}$. This significant difference corresponds to a 6–7 times higher crystal growth rate on the glass substrate (compared to the polycarbonate substrate) for a given temperature in the temperature range discussed. To obtain a similar crystal growth rate on the polycarbonate

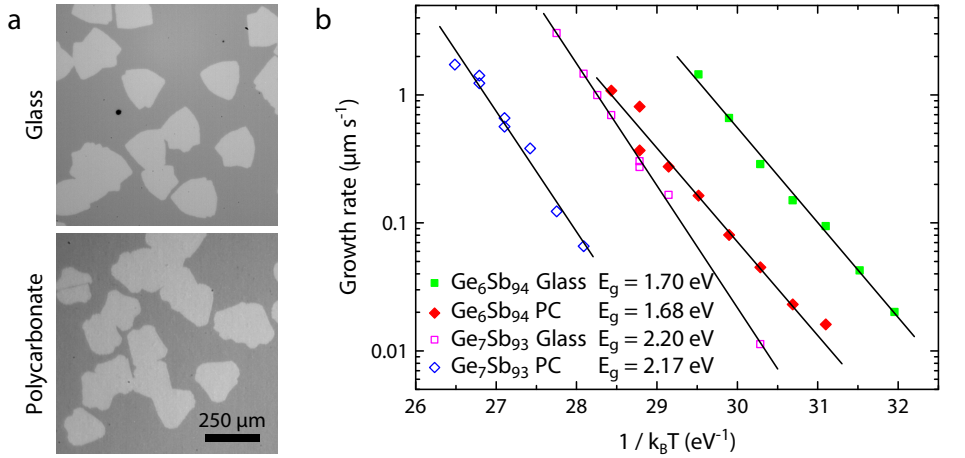

Figure 5.2 | a Optical recordings of crystal growth in a Ge_7Sb_{93} film at 140 °C on glass and polycarbonate substrates showing similar crystal growth on both substrates. **b** Crystal growth rate versus reciprocal temperature for Ge_6Sb_{94} (filled symbols) and Ge_7Sb_{93} (open symbols) phase-change films on glass (squares) and polycarbonate (diamonds) substrates. The activation energies for crystal growth found are similar for both substrates. A shift to significantly higher crystallization temperatures is found when using a polycarbonate substrate instead of a glass substrate.

substrate as that on the glass substrate, the annealing temperature has to be increased by 15 °C. Similar results were found for the Ge_7Sb_{93} films between $T = 110\,°C$ and $T = 160\,°C$. An activation energy for growth of $E_g = 2.17\,eV$ was determined for the polycarbonate substrate and $E_g = 2.19\,eV$ for the glass substrate. Similar to Ge_6Sb_{94}, there is a significant difference in the offset: $\ln(G) = 58.3 \pm 1.0$ for the polycarbonate substrate, and $\ln(G) = 62.1 \pm 1.0$ for the glass substrate. This corresponds for a given temperature to a 20–25 times higher crystal growth rate on the glass compared to the polycarbonate substrate.

This difference in offset (crystallization rate/temperature) is attributed to the difference in thermal expansion between the substrates and the phase-change film, resulting in large differences in thermal stresses. The thermal expansion coefficients for the different materials used are [13] $\alpha_{Sb} = 8.5 \times 10^{-6}\,K^{-1}$ for antimony,[1] $\alpha_{PC} = 65 \times 10^{-6}\,K^{-1}$ for polycarbonate and $\alpha_{Gl} = 9.0 \times 10^{-6}\,K^{-1}$ for glass. The in-plane biaxial stress in the phase-change film due to the difference in thermal expansion between the film and the substrate is estimated by

$$\sigma_{//} = \frac{E}{1-\nu}\Delta\alpha\Delta T \tag{5.2}$$

[1] We use α_{Sb} as the thermal expansion coefficient for the phase-change films since data could not be found for the alloys used and their composition is relatively close to pure Sb.

where E is the Young's modulus of the film (= 54.4 GPa), ν is the Poisson's ratio of the film (= 0.25), $\Delta\alpha$ the difference in thermal expansion coefficient between the substrate and the film, and ΔT is the change in temperature. In this case, it is assumed that the strain in the film completely accounts for the difference in thermal expansion between the film and the substrate and that no significant stresses develop in the substrate. Moreover, isotropic elasticity is assumed. Within this framework, an in-plane tensile stress of $\sigma \approx 400$ MPa is expected in the PCM film on the polycarbonate substrate at 115 °C, whereas the stress is almost zero on the glass substrate.

The large difference in the growth rate for a given temperature depending on the substrate can be explained by this stress difference. As the amorphous film crystallizes, an in-plane tensile strain is introduced in the crystalline phase, as outlined above. During the crystallization process, enough (thermal) energy has to be provided to the system to overcome this tensile strain. Although the thermal stresses introduced in the film due to the mismatch with the substrate will relax, a significant elastic stress will remain. This stress, depending on its sign, will lower or increase the tensile strain that has to be overcome during crystallization and thus the energy needed for crystallization. This results, in agreement with the observations, in a significantly lower crystal growth rate at a given temperature for in-plane tensile stresses induced by the polycarbonate substrate in the PCM film compared to the fairly stress-free state in the case of the glass substrate. Direct proof that significant tensile stresses are present in the PCM films on polycarbonate substrates comes from the observations that, at high heating rates, cracks develop in the PCM film and, for the same heating rates, cracks were not observed in the PCM films on the glass substrates.

When the polycarbonate substrate is heated above the glass transition temperature T_g a transition is found from a tensile stress to a compressive stress in the film. Additionally, buckling in both the amorphous and crystalline surface is observed. In appendix A the observed measurements are explained in more detail.

A more direct and controllable method to prove the large influence of stresses on the crystal growth is to use a four-point bending stage, as described in the experimental section. We verified that, in all cases, the film stays attached to the substrate and thus follows the elastic strains of the substrate. We could only use compressive stresses in the PCM films, because when we tried tensile stresses, the PCM films showed cracks, which prevent any relevant analysis of the influence of tensile stresses on the growth rate.

The whole stage, including the sample with a Ge_6Sb_{94} film, was heated to 115 °C before the bending was performed to prevent relaxation of the applied stresses during the heating and annealing process. This turned out to be crucial. After small, but optically clearly visible, crystals had formed in the film with an average diameter of 30 µm, the compressive bending stress was applied. As soon as the stress was applied, it was clearly visible that the crystal growth

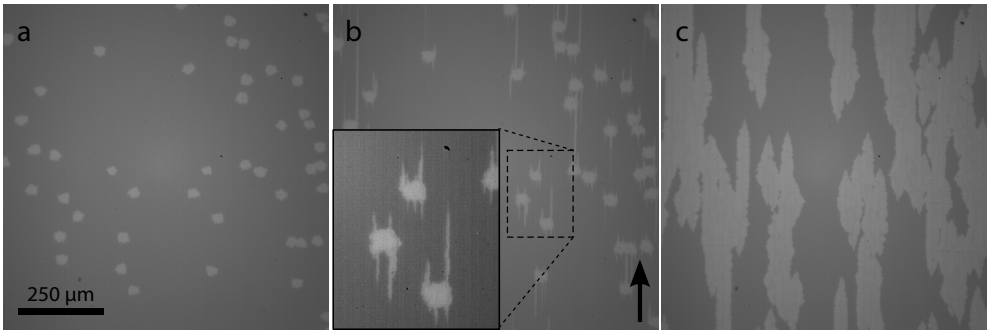

Figure 5.3 | Crystal growth during a 70 MPa bending experiment at 115 °C in a Ge_6Sb_{94} film on a polycarbonate substrate as monitored optically. The arrow indicates the direction of the bending axis; the applied unidirectional in-plane compressive stress is perpendicular to the bending axis. **a** Isotropic crystal growth is visible before bending. **b** 75 s after the onset of bending the sample, crystal growth parallel to the bending axis is clearly visible. This one-dimensional growth occurs at a significantly higher speed than the isotropic growth before bending. **c** After 270 s, crystal growth has become nearly two-dimensional again, resulting in elongated crystals.

became severely anisotropic; see Fig. 5.3. For small stresses (< 50 MPa), the crystals became diamond-shaped, elongated along the bending axis. For larger stress, the crystals initially only grow in one direction at a much higher growth rate than before bending (Fig. 5.3b), resulting in long thin crystalline needles parallel to the bending axis originating from the isotropic grown crystals already present. After the initial fast one-directional growth, the growth rate decreased and the crystal growth continued in all directions (Fig. 5.3c). The same effects were observed in Ge_7Sb_{93} films.

In agreement with the isothermal experiments, where in-plane thermal tensile stresses increased the crystallization temperature, we now see during the bending experiments a strong increase in crystal growth rate at a certain temperature, that is, a decrease in crystallization temperature when compressive stresses are applied.

For understanding the effect on crystallization of applying a 1D compressive stress to a thin film, the analogy with applying a 1D tensile stress on crack opening and crack growth in a thin film is very instrumental. Figure 5.4 shows a schematic representation of this clear analogy. Under tensile stress, the original circular crack grows in a direction perpendicular to the applied stress in order to relax the residual stress in the system. Similarly, the original circular crystal grows perpendicular to the applied compressive stress in order to relax the residual stress in the system for the general case that the crystalline phase has a higher density than the amorphous phase.

The crystal growth during the bending experiment was observed and analyzed as described

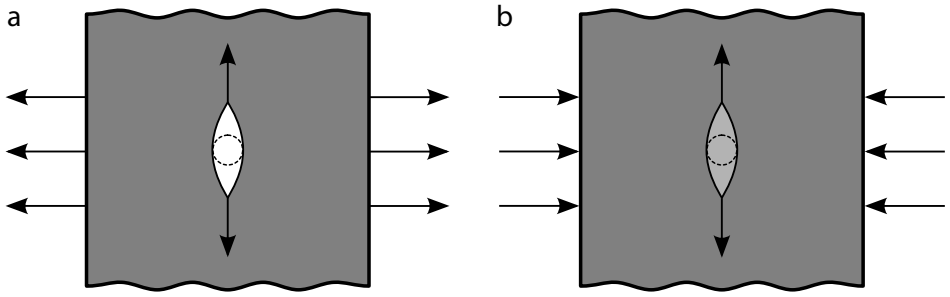

Figure 5.4 | Analogy between **a** crack growth in a plate under a one-dimensional (1D) tensile stress and **b** crystallization under a 1D compressive stress.

above. However, a drawback of the planar fitting used is that it gives a large error at the edges; a sharp change in growing direction cannot be properly fitted with a plane surface. Therefore, because of the shape of the long thin crystals, line profiles were taken along the length or width of the crystals, as described in section 2.3.2 shown in Fig. 5.5. A linear fit was applied to these line profiles to obtain the crystal growth rates.

Figure 5.5a,b shows the time mappings of the bending experiments for an applied compressive bending stress of 40 and 70 MPa. For 70 MPa, we can clearly observe that there is a strong preference for unidirectional growth; the crystals are elongated in the direction parallel to the bending axis. Line profiles taken from the time mappings along the width of the crystals are shown in Fig. 5.5c,d. For both 40 and 70 MPa we obtain a crystal growth rate $v = 0.11 \pm 0.01\,\mu m\,s^{-1}$ parallel to the bending axis, which corresponds to the crystal growth rate at 115 °C for a nonbended sample; that is, the applied bending does not change the growth rate perpendicular to the bending axis. For the growth parallel to the bending axis, we do see a difference between bended and nonbended samples. When a stress of 40 MPa is applied, we initially observe a growth rate of $0.4\,\mu m\,s^{-1}$. After 70 s the crystal growth rate decreases relatively abruptly to $0.15\,\mu m\,s^{-1}$. This is still higher than the growth rate found perpendicular to the bending axis and the nonbended growth rate. Applying a bending stress of 70 MPa leads to an initial crystal growth rate of $6.7\,\mu m\,s^{-1}$, which is 60 times higher than that for the nonbended case. After 20 s, the crystal growth rate decreases relatively abruptly to $0.26\,\mu m\,s^{-1}$, which is still more than twice the unstressed crystal growth rate.

A direct cause for the observed abrupt transition to a lower growth rate is the relaxation of the applied compressive stress, reducing the driving force for accelerated unidirectional crystallization. This relaxation is attributed to crystallization of the phase-change material and to plastic deformation in the substrate as the sample is at an elevated temperature. We have proof for plastic deformation in the polycarbonate substrate, because, when the sample is removed

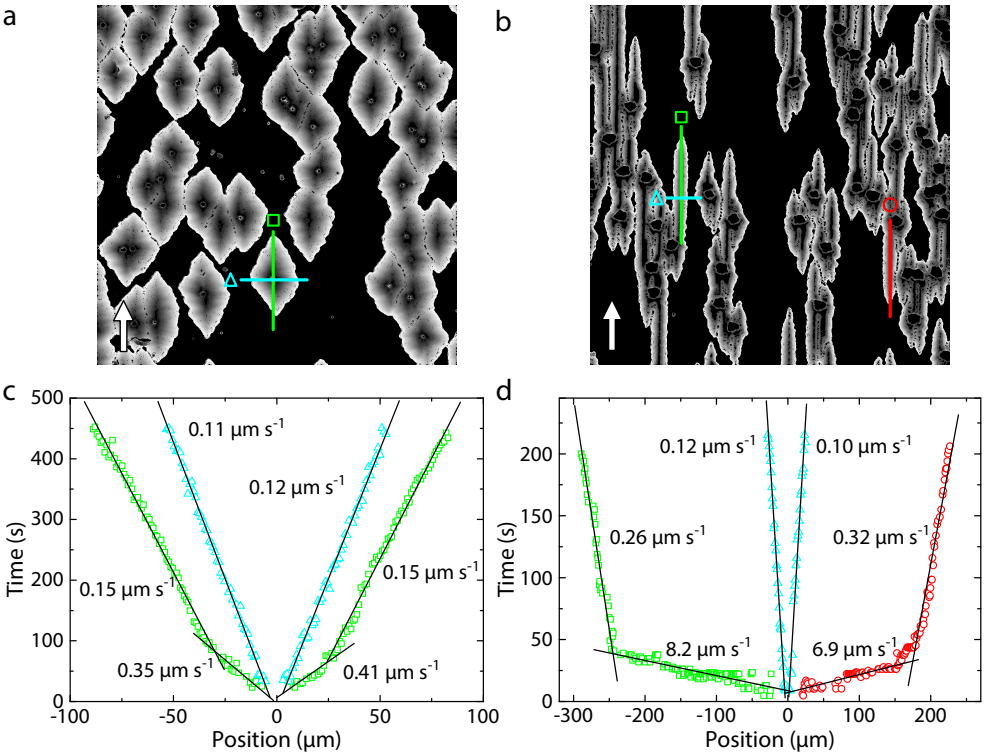

Figure 5.5 | a, b Time mappings with the white arrow indicating the bending axis. **c, d** Line profiles taken along the corresponding lines shown in **a** and **b** for a compressive bending stress of **a, c** 40 MPa and **b, d** 70 MPa. After an initially increased crystal growth rate parallel to the bending direction (squares and circles), the crystal growth rate decreases strongly but remains significantly higher than the unstressed growth perpendicular to the bending axis (triangles).

from the bending stage after the bending experiment at elevated temperature, the sample only partly flexes back and thus partly remains bended. Moreover, there is experimental data [15] that stress relaxation in PCMs at the applied temperatures takes considerably longer (several thousand seconds) than the times of our experiments (not more than a few hundred seconds). This explains why the growth rate in the PCM film, after the initial abrupt drop in growth rate due to relaxation of the substrate, is still higher at a given temperature than that for the stress-free case, because stress relaxation in the amorphous phase of the PCM is not completed yet. We cannot measure these long times needed for full stress relaxation, that is, when the growth rate in all directions becomes the same, because the film is already fully crystallized much earlier.

We have additional evidence that the effect of bending stress on the increase in growth rate is highly nonlinear; see Fig. 5.6. After bending stresses are applied, crystals in the phase-change

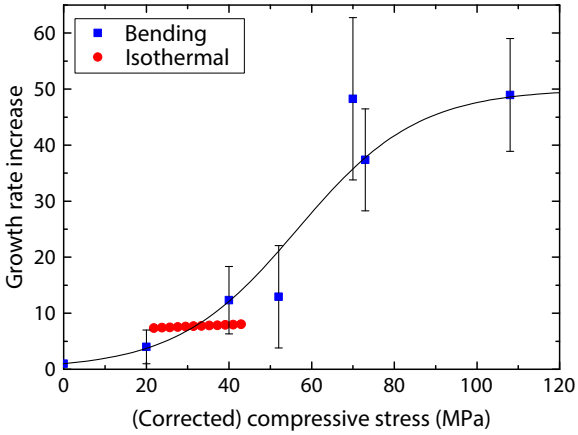

Figure 5.6 | Growth rate increase (multiplication factor) for bending (blue squares) and isothermal (red circles) experiments performed on Ge_6Sb_{94} films as a function of applied compressive stress, where, for the isothermal measurements, the calculated stress has been reduced by 90 % to match the data with the results from the bending experiments. For higher compressive bending stresses, the growth rate increase levels off. The solid black line is a guide to the eye.

films develop into elongated shapes with their long axis parallel to the bending axis. These shapes, therefore, provide a measure for the increase in crystal growth rate due to the applied stresses. By measuring the aspect ratio, that is, the length divided by the width of the crystals at a fixed time after the bending was applied, a lower bound for this increase (multiplication factor) in growth rate due to the applied stresses was obtained. It is a lower bound because the crystals are measured at a time when the growth parallel to the bending axis has lost (due to stress relaxation already in an earlier stage) its initial fast rate. Figure 5.6 shows that the increase in growth rate is highly nonlinear: up to 40–50 MPa, the increase is modest; then, in the regime from 40 to 70 MPa, the increase becomes very pronounced. However, this increase then levels off at stresses beyond 100 MPa, probably because increasing stress beyond this value only causes additional plastic deformation and not an increasing elastic stress required to alter the growth rate. The relatively large error bars in Fig. 5.6 are a result of the large spread in aspect ratios found in the experimental images, and this large spread also reflects the different times crystals with accelerated unidirectional growth started to grow (nucleated) out of the earlier isotropically grown crystals. Crystals that start to grow immediately after applying the bending stress have the highest aspect ratio, and crystals that start to grow later experience a condition with more stress relaxation, and will thus have a lower aspect ratio.

The results in Figs 5.5 and 5.6 demonstrate that compressive stresses in the range of 70–120 MPa accelerate the crystal growth at least 40 times. From the isothermal experiments,

where the stress difference in the film due to the different substrates was calculated to be in the order of 400 MPa, we see a 6-fold increase in growth rate for the Ge_6Sb_{94} films on the glass compared to the polycarbonate substrates. For the bending experiments, we find the same increase in growth rate already at a compressive bending stress of only 20–40 MPa. If we assume that the measurement of the growth rate increase during the bending experiment, as shown in Fig. 5.6, matches the corresponding growth rate increase found from the isothermal experiments, we find that the calculated stresses from the isothermal experiments have to be reduced by 90 % to match the data obtained from bending experiments. This would mean that the thermal stresses induced in the phase-change film due to the difference in thermal expansion coefficient between substrate and film are relaxed by about 90 % during the heating process. This amount of relaxation matches well with the results (that is, 91 % relaxation) found in ref. [8].

5.4 Conclusions

Using optical microscopy, we have demonstrated that stresses in phase-change films have a pronounced effect on the crystal growth rate. For Ge_6Sb_{94} and Ge_7Sb_{93} phase-change films, a large increase in crystallization temperature was found when using a polycarbonate substrate instead of a glass substrate. This increase is attributed to the tensile thermal stress induced in the phase-change film due to a difference in thermal expansion coefficient between the film and the polycarbonate substrate. We also demonstrated that applying a compressive bending stress of only 70 MPa already leads to a 60-fold faster crystal growth parallel to the bending axis, that is, perpendicular to the applied compressive stress. This is a direct proof that modest stresses can have large consequences for the amorphous phase stability and for the crystal growth rates, and these stresses are thus highly relevant for memories based on PCM.

Appendix A Star-shaped crystal growth

One of the initial experiments on Ge_7Sb_{93} films on a polycarbonate substrate showed quite peculiar crystal growth when the substrate temperature was raised to 180 °C. Up to the glass transition temperature of polycarbonate ($T_g \approx 150$ °C) [13] isotropic growth was observed, similar to the crystal growth shown in Figs. 2.2 and 5.2a. Above this temperature we observed initially isotropic growth, after the crystals reached a certain size, star-shaped crystals were observed (see Fig. 1.1). Figure 5.7 shows a close up of these star-shaped crystals. In the amorphous phase temporarily buckling is observed parallel to the growth directions of the star tips. In the crystalline phase buckling is also observed, now perpendicular to the growth direction. The growth rate of the crystalline tips was determined to be 5 to 10 times higher than the growth rate of the initially isotropic growing crystals. Additionally, the growth direction of the tips seems to be influenced by other nearby tips, resulting in a parallel alignment of nearby tips with respect to each other.

There are several mechanism involved, leading to the observed growth pattern. The main difference with the experiments described earlier in this chapter, is the state of the substrate. Above the T_g of polycarbonate substrate, the substrate goes from a glassy state to a rubber-like state before it melts at ~240 °C. The tensile stresses introduced in the film due to the difference in thermal expansion coefficient are even further relaxing than the ~90 % shown in Fig. 5.6. This was confirmed by the observation of closing cracks which initially emerged in the some of the films during heating with a high temperature ramp rate, due to the significant difference between thermal expansion coefficient of the substrate and film. Buckling has also been found in amorphous phase-change Ge_9Sb_{91} phase-change films on polycarbonate after waiting for a sufficient time, where it is noted that these films do not crystallize at 180 °C. Buckling of a film on an elastic substrate is caused by a compressive stress present in the film, with the wave pattern perpendicular to the maximum compressive stress. [16] The buckling observed in the amorphous films indicates that not only the tensile stresses have been relaxed, but that the substrate is locally shrinking with respect to the phase-change film, and a compressive stress in the film is induced. A possible explanation for the local shrinking of the substrate could be the presence of compressive residual stresses in the polycarbonate substrate. These stresses are introduced in the substrate during the rapid cooling after the injection molding used for fabrication of the polycarbonate disc. [17] Near and above $T_g$the polymer chains are able to move and relax the stresses, resulting in shrinkage of the substrate.

The temporarily buckling found around the crystal tips indicate an anisotropic compressive field around these tips. This anisotropy is explained by the increase of the Young's modulus of the phase-change material upon crystallization. [11, 18] The local change in Young's modulus

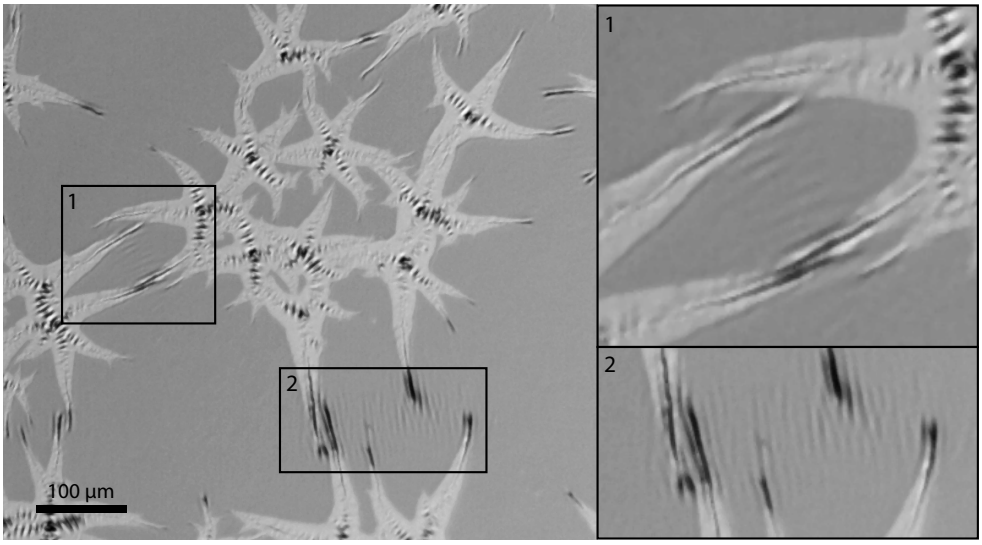

Figure 5.7 | Star-shaped crystals in a 200 nm thick Ge_7Sb_{93} phase-change film on a polycarbonate substrate. The substrate has been heated to 180 °C. Inset 1 and 2 show the presence of wrinkling in both the amorphous phase, parallel to the crystalline tips, and in the crystallized phase, perpendicular to the crystal growth direction.

causes a reduction in the compressive stress in the growth direction of the tip, [19] disturbing the isotropic stress field. The compressive stress perpendicular to the growth direction is now larger than the compressive stress parallel to the growth direction and causes buckling around the crystalline tip. Additionally, it causes buckling to occur in the amorphous phase in a radius of ∼30 µm around the tip. In time the difference in stresses relax and the buckling disappears. The presence of the anisotropic stress field causes the crystal growth to favor the direction perpendicular to the stress field. Tips are being influenced by the stress field induced by other tips, causing them to align if they are close enough.

Permanent buckling is found in the crystalline phase parallel to the growth direction. This suggests that this buckling is a time dependent process caused by the substrate being able to flow, while the film remains stiff. A compressive stress has to build up in the film, leading to the buckling. The permanent buckling is not observed in the amorphous phase for the sample presented in Fig. 5.7 as the sample is fully crystallized before enough compressive stress has been build up in the amorphous phase.

The preference to grow star-shaped crystals is probably connected to the underlying triagonal crystal structure which prefers star-shaped crystals with initially angles of 60° between the six crystal tips. The individual tips show bifurcation with a preference to split a single tip in to

three new tips with again angles of 60° between the new tips. The six initial tips of the crystals is coupled to the strong preference of the crystals to nucleate with their [0001] axis oriented perpendicular to the film surface, as was shown in the TEM results of chapter 3.

References

[1] M. Wuttig, N. Yamada, *Nature Materials* **6**, 824 (2007).

[2] S. Raoux, *Annual Review of Materials Research* **39**, 25 (2009).

[3] D. Lencer, M. Salinga, M. Wuttig, *Advanced Materials* **23**, 2030 (2011).

[4] G. W. Burr, M. J. Breitwisch, M. Franceschini, D. Garetto, K. Gopalakrishnan, B. Jackson, B. Kurdi, C. Lam, L. A. Lastras, A. Padilla, B. Rajendran, S. Raoux, R. S. Shenoy, *Journal of Vacuum Science & Technology B* **28**, 223 (2010).

[5] M. N. Schneider, P. Urban, A. Leineweber, M. Döblinger, O. Oeckler, *Physical Review B* **81**, 184102 (2010).

[6] a) S. Braga, A. Cabrini, G. Torelli, *Applied Physics Letters* **94**, 092112 (2009); b) M. Mitra, Y. Jung, D. S. Gianola, R. Agarwal, *Applied Physics Letters* **96**, 222111 (2010).

[7] W. K. Njoroge, H.-W. Woltgens, M. Wuttig, *Journal of Vacuum Science & Technology A* **20**, 230 (2002).

[8] T. P. L. Pedersen, J. Kalb, W. K. Njoroge, D. Wamwangi, M. Wuttig, F. Spaepen, *Applied Physics Letters* **79**, 3597 (2001).

[9] M. Xu, Y. Meng, Y. Q. Cheng, H. W. Sheng, X. D. Han, E. Ma, *Journal of Applied Physics* **108**, 083519 (2010).

[10] R. E. Simpson, M. Krbal, P. Fons, A. V. Kolobov, J. Tominaga, T. Uruga, H. Tanida, *Nano Letters* **10**, 414 (2010).

[11] I.-M. Park, J.-K. Jung, S.-O. Ryu, K.-J. Choi, B.-G. Yu, Y.-B. Park, S. M. Han, Y.-C. Joo, *Thin Solid Films* **517**, 848 (2008).

[12] Q. Guo, M. Li, Y. Li, L. Shi, T. C. Chong, J. A. Kalb, C. V. Thompson, *Applied Physics Letters* **93**, 221907 (2008).

[13] W. Martienssen, H. Warlimont, eds., *Springer Handbook of Condensed Matter and Materials Data* (Springer, Heidelberg, 2005).

[14] S. Raoux, C. Cabral, L. Krusin-Elbaum, J. L. Jordan-Sweet, K. Virwani, M. Hitzbleck, M. Salinga, A. Madan, T. L. Pinto, *Journal of Applied Physics* **105**, 064918 (2009).

[15] I.-M. Park, J.-Y. Cho, T.-Y. Yang, E. S. Park, Y.-C. Joo, *Japanese Journal of Applied Physics* **50**, 061201 (2011).

[16] a) H. Mei, R. Huang, J. Y. Chung, C. M. Stafford, H.-H. Yu, *Applied Physics Letters* **90**, 151902 (2007); b) N. Bowden, S. Brittain, A. G. Evans, J. W. Hutchinson, G. M. Whitesides, *Nature* **393**, 146 (1998).

[17] a) R. Wimberger-Friedl, *Polymer Engineering & Science* **30**, 813–820 (1990); b) R. Wimberger-Friedl, J. G. De Bruin, *Journal of Polymer Science Part B: Polymer Physics* **31**, 1041–1049 (1993); c) T.-H. Wang, W.-B. Young, *European Polymer Journal* **41**, 2511 (2005).

[18] Y. Won, J. Lee, M. Asheghi, T. W. Kenny, K. E. Goodson, *Applied Physics Letters* **100**, 161905 (2012).

[19] W. T. S. Huck, N. Bowden, P. Onck, T. Pardoen, J. W. Hutchinson, G. M. Whitesides, *Langmuir* **16**, 3497 (2000).

Chapter 6

Electrical surface properties

Abstract. The electrical properties of amorphous-crystalline interfaces in phase-change materials are investigated in this chapter using surface scanning potential microscopy. Analysis of GeSb systems indicates that the surface potential of the crystalline phase is ∼30–60 mV higher than that of the amorphous phase. This potential asymmetry is explained qualitatively by the presence of a Schottky barrier at the amorphous-crystalline interface and is also supported by quantitative Schottky model calculations.

6.1 Introduction

Rewritable optical disk technology, well known from the CD, DVD, and Blu-ray disk formats, has been matured during the last two decades and has shown considerable progress. For example in 2007 alone, ∼10 billion rewritable optical disks were sold, which were used to read, write, and erase data. [1] These erasable optical disks employ phase-change materials [1] to store data by reversibly transforming local material volumes between the amorphous and the crystalline state. A focused laser beam (in combination with a spinning disk) is then used to write and erase (recrystallize) amorphous bits in a crystalline surrounding. Besides data storage in optical disks and in electrically controlled random access memories, phase-change materials have recently been used for switching the magnitude of Casimir-Lifshitz forces which can be promising for application in future micro/nanoelectromechanical devices. [2]

Scanning tunneling microscopy and spectroscopy were employed to reveal the evolution of the band gap and the Fermi level as a function of the annealing temperature for phase-change materials. [3] Nonetheless, and despite the extensive use of phase-change materials, little is known about the electrical properties of the amorphous-crystalline interface. This is important for downscaling of electrically controlled non-volatile solid-state memories. [4] In this case, the switching is done by Joule heating and the amorphous to crystalline transition shows a threshold switching event. Storage media with these so called phase-change memory cells have recently been introduced to the market, but still many questions regarding understanding

Based on *Schottky barrier formation at amorphous-crystalline interfaces of GeSb phase-change materials*, H. J. Kroezen, G. Eising, G. ten Brink, G. Palasantzas, B. J. Kooi, and A. Pauza, *Appl. Phys. Lett.* **100**, 094106 (2012)

and optimizing phase-change material properties and performance remain unanswered. When the data cells become smaller and smaller, the currents used to control these data cells during writing, erase, and reading also decrease. Contact resistances become increasingly important upon down scaling. [5] Also, other electrical effects start to play a more dominant role during the switching process, implying that good understanding of all the electrical characteristics of the system is a prerequisite. This also holds for the amorphous-crystalline interface where the change of surface potential, as this interface is crossed, appears to be important.

Indeed, since the amorphous phase is a semiconductor and the crystalline phase in general shows metallic like behavior where free carriers have small mean free paths, [6] the idea naturally emerges that a Schottky barrier might be present at the amorphous-crystalline interface giving rise to a local electric field. So far, this has not been measured directly and it will be the topic of the present chapter using surface scanning potential microscopy (SSPM) and atomic force microscopy (AFM).

6.2 Experimental

6.2.1 Samples

The phase-change thin films used for this chapter consist of a Ge_7Sb_{93} 200 nm thin film on a 1.3 mm polycarbonate substrate. The amorphous phase-change film was partially crystallized by heating them on the hot plate. This yields, depending on the heating procedure, crystalline marks with different sizes/shapes (Fig. 6.1) and thus possibly different crystalline-amorphous interfaces. This is achieved by heating the sample with a relatively slow constant rate up to a certain temperature above the crystallization temperature of ∼130 °C, but below ∼155 °C, and then allow for isothermal crystallization, i.e., crystals nucleate with a certain incubation time (of less than a minute) after the isothermal temperature is reached. Following this procedure, the polycarbonate bottom substrate layer remained relatively stiff, because we remain below its glass transition temperature of ∼155 °C. Above 155 °C, the crystallization process changes radically, as was shown in Fig. 1.1. In any case, the phase-change films studied here have p-type conductivity with Ge acting as a kind of dopant. [7]

Furthermore, three types of samples were investigated, where different heating processes were used to achieve partial crystallization of the films (Fig. 6.1). These are, respectively, referred to as: C1 (Fig. 6.1a; 20 °C min^{-1} up to a maximum temperature of 150 °C), C2 (Fig. 6.1b; 10 °C min^{-1} up to a maximum temperature of 150 °C), and C3 (Fig. 6.1c; 10 °C min^{-1} up to a maximum temperature of 140 °C). Figure 6.1 shows C1 and C2 samples that have large crystalline areas, while sample C3 contains smaller crystallites with triangular-like shape. The

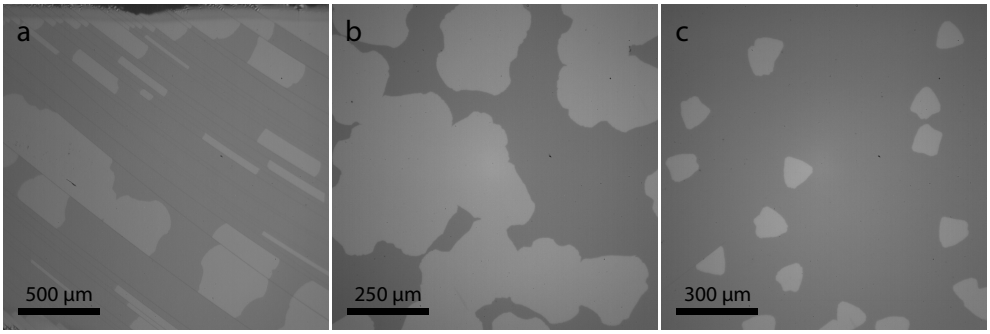

Figure 6.1 | Optical camera images of 200 nm thick partly crystalline Ge_7Sb_{93} films: **a** C1 type, **b** C2 type, and **c** C3 type showing crystallites with a tendency to have a triangular shape.

heating rate in case of Fig. 6.1a has been so high (20 °C min^{-1}) that the difference in thermal expansion between the substrate and the film resulted in parallel cracks in the phase-change film. Despite the cracks, relatively straight amorphous-crystalline interfaces perpendicular to the cracks were formed, which are still very suitable for the present analysis.

6.2.2 Surface measurements

The atomic force microscope (AFM) setup used to perform the SSPM measurements (Figs. 6.2 and 6.3) is a Multimode V (Bruker instruments) with a Nanoscope V controller. The AFM cantilevers/tips were made from Si and were n-type doped with Sb giving a resistivity of ∼0.01–0.025 Ω cm. The natural cantilever frequency was in the range ∼130–250 kHz and the cantilever spring constant was ∼48 N m^{-1} (determined with thermal tuning). Finally, the AFM/SSPM measurements were performed at ambient atmospheric conditions.

6.3 Results and discussion

Figure 6.2 shows an AFM topography and the corresponding SSPM image of an area containing the amorphous-crystalline interface. Figure 6.3 shows the same image types, but now for a relatively small crystal that can be analyzed as a whole embedded in the amorphous surrounding. The average height differences between the crystalline and amorphous areas, as deduced from the images in Figs. 6.2 and 6.3, is 10–15 nm, which is 5 %–7.5 % of the original amorphous layer thickness of 200 nm. This is in good agreement with findings for phase-change materials where upon crystallization the crystalline area shrinks in thickness typically 6 %. [8] On the

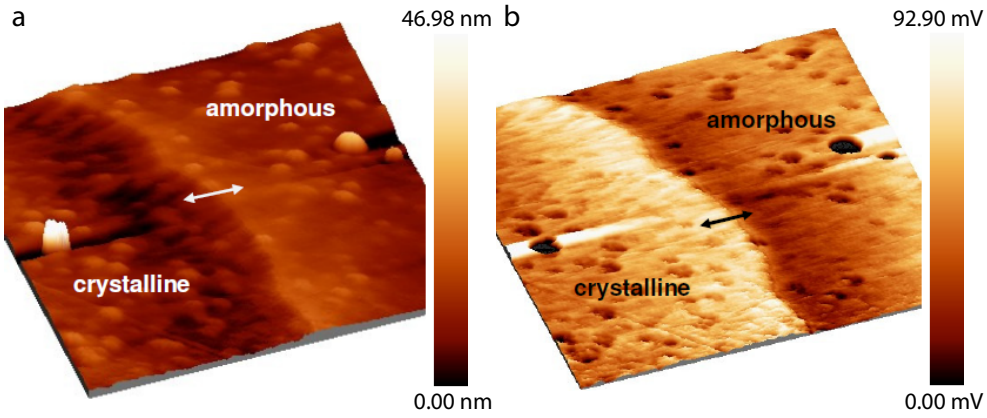

Figure 6.2 | a AFM topography image for sample C2 across a crystalline/amorphous interface. **b** SSPM image. The scan size for both images was 5 µm × 5 µm.

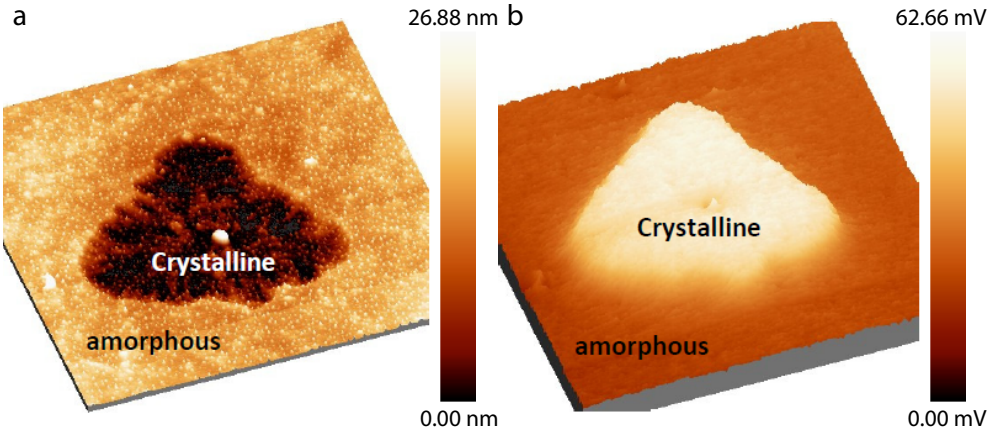

Figure 6.3 | a AFM topography image for sample C3 including a whole crystalline island. **b** SSPM image. The scan size for both images was 15 µm × 15 µm.

other hand, the SSPM image indicates the inverse behavior for the surface potential yielding a higher potential over the crystalline area.

Indeed, as the amorphous to crystalline transition area is crossed, the surface potential increases by $\Delta V \approx 60 \pm 30$ mV for all the samples studied. This potential change ΔV is, however, relatively constant along the same amorphous-crystalline transition area that has a width from topography analysis in the range $W_{\mathrm{TOP}} \approx 300$–$1000$ nm for all the samples studied here (Fig. 6.4). The width of the surface potential change as we cross from the amorphous to crystalline area is slightly smaller of $W \approx 300$–700 nm (Fig. 6.4). Reduction of the resolution in SSPM is

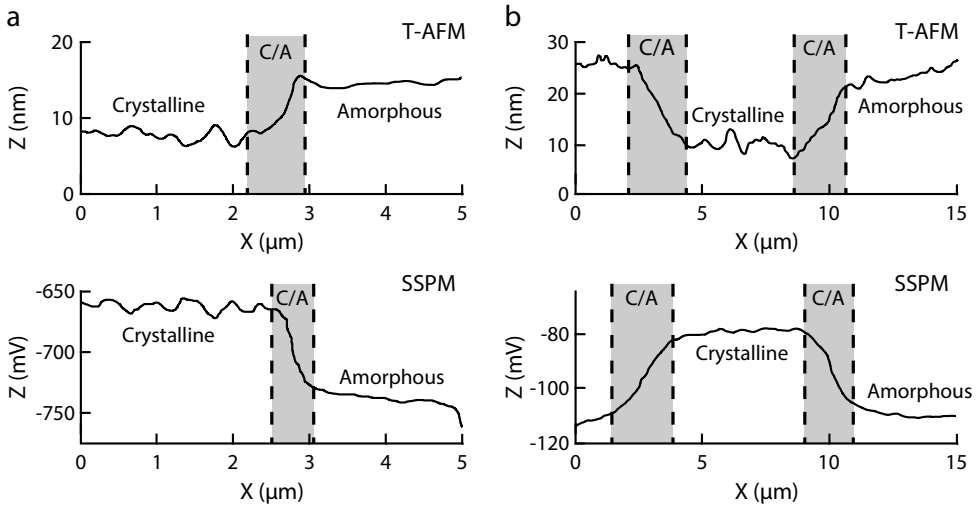

Figure 6.4 | Indicative profiles across the amorphous-crystalline areas in topography (T) AFM and SSPM mode: **a** sample C1 and **b** sample C3. In both cases, the crystalline-amorphous areas and the position of the C/A interface (grayed area) are indicated in a qualitative sense.

due to the transfer function defined by the derivatives of the capacitances between specimen and tip. [9] Nevertheless, as Fig. 6.4 indicates, the amorphous-crystalline transition area is resolved in both AFM topography and SSPM mode. Transmission electron microscopy (TEM) analysis of the amorphous-crystalline interface for GeSb has shown that it is relatively sharp within a few atomic layers. At the profiles, for example of Fig. 6.4, it is located at the bottom of the inclination where the crystalline phase commences.

A simple calculation of the potential barrier assuming that this is of Schottky type is as follows. When the two phases are in contact then the Fermi levels must be aligned for the junction to be in equilibrium otherwise a current would flow. The amorphous phase behaves as a normal p-type semiconductor with the Fermi level lower than that of the crystalline phase, which behaves closely as a metal. Therefore, electrons flow from the crystalline to the amorphous phase. The migration of electrons causes a build-up of charge on both sides of the interface resulting in an electric field and a potential gradient in the semiconducting material. Due to this electric field, the majority carriers (holes in a p-type semiconductor) are pushed away from the interface resulting in an excess negative charge (caused by uncompensated charged acceptors) forming a depletion region of width W (Fig. 6.5). [10]

Furthermore, a square charge density profile $\rho(x) = -qN\theta(W - x)$ (where $\theta(x)$ is the step function) is assumed within the semiconductor occupying the space $x > 0$ with N carriers, of charge q, per unit volume. This is valid when all the acceptors are ionized and the free charges

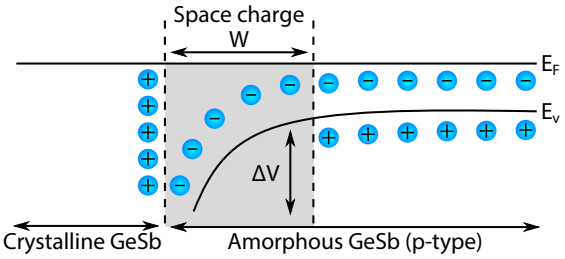

Figure 6.5 | Schematic illustration of the formation of the Schottky barrier.

have moved out of the interface region leaving behind the uncompensated ionized acceptors exactly up to a certain point W (Fig. 6.5). The metal phase is assumed to occupy the $x < 0$ space. Then, the solution of the Poisson equation $d^2V/dx^2 = \rho(x)/\varepsilon$, where ε is the semiconductor permittivity, with the boundary condition $V(x = W) = 0$ gives the potential expression $V(x) = qN(W - x)^2/2\varepsilon$ for $0 \leq x \leq W$ ($V = 0$ for $x \geq W$ and $V = qNW^2/2\varepsilon$ for $x \leq 0$). [9] Thus, at the metal-semiconductor interface, $x = 0$, the Schottky potential height $\Delta V \approx qNW^2/2\varepsilon$ is obtained. [10] Assuming a typical dopant density of $N \approx 10 \times 10^{21}\ \mathrm{m}^{-3}$, [8] $q = 1.6 \times 10^{-19}$ C, interface width $W \approx 400$ nm (obtained from SSPM images), and electric permittivity $\varepsilon \approx 15\varepsilon_0$ ($\varepsilon_0 = 8.86 \times 10^{-12}$), an estimated Schottky barrier height of $\Delta V \approx 96$ mV is obtained. This is relatively close to the measured value of $\Delta V \approx 60 \pm 30$ mV.

Since the amorphous phase is a p-type semiconductor, the Fermi level is localized close to the valence band. As a result, the difference of the work functions, ignoring Fermi level matching and Schottky barrier formation, of the crystalline (φ_C) and amorphous (φ_A) phases would be $\varphi_A - \varphi_C \approx E_g$, where E_g is the band gap of the amorphous phase. Since for the eutectic GeSb phase $E_g \geq 0.4$ eV, [7] the difference in work functions (ignoring Schottky barrier formation) is much larger than the measured surface potential change ΔV ($\varphi_A - \varphi_C >> \Delta V$). However, the Fermi level matching at the C/A interface associated with Schottky barrier formation indicates that ΔV arises mainly from the space charge region.

6.4 Conclusions

The surface potential changes across amorphous-crystalline interfaces in phase-change materials were investigated mainly by SSPM for the GeSb system. Analysis indicated a surface potential for the crystalline phase compared to the amorphous phase which is on average 60 mV higher and always larger than 30 mV. This change in surface potential is associated with the presence of a Schottky barrier at the amorphous/crystalline interface. The latter, if present, has to be taken carefully into account in the electrical characterization of phase-change materials.

References

[1] a) E.R. Meinders, A.V. Mijiritskii, L. van Pieterson, M. Wuttig, *Optical Data Storage - Phase-change media and recording*, vol. 4 of *Philips Research Book Series* (Springer, Berlin, 2006); b) M. Wuttig, N. Yamada, *Nature Materials* **6**, 824 (2007).

[2] G. Torricelli, P. J. van Zwol, O. Shpak, C. Binns, G. Palasantzas, B. J. Kooi, V. B. Svetovoy, M. Wuttig, *Physical Review A* **82**, 010101 (2010).

[3] D. Subramaniam, C. Pauly, M. Liebmann, M. Woda, P. Rausch, P. Merkelbach, M. Wuttig, M. Morgenstern, *Applied Physics Letters* **95**, 103110 (2009).

[4] a) G. Bruns, P. Merkelbach, C. Schlockermann, M. Salinga, M. Wuttig, T. D. Happ, J. B. Philipp, M. Kund, *Applied Physics Letters* **95**, 043108 (2009); b) J. Siegel, A. Schropp, J. Solis, C. N. Afonso, M. Wuttig, *Applied Physics Letters* **84**, 2250 (2004).

[5] D. Roy, M. Zandt, R. A. M. Wolters, *IEEE Electron Device Letters* **31**, 1293 (2010).

[6] a) B. Huang, J. Robertson, *Physical Review B* **81**, 081204 (2010); b) T. Siegrist, P. Jost, H. Volker, M. Woda, P. Merkelbach, C. Schlockermann, M. Wuttig, *Nature Materials* **10**, 202 (2011); c) K. Shportko, S. Kremers, M. Woda, D. Lencer, J. Robertson, M. Wuttig, *Nature Materials* **7**, 653 (2008); d) D. Lencer, M. Salinga, M. Wuttig, *Advanced Materials* **23**, 2030–2058 (2011).

[7] a) D. Shakhvorostov, R. A. Nistor, L. Krusin-Elbaum, G. J. Martyna, D. M. Newns, B. G. Elmegreen, X.-h. Liu, Z. E. Hughes, S. Paul, C. Cabral, S. Raoux, D. B. Shrekenhamer, D. N. Basov, Y. Song, M. H. Müser, *Proceedings of the National Academy of Sciences* **106**, 10907 (2009); b) D. Krebs, Electrical transport and switching in phase change materials, Ph.D. thesis, RWTH Aachen University, Aachen (2010).

[8] a) W. K. Njoroge, H.-W. Woltgens, M. Wuttig, *Journal of Vacuum Science & Technology A: Vacuum, Surfaces, and Films* **20**, 230 (2002); b) J. A. Kalb, C. Y. Wen, F. Spaepen, H. Dieker, M. Wuttig, *Journal of Applied Physics* **98**, 054902 (2005); c) S. Raoux, *Annual Review of Materials Research* **39**, 25 (2009).

[9] a) H. O. Jacobs, P. Leuchtmann, O. J. Homan, A. Stemmer, *Journal of Applied Physics* **84**, 1168 (1998); b) B. Rezek, J. Garrido, M. Stutzmann, C. Nebel, E. Snidero, P. Bergonzo, *Physica Status Solidi A* **193**, 523–528 (2002).

[10] P. Stallinga, *Electrical Characterization of Organic Electronic Materials and Devices* (Wiley, New York, 2009).

Chapter 7

Cluster evolution and critical cluster sizes during nucleation

Abstract. Growth and decay of clusters play an important role in nucleation processes. In this chapter we study these processes at temperatures below the critical temperature T_c for a two dimensional Ising model for both square and triangular lattices using Monte Carlo (MC) simulations and the enumeration of lattice animals. For the lattice animals all unique cluster configurations with their internal bonds were identified up to 25 spins for the triangular lattice and up to 29 spins for the square lattice. From these configurations the critical cluster sizes for nucleation have been determined based on two (thermodynamic) definitions. From the Monte Carlo simulations the critical cluster size is also obtained by studying the decay and growth of inserted most compact clusters of different sizes. A good agreement is found between the results from the MC simulations and one of the definitions of critical size used for the lattice animals at temperatures $T > \sim 0.4T_c$ for the square lattice and $T > \sim 0.2T_c$ for the triangular lattice (for the range of external fields H considered). At low temperatures ($T \approx 0.2T_c$ for the square lattice and $T \approx 0.1T_c$ for the triangular lattice) magic numbers are found in the size distributions during the MC simulations. However, these numbers are not present in the critical cluster sizes based on the MC simulations, as they are present for the lattice animal data. In order to achieve also these magic numbers in the critical cluster sizes based on the MC simulation the temperature has to be reduced further to $T \approx 0.15T_c$ for the square lattice. The observed evolution of magic numbers with temperature rise is rationalized.

7.1 Introduction

Understanding nucleation processes is of great importance, because many natural and technological processes critically depend on nucleation. Most phase transformations proceed via nucleation and growth, and such transitions occur in a wide variety of systems from atomic to astronomic length scales. For instance, stars and solar systems have been developed in the

Based on *Cluster evolution and critical cluster sizes for the square and triangular lattice Ising models using lattice animals and Monte Carlo simulations*,
G. Eising and B.J. Kooi, *Phys. Rev. B* **85**, 214108 (2012)

(early) universe by nucleation and growth. [1] Clouds and rain drops can be associated with nucleation and growth. [2] Nucleation plays also a key role in most materials production, having in general a crucial influence on the final product performance, for instance determining crystal grain sizes and morphologies, second-phase precipitation, recrystallization, etc. [3–5]

A crucial ingredient of nucleation is the presence of an energy barrier that has to be overcome by multiple crossing attempts by certain jump frequencies with certain energies (which often is the thermal energy). The energy barrier is directly associated with (the minimal work required to form) a critical nucleus. For sizes smaller than this critical one, the nucleus has a larger probability to decay than grow and this is only reversed when a nucleus size becomes larger than the critical one. The attempts to cross the energy barrier can in many systems be described as a stepwise release or attachment of monomers to clusters ranging in size from a single monomer to a size that exceeds the critical cluster size having a number of monomers n^*. In the isotropic case, cluster properties are only a function of the number of monomers (spins, atoms, etc.) n they contain. Clusters decay or grow by stepwise release or attachment of a monomer ($n-1$ and $n+1$), i.e. the process is a one-dimensional Markov chain. Although a complete picture of (both steady state and transient) nucleation is far from trivial in this one-dimensional case, [6] the complexity strongly increases when clusters with the same n can have a large variety in shapes and energies, as is already the case within the relatively simple 2D square-lattice Ising model for $n \geq 6$. [7–9] For example, for $n = 19$, 20, and 21, the total number of distinct cluster configurations on the 2D square lattice is over 5.9×10^9, 22×10^9, and 88×10^9, respectively. [9] In principle, all possible transitions with their energies and probabilities between all configurations for such $n-1 \leftrightarrow n \leftrightarrow n+1$ have to be considered from $n = 0$ to n clearly larger than the critical nucleus size n^* in order to arrive at a complete picture of nucleation. Fortunately, the situation simplifies at low temperatures, because cluster energy will prevail over entropy and, thus, for each n, only clusters with the lowest possible energies have to be considered. Then, most configurations can be discarded and the one-dimensional case is again approached. For instance, for $n = 19$, 20, and 21, the number of clusters with the lowest energy (two lowest energies) is 8 (922), 2 (428), and 187 (7835), respectively. [9]

Interesting work has been published recently on the validity of the classical nucleation theory for Ising models. [10] However, still the nucleation process is considered a 1D Markov chain process. Here we show that in principle this one-dimensionality is valid when (i) growth proceeds only along the lowest possible energy path at very low temperatures and (ii) at sufficiently high temperatures the anisotropy in surface energy vanishes.

These examples shows that dynamic Ising models can be relevant and have been popular systems for studying and understanding nucleation (see a non-exhaustive list in Refs. [8–14]). Also, this chapter is dedicated to this field of research by studying for the 2D square and tri-

angular lattice Ising models the critical cluster for nucleation. Two thermodynamic and one kinetic definition have been used to determine the critical cluster size as a function of the external magnetic field H and temperature T below T_c. The thermodynamic definitions are based on lattice animal enumeration up to $n = 29$ for the square lattice and up to $n = 25$ for the triangular lattice. Critical cluster sizes obtained in this way are compared with the ones obtained by the MC simulations based on a technique that we recently developed. [14] Since the MC simulations and the critical cluster size determination (based on the kinetic definition) are computer resource intensive, they were limited to $0.23T_c \leq T \leq 0.5T_c$ and a certain interval of H values. A striking result of the comparison is that critical cluster sizes with magic numbers are present at low temperatures ($T \approx 0.2T_c$ for the square lattice and $T \approx 0.1T_c$ for the triangular lattice) according to both thermodynamic definitions, whereas they are still absent according to the kinetic definition. Yet, the same type of magic numbers are present in the actual size distributions as obtained using the MC simulations at these low temperatures, but they do not show up in the critical cluster size according to the kinetic definition. In order to observe these magic numbers also in the critical nucleus sizes based on the kinetic definition the temperature has to be reduced further ($T \approx 0.15T_c$ for the square lattice). Here we show that the actual critical nucleus involves averaging over neighboring cluster sizes and therefore can be also rationalized in the light of the so-called Transition Path Theory. [15]

The chapter is organized as follows. In section 7.2 the model and numerical methods are explained in detail. Then the results are presented in section 7.3 based on the lattice animal enumerations (7.3.1), based on the MC simulations (7.3.2). The results of these sections 7.3.1 and 7.3.2 are compared in section 7.3.3. Subsequently, the temperature evolution of magic numbers according to Monte Carlo simulations are compared for the square and triangular lattice and finally the correlation of these evolutions with the temperature evolution of the interface tensions for the respective Ising models are shown.

7.2 Model and numerical methods

7.2.1 Ising model

We consider the standard 2D Ising model with the Hamiltonian given by:

$$\mathscr{H} = -J \sum_{nn} \sigma_i \sigma_j - H \sum_i \sigma_i \tag{7.1}$$

with a ferromagnetic coupling constant $J > 0$ between the spins σ having ± 1 value and with an external magnetic field H; nn indicates the summation over all nearest-neighbor pairs.

The energy of a cluster with spins up on a 2D lattice with surrounding spins down in a field H pointing up is defined by the cluster size n and the number of internal nearest-neighbor bonds b:

$$E_n^b = 2JP_n^b - 2nH \tag{7.2}$$

with P_n^b the perimeter of the cluster given by:

$$P_n^b = 4n - 2b \qquad \text{for a square lattice and} \tag{7.3a}$$

$$P_n^b = 6n - 2b \qquad \text{for a triangular lattice.} \tag{7.3b}$$

At low temperatures growth of clusters is completely dominated by the path along minimum cluster energies and thus occurs via the most compact shapes. This means a minimum in E_n^b for each n, corresponding to a maximum in number of bonds b for each n (being the minimal perimeter). The curve of E_n^b versus n in this case is not smooth, because it has an overall classical (Gibbs) outlook plus sharp saw-tooth modulation, see for example Fig. 7.6.

On the square lattice the square $m \times m$ and rectangular $m \times (m + 1)$ shapes, i.e., with {10} facets are the most compact shapes. For given external magnetic field H the critical length m^* is defined by $m^* =$ "floor"$(2J/H)$ with $J(> 0)$ the ferromagnetic coupling constant in the standard Ising Hamiltonian [cf. (7.1)], where the operation "floor" means rounding to the lower nearest integer number. The critical nucleus, as derived by Neves and Schonmann for $T \to 0$, [16] is then the $n^* = m^* \times (m^* + 1)$ rectangle with an extra spin on the longer side. Directly above $T = 0$, also the intermediate $n = m^2 + 1$ clusters can become critical nuclei. [8] The higher the temperature, the more these discrete magic values of n due to the specific low energy configurations become replaced by the continuous spectrum of all integer n values due to configurational entropy.

For the triangular lattice this analysis of most compact shapes and the magic critical cluster sizes has not been presented before and is somewhat more complicated (than for the square lattice), but still can be derived readily based on Eqs. (7.2) and (7.3b). The curve of E_n^b versus n along the lowest energy path shows primary minima in energy for the most compact hexagonal shapes (m(integer) ≥ 1):

$$n_p^- = 3m^2 - 3m + 1, \tag{7.4a}$$

$$b_p^- = 9m^2 - 15m + 6, \tag{7.4b}$$

$$E_n^b = 4J\left[-\frac{9H}{6J}m^2 + \left(6 + \frac{9H}{6J}\right)m - \left(6 + \frac{3H}{6J}\right)\right]. \tag{7.4c}$$

Similarly as for the square lattice, m can be interpreted physically as the facet length, in this case of the hexagon. 'Primary' critical fields H_p^* occur at the maximum in the primary energy

minimum:

$$H_p^* = \frac{4J}{2m-1}. \tag{7.5}$$

In-between two sequential primary critical fields, starting from $H_p^* = \frac{4J}{2m-1}$ in the direction of decreasing H-values (i.e. going from m to $m+1$), first a primary maximum occurs for:

$$n_p^{+1} = 3m^2 - 2m + 1, \tag{7.6a}$$

$$b_p^{+1} = 9m^2 - 12m + 4. \tag{7.6b}$$

Secondary maxima are absent at zero Kelvin, but three secondary maxima do arise for $T > 0$, originating from the secondary critical field at $T = 0$:

$$H_s^* = \frac{6J}{3m}. \tag{7.7}$$

These three secondary maxima in order of decreasing H-values are:

$$n_s^{+2} = 3m^2 - m + 1, \tag{7.8a}$$

$$b_s^{+2} = 9m^2 - 9m + 3, \tag{7.8b}$$

$$n_s^{+3} = 3m^2 + 1, \tag{7.8c}$$

$$b_s^{+3} = 9m^2 - 6m + 2, \tag{7.8d}$$

$$n_s^{+4} = 3m^2 + m + 1, \tag{7.8e}$$

$$b_s^{+4} = 9m^2 - 3m + 1. \tag{7.8f}$$

Then the second primary maximum with:

$$n_p^{+5} = 3m^2 + 2m + 1, \tag{7.9a}$$

$$b_p^{+5} = 9m^2 \tag{7.9b}$$

occurs down to the next $H_p^* = \frac{4J}{2(m+1)-1}$.

Summarizing: In-between two sequential H_p^*, in the direction of decreasing H-values, there are at low temperatures always five domains of constant critical nucleus sizes, where the first $n_p^{+1} = 3m^2 - 2m + 1$ and fifth $n_p^{+5} = 3m^2 + 2m + 1$ correspond to primary domains that at $T = 0$ span the regions defined by $\frac{4J}{2m-1} < H < \frac{6J}{3m}$ and $\frac{6J}{3m} < H < \frac{4J}{2(m+1)-1}$, respectively. The three secondary domains only emerge for $T > 0$ and they originate from $H = \frac{6J}{3m}$ at $T = 0$. One can wonder why there are only five domains and not six, because that would correspond to adding one extra spin to each of the six facets of a perfect hexagon. The reason is that the perfect hexagon has that low (cusp in) energy that adding the first extra spin to one of the six facets of the hexagon will not provide a maximum in energy and will thus not be a critical cluster size at low temperatures.

Based on the energies E_n^b the semi-equilibrium distribution (number density) D_n^b of non-interacting clusters can be derived: [8]

$$D_n^b = w_n^b \exp\left(-\frac{E_n^b}{k_B T}\right), \tag{7.10}$$

where k_B is the Boltzmann constant and w_n^b is the distinct number of configurations possible for given cluster size n and internal bond count b. For the square lattice the values w_n^b can be found in literature up to $n = 21$, [9] for the triangular lattice no relevant literature providing w_n^b values exists. Note that existing literature only provides data on the total number of configurations, polyominoes (polyiamonds, polyhexes) or lattice animals for a given n or provides data on the so-called perimeter polynomials. In the latter case not only the total number of clusters with a certain size n is given, but also how this total number is subdivided over the various possible perimeters. The perimeter is defined as the number of adjacent unoccupied lattice sites which is not equal to the number of bonds to unoccupied nearest neighbor sites needed to calculate the number of internal bonds. Therefore, these known values cannot be used to specify w_n^b and to calculate the number distribution D_n^b that is essential for the study of nucleation (see e.g. Refs. [7] and [8]).

7.2.2 Lattice animals enumeration

The semi-equilibrium distribution of non-interacting clusters as described by Eq. (7.10) is central to the present work and also can be considered fundamental for understanding the nucleation problem of clusters on a lattice (see e.g. Refs. [7] and [8]). The energies E_n^b in Eq. (7.10) can be determined readily, but calculation of the w_n^b values, apart from small cluster sizes n, is very demanding. Based on algorithms by Redner [17] and [18] a parallel algorithm was developed to enumerate all these fixed w_n^b configurations or lattice animals up to a given size $n_{\max}$ including the internal bond counts for each configuration. The enumeration was done recursively, i.e. using a cluster of size n all possible clusters of size $n + 1$ are generated using the cluster of size n as base. The $(n + 1)$-clusters are then used to generate the $(n + 2)$-clusters in a similar way. To prevent generating the same cluster multiple times, information is passed on to the $(n + 1)$-clusters on which lattice sites already have been used by previous n-clusters and are thus forbidden. This is explained in more detail in Ref. [18].

As information on which lattice sites are available for $n + 1$ clusters is only provided by clusters smaller than size $n + 1$ it is possible to split the calculations into multiple branches at size n allowing for perfect parallelization. [18] First, all unique configurations up to size n are generated and stored, together with the information on available and forbidden lattice sites.

Then a number of calculations is started, equal to the number of unique configurations at size n, generating all configurations of size $n+1$ up to $n_{\max}$ with the clusters of size n as starting points.

Using this algorithm the number of configurations w_n^b for the square lattice was calculated up to $n_{\max} = 29$ and for the triangular lattice up to $n_{\max} = 25$. It is noted that the limit $n_{\max}$ is imposed by available computing power, because increasing $n_{\max}$ with one would require four to five times more computing power or time as the total amount of lattice animals increases four to five times. The current enumerations used 40000 hours of CPU time on the Millipede computing cluster at the University of Groningen, which consists of 2832 Opteron 2.6 GHz cores.

7.2.3 Critical cluster sizes

Based on the semi-equilibrium distribution of non-interacting clusters [Eq. (7.10)] two definitions are possible for the determination of the critical cluster size for nucleation at a given temperature and external field. [8] The "microscopic" saddle-point definition identifies a maximum D_n^b among all possible b for a given n. Then a minimum among all n is selected. The second definition is a thermodynamically averaged distribution, i.e. for each n first averaging over all b takes place and then the optimum is selected.

Using the microscopic saddle-point [8] the critical cluster size n^* for nucleation is identified. $D_n(H,T)$ is defined as the maximum of $D_n^b(H,T)$ for a given n for all possible b:

$$D_n(H,T) = \max\left\{ D_n^b(H,T)\,;\, b_{min} \le b \le b_{\max} \right\}. \tag{7.11a}$$

From this definition we find the most favorable amount of bonds for a given n at a certain temperature and field. The critical cluster size $n^*(H,T)$ is then given by n for which $D_n(H,T)$ is minimal.

$$D_{n^*}(H,T) = \min\left\{ D_n(H,T)\,;\, 1 \le n \le n_{\max} \right\}. \tag{7.11b}$$

The critical cluster size according to the thermodynamically averaged definition is derived by summing the contributions of all possible internal bond counts such that an averaged $\langle W \rangle_n (H,T)$ is obtained:

for a triangular lattice:

$$\langle W \rangle_n (H,T) = 12nJ(1 - H/6) - k_B T \ln \sum_{b=b_{min}(n)}^{b=b_{\max}(n)} w_n^b e^{4Jb/k_b T}, \tag{7.12a}$$

and for a square lattice:

$$\langle W\rangle_n(H,T) = 8nJ(1-H/4) - k_BT\ln\sum_{b=b_{min}(n)}^{b=b_{\max}(n)} w_n^b e^{4Jb/k_bT}, \tag{7.12b}$$

and then determining the critical size by selecting the maximum:

$$\langle W\rangle_{n^*}(H,T) = \max\left\{\langle W\rangle_n(H,T)\,;1\le n\le n_{\max}\right\}. \tag{7.12c}$$

It is convenient, without loss of generality, to scale J and the Boltzmann constant k_B to unity and define the temperature with respect to the critical temperature T_c. Calculations were done up to $1.3T_c$, where $T_c = 2/\ln\left(\sqrt{2}+1\right)$ for the square lattice given by Onsager's exact solution [19] and $T_c = 4/\ln(3)$ for the triangular lattice. [20] Note that beyond T_c results can be readily calculated, but they do not have physical meaning and should be treated as formal.

Both definitions for the critical cluster size result in figures with domains of constant critical number n^* (with associated b^*) as function of temperature and external field. For the square lattice this analysis and construction of figures was already done by Ref. [8] up to $n_{\max} = 17$. For the triangular lattice no domain map has been published before as existing literature only provides data on the total number of configurations, polyominoes (polyiamonds, polyhexes) or lattice animals for a given n or provides data on the on the so-called perimeter polynomials, which are not the same as our w_n^b as already explained above.

Note that both definitions of the critical cluster size can never fully agree with the exact results derived for the square lattice by Neves and Schonmann for the critical nuclei when (for fixed H) $T \to 0$. [16] The reason is that in the lattice animal enumeration there is no distinction between the true Neves-Schonmann critical nucleus configurations and configurations that have the same size and energy. To give the most simple example: the $n = 3$ straight cluster and the $n = 3$ L-shaped cluster have the same size and energy in the lattice animal enumeration and are not distinguished, whereas only the latter is a true critical nucleus according to the exact results for $1J < H < 2J$ when $T \to 0$. Nevertheless, as will be demonstrated below the critical nucleus sizes as a function of H for $T \to 0$ based on the two definitions given above still completely agree with the sizes predicted by the exact results of Neves and Schonmann.

7.2.4 Monte Carlo simulations

In order to compare critical cluster sizes derived on the basis of the definitions presented in the previous section, which employ lattice animals enumeration and have in fact a thermodynamic basis, an alternative method employing Monte Carlo simulations is introduced here, which has

a kinetic basis. Cluster growth on triangular and square lattices was studied using Monte-Carlo simulations using the method outlined in Ref. [14]. To study the dynamic cluster evolution processes, the stochastic Glauber dynamics were used, where the spin-flip probabilities are defined by: [21]

$$P\left[s_i \rightarrow -s_i\right] = \frac{\exp\left(-\beta\Delta E\right)}{1 + \exp\left(-\beta\Delta E\right)} \tag{7.13}$$

with $\beta = 1/k_B T$, with k_B the Boltzmann constant, T the temperature and ΔE the energy change due to the spin flip defined, according to the Ising model of Eq. (7.1), by:

$$\Delta E = 2s_i \left(J \sum_{nn} s_j + H \right) \tag{7.14}$$

with *nn* the nearest neighbor sites of site *i*.

Simulations were performed on small square or triangular lattices with appropriate boundary conditions. Initially all spins are pointing downwards. For each Monte Carlo step a site is chosen at random and flipped with the probability given in Eq. (7.13). Time is given in units of Monte Carlo steps per site (MCSS), i.e. in one unit a number of Monte Carlo steps is performed that is equal to the total amount of lattice sites.

To be able to perform relevant MC simulations at low temperatures ($T < 0.5T_c$) and low fields ($H < 0.5$) a cluster with n spins pointing upwards is inserted near the center of a relatively small lattice at $t = 0$ in order to speed up the simulation process. It was shown that inserted clusters of course show stochastic behavior. [14] However, deterministic overall behavior (e.g. the overall fractions of growing and decaying clusters and the whole size distribution after a certain number of MCSS as will be shown below) can be obtained approximately by repeating the simulations several thousand times. [14, 22] The inserted clusters correspond to the most compact shapes, i.e. with the highest number of internal bonds. All the clusters of various size n considered are on the growth path associated with the most compact shapes and thus remain closest to a perfect square shape on the square lattice and a perfect hexagonal shape on the triangular lattice. However, our experiments also show that the results on the critical nuclei are not sensitive to the type of inserted cluster, because results for inserted clusters with two internal bonds less, i.e. two corner sides of the most compact clusters were removed and added to the longer sides of the remaining cluster, showed very similar results.

During the simulation the evolution of the size of the single cluster and its number of internal bonds as function of time is followed. After a certain number of MCSS the amount of clusters and the cluster sizes are determined using the efficient Hoshen-Kopelman algorithm. [23] The cluster size n is defined as the total number of connected spins with a positive orientation. If multiple clusters are present, the size of the largest cluster is taken.

It was shown in Ref. [14] that early on in the simulation the distribution curves after various MCSS are pivoting around a central point that coincides with the final fraction of clusters that will decay and grow. With distribution curve we mean here that all observed cluster sizes after a certain amount of MCSS (when starting at MCSS = 0 from the same initial input cluster) are plotted in ascending (or descending) order. In this way for each input cluster of size n the decay fraction $f_d^n(H,T)$ and growth fraction $f_g^n(H,T) = 1 - f_d^n$ was determined for given temperature T and external field H. The critical cluster size n^* was then defined as the size of the input cluster which shows a decay fraction closest to 0.5:

$$n^*(H,T) = \min\left\{ \left| f_d^n(H,T) - f_g^n(H,T) \right| ; n_{min} \le n \le n_{\max} \right\}. \tag{7.15}$$

Compared to the thermodynamic definitions provided in the previous Section 7.2.3 the present definition of the critical cluster size based on MC simulations can thus be considered a kinetic definition.

7.3 Results

7.3.1 Results of lattice animals enumeration

The results of the enumerations using the algorithm described in section 7.2.2 above are shown in Fig. 7.1 and are listed in Appendix A for both the square and triangular lattice. Cumulative data $\sum_b w_n^b$, available for both square [24] and triangular [25] lattices, were used for verification of the calculated data. Moreover, the present data for the square lattice is identical to the data presented by Ref. [8] going up to $n = 17$ (apart from a mistake in this list at $n = 12$ and $k - n + 1 = 0$; it gives 268852, but must be 268352), and Ref. [9] going up to $n = 21$.

Using the results given in Table 7.1 in Appendix A, a 'phase diagram' of relative temperature T/T_c versus external magnetic field H, showing domains of constant critical cluster size n^* was constructed for the square lattice; see Fig. 7.2a. Effectively this phase diagram was already given in Ref. [8], but we extended it from $n = 17$ up to $n = 29$. In addition we are now showing in one figure both the domains of constant critical bond count b^* using the color coding (see scale at the right-hand axis) and the domains of critical cluster size n^* as indicated by the numbers in the figure. For the triangular lattice the analogous phase diagrams were calculated up to $n = 25$, using the results in Table 7.2 in Appendix A, and are presented with domains of constant n^* and b^* in Fig. 7.2b. Boundaries of domains which are not definite due to limited $n_{\max}$ are shaded.

For $T = 0$ the critical sizes n^* as a function of H in Fig. 7.2b are identical to the sizes calculated using the primary maxima of the energy function, e.g. as described by Eqs. (7.5) and (7.6) in section 7.2.1 for the triangular lattice. For the square lattice the primary maxima

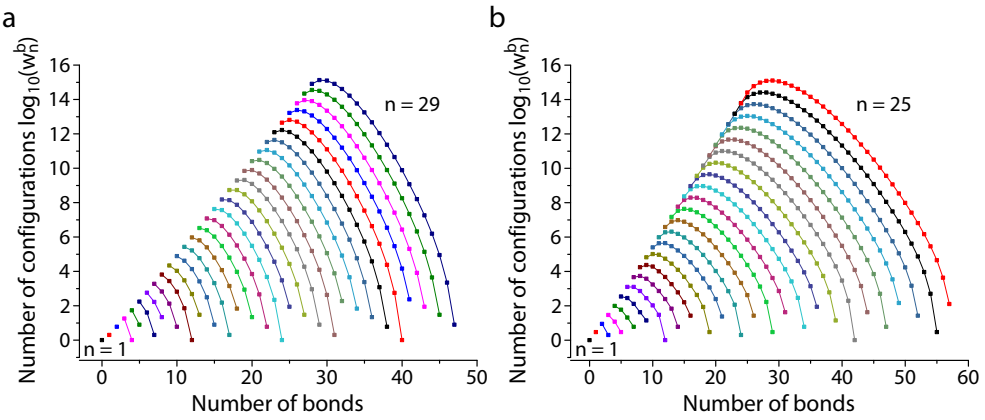

Figure 7.1 | Number of configurations w_n^b as function of the amount of bonds for clusters of given size n for **a** the square lattice and **b** the triangular lattice. Solid lines connect points belonging to the same size n but having a different number of bonds b.

correspond to the $n^* = m(m+1)$ rectangles with an extra spin on the longer side. Also just above $T = 0$ the secondary maxima in Fig. 7.2b for the triangular lattice appear in full agreement with the calculations based on the energy function for the most compact sizes, i.e. Eqs. (7.7) and (7.8) for the triangular lattice. For the square lattice the secondary maxima correspond to $n^* = m^2 + 1$, i.e. square clusters with an extra spin on one side. For higher temperatures (say $T > 0.2T_c$) a more complex pattern appears, showing small domains for which the critical cluster size decreases with increasing temperature (at a certain field H). For the triangular lattice this complex pattern develops already at lower temperatures than for the square lattice.

When comparing the domains of constant n^* with b^* interesting behavior is observed. Let's first consider the situation for the square lattice, because this is more straightforward than for the triangular lattice. For the non-primary and non-secondary domains of constant n^*, i.e. those n^* domains that do not extend down to $T = 0$, two b^* regions are present within each domain of constant n^*: b^* becomes $b^* - 1$ above a certain temperature in the domain. This transition only depends on the temperature since there is no coupling between the external H-field and the number of bonds [cf. Eq. (7.2)]. This is a clear entropic effect, because certain n^* clusters, which have a higher energy (because they contain 1 bond less and thus have a larger perimeter) but have a larger number of configurations w_n^b, become more favorable when the temperature is increased. For the triangular lattice some domains of constant n^* are split (instead of two) in three temperature regions, with b^*, $b^* - 1$ and $b^* - 2$ when going to higher temperature. For instance the domains with $n^* = 4, 5, 9$.

The phase diagram of T/T_c versus H, showing domains of constant critical n^*, calculated

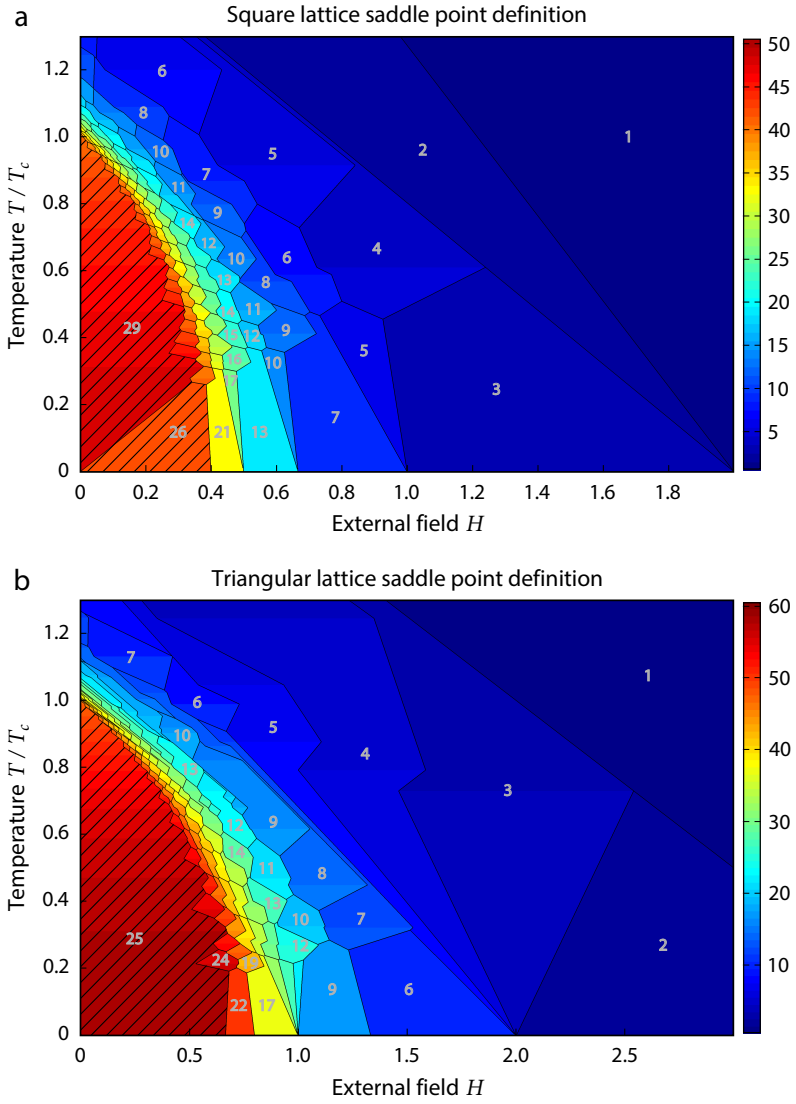

Figure 7.2 | Normalized temperature versus external field H showing domains with constant critical bond count b^* where domains of critical cluster size n^* are separated by black lines for **a** the square lattice and **b** the triangular lattice. The colors depict the most favorable bond counts b^*, where in larger sized domains also values for n^* are given. Note that for the square lattice all domains of constant n^*, that do not extend down to $T = 0$, are split in a b^* lower- and a $b^* - 1$ upper temperature region; for the triangular lattice most domains of constant n^*, certainly those that do not extend down to $T = 0$, are split in two or three temperature regions. This indicates that for those n^* less compact shapes becomes more favorable in the higher temperature region compared to the lower temperature region. The boundaries of the shaded domains are not definite due to limited $n_{\max}$.

using the thermodynamically averaged distribution, are shown in Fig. 7.3a and Fig. 7.3b for the square and triangular lattices, respectively. At low temperatures (say $T < 0.2T_c$) the figures show identical behavior as for the microscopic definition. At higher temperatures the domain boundaries bifurcate, creating new domains with values for the critical size n^* which are in-between the ones of the neighboring domains. This creates a fine pattern with a gradually increasing n^* when going (at a certain temperature) to lower H. This also means that the magic numbers that hold for n^* at low temperatures ($T < 0.2T_c$) become gradually replaced by the whole spectrum of all possible integer n^* at higher temperatures. This replacement occurs for the triangular lattice at clearly lower relative temperatures (T/T_c) than for the square lattice.

For all phase diagrams it is clear that n^* decreases with increasing H. This is an obvious result, because the maximum in (every possible) curve of E_n^b versus n [cf. Eqs.(7.2) and (7.3)] shifts to lower n for higher H. For all phase diagrams it is also clear that n^* decreases with increasing T. The reason for this is that for lower n the total number of possible configurations is also lower. At higher temperatures the configurational entropy term becomes increasingly determining compared to the energy term [cf. Eq. (7.8)]. Therefore, clusters become increasingly critical when they have fewer configurations, i.e. when they are smaller. In Figs 7.2 and 7.3 the results of the calculations are shown for $T \geq T_c$, however the assumption of $J = 1$ is not justified in this regime and the results should be treated as formal.

7.3.2 Results of Monte Carlo simulations

To determine the critical cluster sizes, using the approach employing MC simulations as delineated in section 7.2.2, MC simulations were repeated with different input clusters ranging from a cluster size $n = 5$ to $n = 32$ in their most compact configuration. The simulation was run up to 40 MCSS after which the pivot point in the size distribution could clearly be determined at the intersection of the size distribution curves pertaining to 20 MCSS and 40 MCSS. The decay fraction f_d^n was taken equal to the relative position of the pivot point.

Since the MC simulations and the critical cluster size determination are computer resource intensive, they were limited to regions which showed interesting features in the figures based on the thermodynamic calculations (cf. Figs. 7.2 and 7.3), e.g. where domain boundaries bifurcate when going from lower to higher temperatures. For the triangular lattice the external field H was in-between $0.65J$ and $0.85J$, for the square lattice H was chosen between $0.33J$ and $0.49J$. For both lattices the temperature T ranges between $0.23T_c$ and $0.5T_c$. The MC simulations were repeated 5000 times for each input cluster to obtain enough statistical data for accurately determining the growth and decay fractions.

The resulting $n^*(H, T)$ figures are plotted in Fig. 7.4a for the square lattice and in Fig. 7.5a

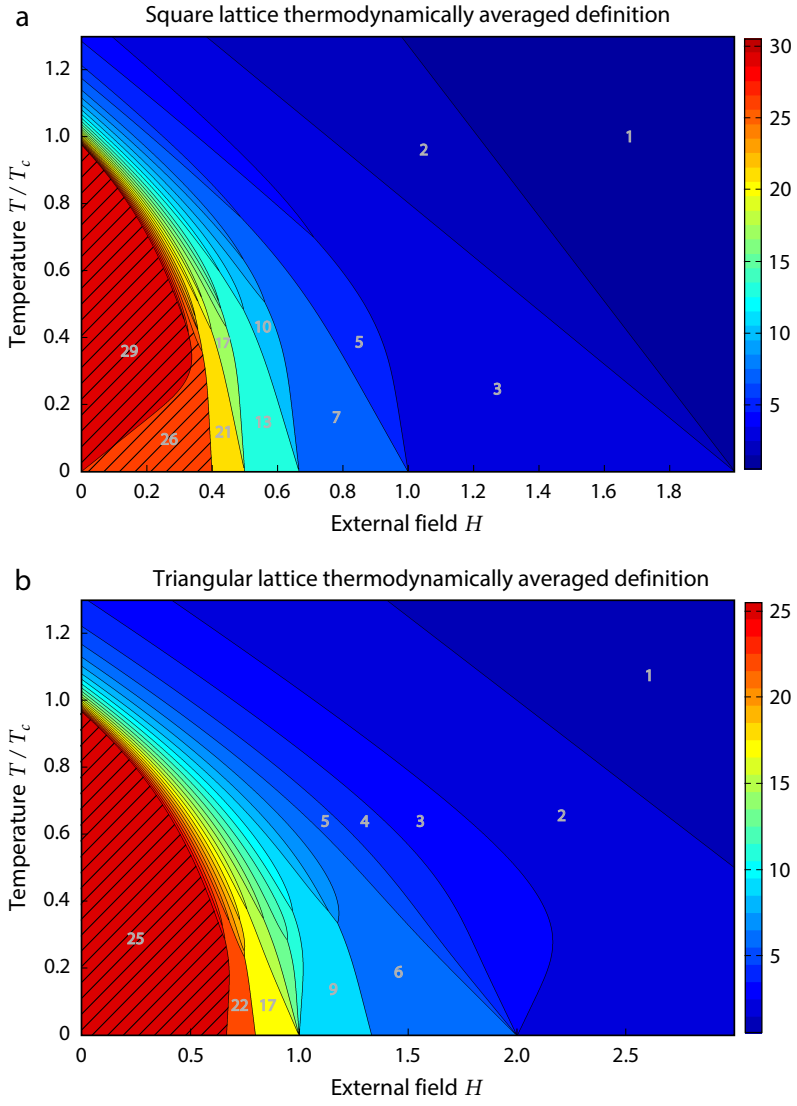

Figure 7.3 | Normalized temperature versus external field H showing domains of constant critical size n^* as defined by the averaged distribution [cf. Eq. (7.12)] for **a** the square lattice and **b** the triangular lattice. **a** Between $T = 0$ and $T = 0.3T_c$ the domains are similar to those in Fig. 7.2a , above $0.3T_c$ a fine pattern appears with increasing n^* when going (at a certain temperature) to lower H. **b** Between $T = 0$ and $T = 0.2T_c$ the domains are similar to those in Fig. 7.2b , above $0.2T_c$ a fine pattern appears with increasing n^* when going (at a certain temperature) to lower H. The boundaries of the shaded domains are not definite due to limited $n_{\max}$.

for the triangular lattice. For both lattices a gradual decrease in critical cluster size is found when increasing temperature and external field; both effects were already explained in section 7.3.1 directly above. The negative slope of the boundaries and bands of the critical sizes become slightly more negative when going to lower H-fields.

In the phase diagram of the triangular lattice all domains with value n^* border domains with value $n^* + 1$ or $n^* - 1$. All changes in critical size are gradual in this window. The domains get slightly narrower when going to lower H. Clearly, no sign of magic numbers can be observed.

On the square lattice the transitions between domains are less gradual, because they involve larger variations in domain width (along the H-axis). Also domain bands are shared by multiple critical n^*, for example $n^* = 19$ and $n^* = 20$ (or 14/15 or 24/25) are both detected critical in the same region. Apart from this, some weak signs of magic numbers are present, because the domains with $n^* = 17$, 21 or 26 are wider.

These results on the critical nuclei turn out not sensitive to the type of inserted cluster, because results for inserted clusters on the square lattice with two internal bonds less, i.e. two corner sides of the most compact clusters were removed and added to the longer sides of the remaining cluster, showed very similar results. With respect to Fig. 7.4a only a shift in H of $-0.03J$ is found for the critical cluster size in case of the inserted less compact clusters. No significant other changes are present in the results for the two types of input clusters and therefore the main conclusions of the present work are not dependent on the type of inserted cluster as long as they are near to the appropriate growth (and decay) paths for this temperature and fields.

7.3.3 Comparing lattice animals enumeration and Monte Carlo simulations

When comparing the domain maps based on the thermodynamic definitions with the ones derived using the MC simulations, it is seen that the best agreement is found with the thermodynamically averaged distribution, see Figs. 7.4 and 7.5. No large discrete regions are observed in the MC simulations, similar as seen for the saddle-point definition. Instead there are bands of constant critical size with an increasing negative slope for higher H, like in the case of the thermodynamically averaged results. This holds for both the triangular and square lattices. This is an interesting observation, because the starting clusters for the MC simulations are the most compact shapes (closest to perfect square or hexagonal shapes) and therefore these clusters start directly on the lowest energy path associated with the saddle-point definition. Apparently during the MC simulations an averaging over configurations is taking place that appears to go away from the lowest energy path and, as we will show below, the averaging is even going beyond the one of the thermodynamically averaged result.

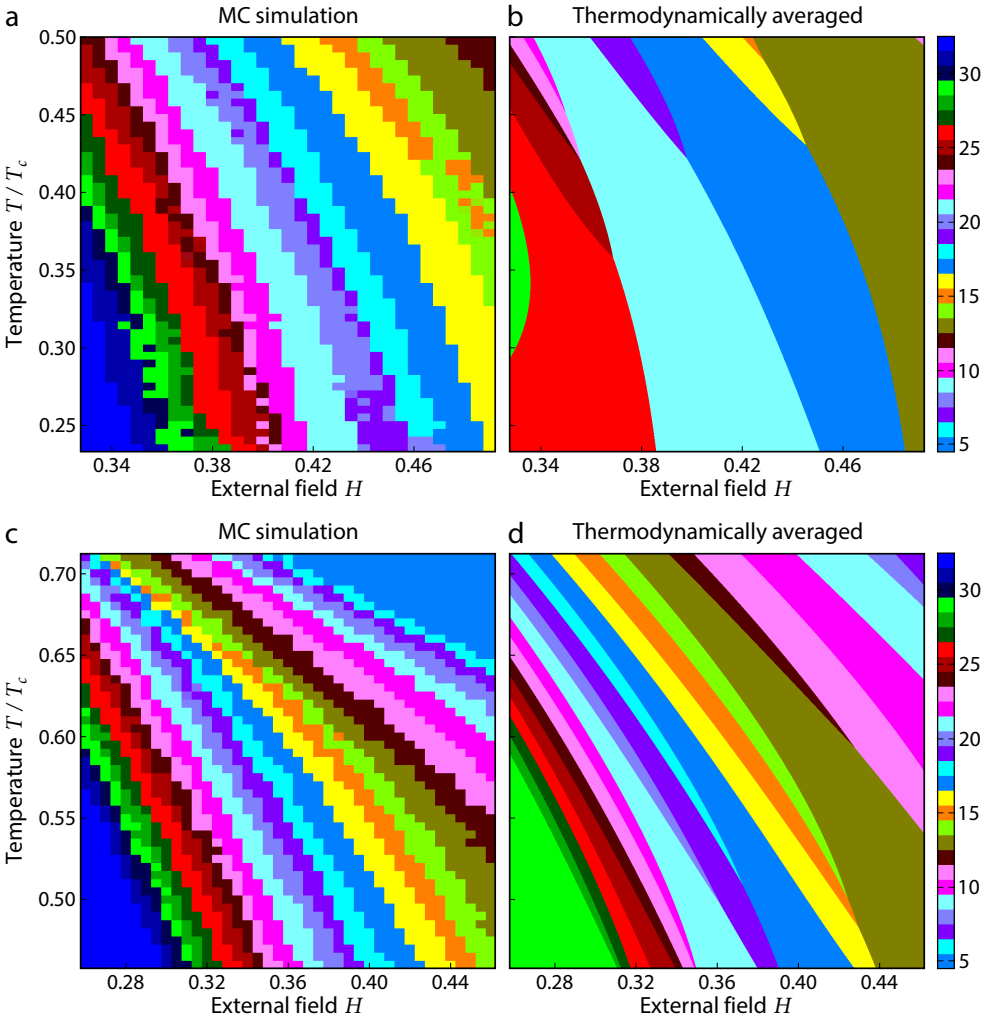

Figure 7.4 | Domains for critical size n^* on a square lattice. The color indicates the critical size n^*. **a** and **b** Temperature T between $0.23T_c$ and $0.50T_c$ and external field H between $0.33J$ and $0.49J$. **c** and **d** Temperature T between $0.46T_c$ and $0.71T_c$ and external field H between $0.26J$ and $0.46J$. **a** and **c** For each point 5000 clusters in their most compact configurations were used for the MC simulations for each n. For each simulation the decay fraction was determined after 40 MCSS and was used to determine the critical cluster size n^* [cf. Eq. (7.15)]. **b** and **d** Critical cluster size as determined by the thermodynamically averaged definition [cf. Eq. (7.12b)]. The boundaries of the shaded domains are not definite due to limited $n_{\max}$.

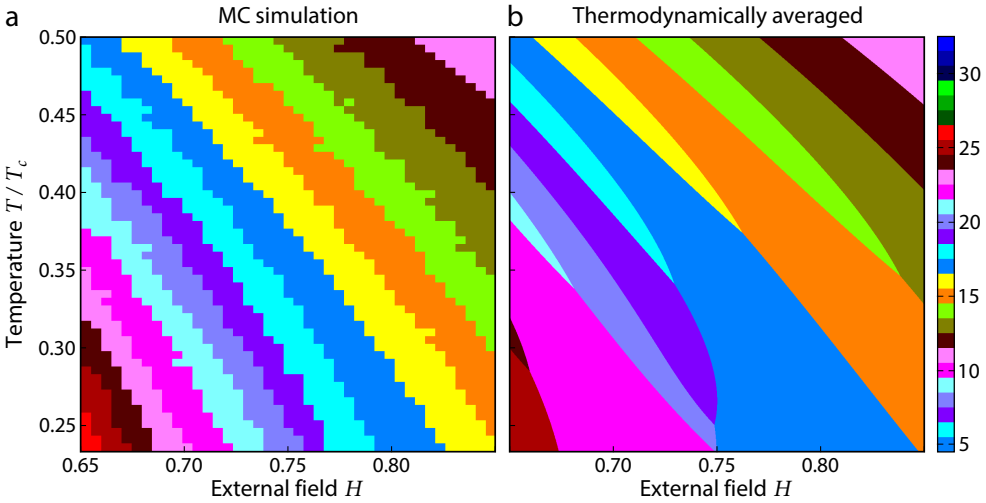

Figure 7.5 | Domains for critical size n^* on a triangular lattice for T between $0.23T_c$ and $0.5T_c$ and H between $0.65J$ and $0.85J$. The color indicates the critical size n^*. **a** Results from the Monte Carlo simulations. For each point 5000 clusters in their most compact configurations were used for the MC simulations for each n. For each simulation the decay fraction was determined after 40 MCSS and was used to determine the critical cluster size n^* [cf. Eq. (7.15)]. **b** Results from the averaged definition as calculated using Eq. (7.12a). The boundaries of the shaded domains are not definite due to limited $n_{\max}$.

For the square lattice not all critical sizes are present in the MC simulations in similar quantities. For example, input clusters of size 20 and 25 are less present than clusters of size 21 and 26. This is supported by the thermodynamically determined critical sizes where below $0.36T_c$ no critical size of 25 is found. A big difference is however that even at a low temperature of $0.25T_c$ all possible critical sizes (in the interval 12–32) are still found in the MC simulations, whereas in the thermodynamic definition only the magic numbers 13, 17, 21 and 26 are present.

By increasing the temperature T to the range of $0.46T_c$ to $0.71T_c$ and decreasing the external field H to the range of 0.26 to 0.46 the thermodynamically averaged definition shows a gradual change from large clusters to small ones with all possible n^* present, see Figs. 7.4c and 7.4d. MC simulations on a square lattice performed in this range show excellent agreement for clusters larger than $n^* = 15$ for the entire range, while for smaller cluster sizes the best agreement is found for $T < 0.6T_c$ (and $T > 0.45T_c$).

For the triangular lattice we see an excellent agreement between the MC simulations and the results from the averaged definition for temperatures above $0.4T_c$, see Fig. 7.5. Below this temperature the domains according to the thermodynamically averaged definition gradually

reduce to only the ones of the magic numbers described by Eqs. (7.6)–(7.9), whereas the MC simulations still shows the presence of all possible n^*.

Apparently for both the square and triangular lattices at low temperatures ($< \sim 0.30 T_c$ for the range of H-values presented) the MC simulations still provide the complete spectrum of all possible n^* and are not following the results for the thermodynamically averaged definition of the critical cluster size. The reason for this is that with the MC definition of the critical cluster size, i.e. the most compact n-size cluster that has a probability to grow (or decay) most closely to 50%, not only averaging over b for a certain n takes place, but that also a certain weighted averaging over directly associated neighboring n takes place. In this respect it is quite obvious that the occurrence of magic numbers for the critical cluster size is strongly suppressed according to the kinetic MC definition. In this respect the MC simulations provide results that show some interesting features also predicted by the Transition Path Theory. [15]

7.3.4 Temperature evolution of magic numbers

The MC simulations indicate that magic numbers are not present at low temperatures such as $T/T_c = 0.25$, at least not in the sequence of critical nuclei as a function of magnetic field H. Moreover, the phase diagrams shown above in Figs. 7.2 and 7.3 indicate that the disappearance of magic numbers with temperature rise occurs at lower temperatures for the triangular lattice than for the square one. To shed more light on these issues Fig. 7.7 presents cluster-size distributions obtained by MC simulations at relatively low temperatures for the square and triangular lattice, where on both lattices the starting cluster was a $n = 30$ cluster in (one of) its most compact shape. The statistic distribution of cluster sizes obtained for 10000 initially identical clusters is shown after a sufficiently large number of MCSS, which allows some local equilibration of cluster sizes. Actually the cluster size distribution can be considered the product of a Gaussian distribution with the semi-equilibrium distribution described by Eq. (7.10). [14] For fixed H and T, Eq. (7.10) is fixed, but the Gaussian distribution evolves with MCSS from nearly a delta function to a broad distribution.

Figure 7.6 shows, for both the triangular and square lattices, the cluster energy E_n^b normalized by the critical temperature T_c as a function of cluster size n for the most compact clusters (i.e. largest number of bonds b) and thus depicts the lowest energy path for growing (and decaying) clusters. The energy curves in Fig. 7.6 clearly exhibit an overall classical (Gibbs) outlook plus a sharp saw-tooth modulation. The values for H were chosen such that the overall classical outlook of the energy curves for the triangular and square lattice obtains the same shape, with a maximum near $n = 30$, i.e. $H = 0.37$ for the square lattice and $H = 0.642$ for the triangular lattice. Normalization by T_c allows the energy curves to also obtain comparable absolute val-

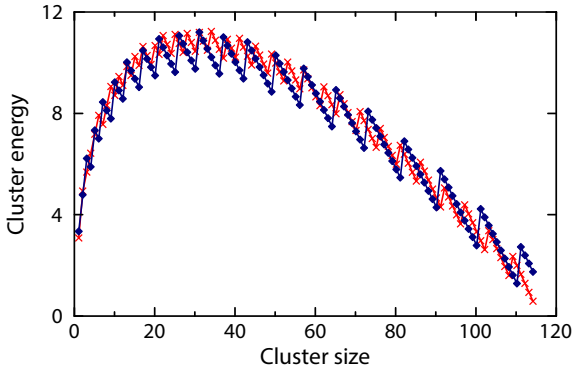

Figure 7.6 | Cluster energy E_n^b normalized by T_c as a function of cluster size n for both square (diamonds) and triangular (crosses) lattice for the most compact clusters. The external field H was chosen such that the energy curves for the triangular and square lattice obtain the same overall shape.

ues. In this way we create comparable energy landscapes for cluster evolution on the triangular and square lattice.

Figure 7.7a shows results for $T = 0.454$K, i.e. the same absolute temperature for the square and triangular lattice (which is $T = 0.2T_c$ for the square and $T = 0.1247T_c$ for the triangular lattice). The results for the square lattice hold after 200 MCSS and for the triangular lattice after 300 MCSS, but the conclusions we will draw below are not sensitive to the value of the MCSS. In both cluster size distributions clear signs of the expected magic numbers for maxima and minima are present. These magic numbers vanish at approximately $0.2T_c$ for the triangular lattice and $0.4T_c$ for the square lattice. Despite that T/T_c is clearly lower for the triangular lattice, the (amplitude of the) modulation in the size distribution, i.e. the ratio between neighboring maxima and minima, is clearly smaller in case of the triangular lattice than for the square lattice. The main reason for this is that, for the same absolute temperature, the value for the saw-tooth modulation (barrier heights) in the energy curve E_n^b versus n is lower for the triangular than for the one of square lattice case [cf. Fig. 7.6].

Therefore, it is interesting to lower the temperature for the triangular lattice such that the same value for the saw-tooth modulation holds for the (lowest energy path in the) E_n^b versus n curves of the square and triangular lattices. To do so, the temperature is reduced from $T = 0.1247T_c$ (the case shown in Fig. 7.7a) to $T = 0.1038T_c$ and the result (after 400 MCSS) is shown in Fig. 7.7b. The size distribution holding for the square lattice is the same in Figs. 7.7a and 7.7b. Lowering the temperature of the triangular lattice has the clear effect that the modulation and magic numbers (which were weaker) are now much stronger present in the size distribution for the triangular lattice than for the square one. Apparently for the same value of

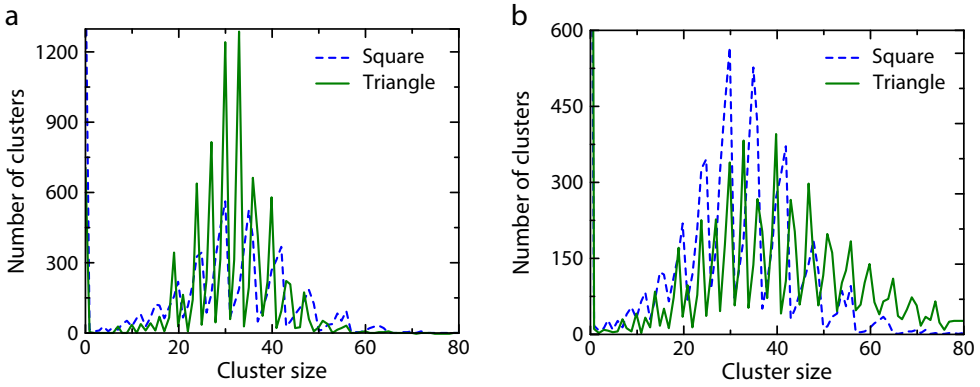

Figure 7.7 | a Cluster size distribution at $T = 0.454$ K after 200 MCSS (square lattice) and 300 MCSS (triangular lattice) after insertion of a most compact $n = 30$ cluster. For both lattices the occurrence of magic numbers is clearly visible, but the modulation is clearly stronger for the square lattice. **b** Cluster size distribution for the triangular lattice at $T = 0.377$ K after 400 MCSS. For the square lattice the distribution is identical as in **b**, i.e. holds for $T = 0.454$ K after 200 MCSS. This difference in temperature for both lattices ensures that the height in the saw tooth modulation of the energy curve shown in 7.6 is the same for both cases. Now the magic numbers are more prominent for the triangular than for the square lattice.

the saw-tooth modulation (barrier heights) in the energy path, the lower absolute temperature for the triangular lattice determines that the modulation in the size distribution and thus the magic numbers become more prominent. This can be understood, because the lower the temperatures the more growth proceeds via the lowest energy path. At higher temperatures growth also occurs via less favorable (higher energy) cluster configurations, which obscure the magic numbers (and thus dampens the modulation) in the size distribution.

Despite that magic numbers are *not* present according to the kinetic MC definition of critical cluster sizes (see previous section), the present results show that they are actually present in the size distribution itself for the square lattice below about $0.4T_c$ (for $\sim 0.3J < H < \sim 0.5J$) and for the triangular lattice below $\sim 0.2T_c$ (for $\sim 0.5J < H < \sim 0.9J$).

The question now remains when magic numbers will become present according to the kinetic MC definition of critical cluster sizes. To test this, additional MC simulations were performed for the square lattice for $T = 0.15T_c$ for H between $0.1J$ and $0.5J$ with 1000 MCSS and showed that the critical clusters as found from theory [$m^*(m^* + 1) + 1$ and $m^2 + 1$] are clearly present. Cluster sizes in between these critical cluster sizes were also present but only in thin lines between the critical domains. Therefore we expect that the critical cluster sizes according to our kinetic definition will also converge to, i.e. reproduce the sizes with magic numbers of the exact results of Neves-Schonmann for $T \to 0$.

The present results show some interesting agreement with predictions of Transition Path Theory. [15] TPT shows for example that at elevated temperatures a critical cluster size for nucleation is not present, but there is a transition path region (which includes many different clusters also with different sizes). Therefore, from TPT at higher T a 'critical cluster size for nucleation' in the Ising model can be absent, but when $T \to 0$ the transition path region converge exactly to the critical nuclei according to Neves-Schonmann. [16] These predictions agree very well with the results of our MC simulations described and shown above. It is particularly relevant to note that at higher temperatures the averaging over neighboring cluster sizes indicate that there in principle is not a critical cluster size, but only a transition path region. The results also show that the thermodynamic definitions have limited meaning. The saddle-point definition is only relevant for $T \to 0$.

7.3.5 Reduced interface tension according to lattice animals

An interesting correlation can be made between the disappearance of magic numbers with temperature rise in the size distributions and the disappearance of the difference in interface tension for the lowest and highest interface energy direction of the Ising system considered. For the square lattice the lowest interface tension holds for the direction parallel to one of the two principal lattice vectors (i.e. parallel to a {10} boundary): [26]

$$\sigma_{//} = 2 + T \ln\left(\tanh\left(\frac{1}{T}\right)\right). \tag{7.16a}$$

The highest interface tension holds for the two directions making 45° with the principal lattice vectors (i.e. parallel to a {11} boundary): [26]

$$\sigma_{\text{diag}} = T\sqrt{2}\sinh\left(\frac{2}{T}\right). \tag{7.16b}$$

These two interface tensions are shown as a function of reduced temperature (i.e. with $T_c = 2/\ln\left(\sqrt{2}+1\right)$) in Fig. 7.8a. For temperatures above $0.6T_c$, about the same interface energies hold for $\sigma_{//}$ and σ_{diag}. In the range from $0.6T_c$ down to $0.3T_c$ the difference between the highest and lowest interface energy is still modest, but this difference rapidly increases when going from $0.3T_c$ down to $0T_c$.

For the triangular lattice the lowest interfacial tension holds for the direction parallel to one of the three principal lattice vectors (i.e. parallel to the $\{10\bar{1}\}$ boundary): [27]

$$\sigma_{\{10\bar{1}\}} = 2T\,\text{arcCosh}\left(\sqrt{\frac{2X+3}{4}} - \frac{1}{2}\right). \tag{7.17a}$$

The highest interfacial tension holds for the three directions making 30° with the principle lattice vectors (i.e. parallel to the $\{11\bar{2}\}$ boundary): [27]

$$\sigma_{\{11\bar{2}\}} = \frac{2T}{\sqrt{3}} \operatorname{arcCosh}\left(\frac{X-1}{2}\right), \tag{7.17b}$$

With X specified as:

$$X = \frac{2y}{(1-y)^2} + \frac{(1-y)^2}{2y} + 1, \tag{7.17c}$$

With y specified as:

$$y = \tanh\left(J/T\right). \tag{7.17d}$$

These two interface tensions are shown as a function of reduced temperature (i.e. with $T_c = 4/\ln(3)$) in Fig. 7.8b. For temperatures above $0.3T_c$, about the same interface energies hold for $\sigma_{\{10\bar{1}\}}$ and $\sigma_{\{11\bar{2}\}}$. In the range from $0.3T_c$ down to $0.15T_c$ the difference between the highest and lowest interface energy is still modest, but this difference rapidly increases when going from $0.15T_c$ down to $0T_c$.

Interestingly, the difference in highest and lowest interface tension lattice reduces to a value of about 0.12 at $0.4T_c$ for the square lattice and at $0.2T_c$ for the triangular lattice. Apparently at these temperatures the experienced anisotropy in interface tension is that low that also in the MC simulations the magic numbers disappear. The evolution and the disappearance of the difference in interface tension occur at two times higher T/T_c values for the square than for the triangular lattice. The same holds for the evolution and disappearance of magic cluster sizes with the MC simulations. Therefore, an interesting correlation exists between the disappearance of anisotropy in interface tension with temperature rise holding for the Ising systems considered and the disappearance of magic numbers with temperature rise based on MC simulations of these Ising systems.

Partly the comparison between the interfacial tension and the MC simulations is not appropriate, because with the MC simulations we consider (too) small cluster sizes. This can be readily deduced from the following analysis. Using the results of the lattice animal enumeration we are able to derive an effective interface tension associated with a certain cluster size, which is defined for the square lattice as: [26]

$$\sigma_n^{s,\,eff} = \frac{-T\ln\left(\sum_{b_{\min}}^{b_{\max}} D_n^b\right)}{2\sqrt{\pi n}}, \tag{7.18}$$

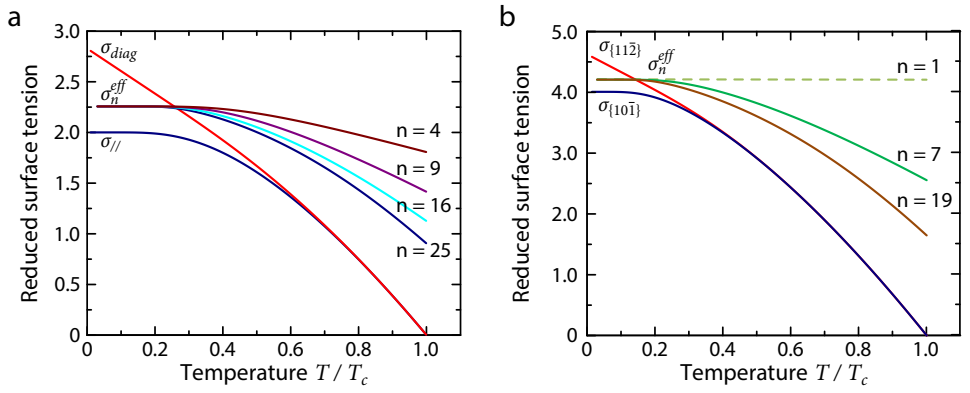

Figure 7.8 | Lowest and highest interface tension as function of normalized temperature compared with the effective interface tension derived from the results of the lattice-animals enumeration for the most compact square and hexagonal clusters. **a** For the square lattice the lowest interface tension and the highest interface tension hold for the directions parallel and making a 45° angle with the principal lattice vectors: $\sigma_{//}$ and σ_{diag}. Above $0.6T_c$ about the same interface energy is found for $\sigma_{//}$ and σ_{diag}, below $0.6T_c$ a modest difference is seen, which is rapidly increasing below $0.3T_c$. **b** For the triangular lattice the lowest interface tension and the highest interface tension hold for the direction parallel and making a 30° angle with the principal lattice vectors: $\sigma_{\{10\bar{1}\}}$ and $\sigma_{\{11\bar{2}\}}$. Above $0.3T_c$ about the same interface energy is found for $\sigma_{\{10\bar{1}\}}$ and $\sigma_{\{11\bar{2}\}}$, below $0.3T_c$ a modest difference is seen, which is rapidly increasing below $0.15T_c$.

and for the triangular lattice as:

$$\sigma_n^{t,\,eff} = \frac{-T \ln\left(\sum_{b_{\min}}^{b_{\max}} D_n^b\right)}{\sqrt{\sqrt{3}\pi(4n-1)/2}}, \tag{7.19}$$

where D_n^b is given by Eq. (7.10) for $H = 0$. This effectively means that the cluster area (independent of shape) is mapped onto a circle and the circumference of this circle is taken as the interface length. The size dependent effective interface tensions are shown for most compact shapes in Fig. 7.8a and 7.8b for the square and triangular lattices, respectively. Clearly, it can be observed that the effective interface tensions of these small clusters largely deviate from the ones of long interfaces according to the Ising models considered. Since hexagons have shapes better approaching the circular circumference than squares, it might be expected that in the high temperature regime, where there is no anisotropy in interface tension for long interfaces, the effective interface tension with increasing cluster size more rapidly converges to the one of long interfaces. The present results do not show this more rapid convergence as a function of cluster size n, but when normalized to the facet length of the hexagon and square (so that

hexagons with $n = 7$ and 19 are compared to squares with $n = 4$ and 9, respectively) indeed this more rapid convergence occurs.

7.4 Summary and conclusions

In the present work we have studied the growth and decay of clusters at temperatures below T_c for a two dimensional Ising model on square and triangular lattices. This was done by enumerating all unique lattice configurations up to $n = 25$ for the triangular lattice and up to $n = 29$ for the square lattice. From these enumerations the critical cluster sizes as function of temperature and external field have been calculated for both lattices using two different thermodynamic definitions. In addition, Monte Carlo simulations were performed to calculate the critical cluster size using a kinetic definition. By inserting a (most) compact cluster at the start of the simulation on a relatively small lattice, the simulation was speeded up at low temperatures.

The obtained MC results are in good agreement with the results obtained from the lattice-animals enumeration based on the thermodynamic 'averaged' definition. In contrast, the thermodynamic 'saddle-point' definition provides results which strongly deviate from the other two definitions at higher temperatures ($T > \sim 0.4T_c$ for $\sim 0.3J < H < \sim 0.5J$ for the square lattice and $T > \sim 0.2T_c$ for $\sim 0.5J < H < \sim 0.9J$ for the triangular lattice). Even when we start with the inserted most compact cluster exactly in the saddle-point of the energy landscape, still the MC simulations will create a critical cluster size based on averaging not only over the various highest bond numbers for this size, but also influenced by growth and decay of neighboring cluster sizes. These results show interesting correspondence with predictions of Transition Path Theory. The dominance of a transition path region is also the principle reason that magic numbers found at low temperatures in the critical cluster size mapping determined from the lattice-animals enumeration did not appear in the results from the MC simulations. However, the magic numbers are still present at these low temperatures when looking at the cluster size distributions themselves during the MC simulation. Magic numbers in the size distribution are absent for $T > \sim 0.4T_c$ for the square lattice and $T > \sim 0.2T_c$ for the triangular lattice. This disappearance of the magic numbers with temperature rise according to the MC simulations appears to correlate well with the disappearance of anisotropy in interface tension for both the triangular and square lattice Ising models.

Appendix A Results of lattice animal enumerations

To reduce the size of this appendix, only the last four columns of the enumeration results for both square (i.e. $n = 26$–29) and triangular (i.e. $n = 22$–25) lattices are displayed. The complete tables with results of the enumerations can be obtained from http://prb.aps.org/epaps/PRB/v85/i21/e214108/Supplementary_information.pdf

Table 7.1 | Numbers w_n^b for lattice animals of size n with b nearest-neighbor bonds on a square lattice

$b-n+1$	$n=26$	$n=27$	$n=28$	$n=29$
0	16229462702152	59347661054364	217310732774774	796703824808133
1	24189042735960	92182297780388	351188857252945	1337559410177992
2	20069340693032	79445751162174	313931473684234	1238483979520028
3	11597020580256	47725780350640	195729688775506	800180322864548
4	5206305915854	22277974479762	94833467125572	401780150376616
5	1907128463082	8497520990660	37589435038468	165195027753972
6	590692982046	2744186080582	12628435807352	57620841061986
7	157649849696	765476680236	3671711955694	17421230022108
8	36829344698	187422193706	939128828434	4641894687940
9	7573377658	40581745976	213182013614	1100786553816
10	1376399286	7815893062	43249505720	234139368404
11	219358602	1334350332	7839604886	44760447220
12	30221878	200555450	1266040556	7688145478
13	3436112	25853212	179481116	1176550436
14	292150	2715418	21706048	157863938
15	14408	203956	2089582	17843312
16	238	8238	138032	1572217
17		88	4410	89720
18			30	2244
19				8
Sum	79992676367108	313224032098244	1228088671826973	4820975409710116

Table 7.2 | Numbers w_n^b for lattice animals of size n with b nearest-neighbor bonds on a triangular lattice

$b-n+1$	$n=22$	$n=23$	$n=24$	$n=25$
0	904559526029	3633045705543	14618866104849	58925096656511
1	3381680573145	14245879371702	59994271844640	252587197669380
2	6935395193619	30536428025994	134149981674201	588136415285907
3	9882512145349	45491545097088	208502270964357	951883848747450
4	10946275371915	52639206348039	251541102048070	1195131553155843
5	10029051824175	50323384357908	250467164237622	1237407269795130
6	7951429502780	41540918651313	214945130085942	1102419675592266
7	5616587038428	30493548920454	163742542311590	870415630787376
8	3604100678331	20309871329400	113031582891882	621926951369688
9	2125074406429	12426594377682	71643698564961	407769357680848
10	1162894886292	7054620513255	42120504760647	247887899346549
11	595319641932	3745901651316	23155725486606	140868293836188
12	286949641752	1872872536719	11985082924146	75351132792440
13	130627824807	885143641404	5866594347098	38126042283798
14	56389557147	396966215310	2726382831960	18321328706652
15	23152543856	169477230348	1206921456984	8390106044744
16	9060408456	69067326666	510450312074	3672888359445
17	3376811733	26876822412	206507952681	1539749615394
18	1201199147	10003234443	80041352667	619195388568
19	407325135	3562397538	29750219757	239163111534
20	131388126	1213474803	10611378024	88825796556
21	40050371	393762516	3624898689	31702007762
22	11542896	121707717	1185595080	10872940908
23	3095724	35638878	370426029	3580047858
24	753821	9774798	109999506	1129300090
25	163743	2479080	30800680	339516990
26	29049	568761	8081229	97023045
27	3424	111990	1933998	26091412
28	147	17115	411402	6493404
29		1458	73266	1462794
30		27	9138	288661
31			496	44646
32			3	4338
33				128
Sum	63646233127758	315876691291677	1570540515980274	7821755377244303

References

[1] a) H. J. D. Vega, I. M. Khalatnikov, N. G. Sànchez, eds., *Phase Transitions in the Early Universe: Theory and Observations*, vol. 40 of *NATO Science Series* (Springer Netherlands, Dordrecht, The Netherlands, 2001); b) A. Patzer, A. Gauger, E. Sedlmayr, *Astronomy & Astrophysics* **337**, 847 (1998); c) T. Nozawa, T. Kozasa, H. Umeda, K. Maeda, K. Nomoto, *The Astrophysical Journal* **598**, 785 (2003); d) I. Bombaci, D. Logoteta, C. Providência, I. Vidaña, *Astronomy & Astrophysics* **528**, A71 (2011).

[2] R. McGraw, Y. Liu, *Physical Review Letters* **90**, 018501 (2003).

[3] a) J. W. Christian, *The theory of transformations in metals and alloys: an advanced textbook in physical metallurgy* (Pergamon Press, Oxford, England, 1965); b) D. A. Porter, K. E. Easterling, M. Y. Sherif, *Phase Transformations in Metals and Alloys* (CRC Press, Boca Raton, FL, 2009).

[4] J. Schmelzer, ed., *Nucleaton Theory and Applications* (Wiley, New York, 2005).

[5] B.-S. Lee, G. W. Burr, R. M. Shelby, S. Raoux, C. T. Rettner, S. N. Bogle, K. Darmawikarta, S. G. Bishop, J. R. Abelson, *Science* **326**, 980 (2009).

[6] K. F. Kelton, A. L. Greer, C. V. Thompson, *The Journal of Chemical Physics* **79**, 6261 (1983).

[7] V. A. Shneidman, *Journal of Statistical Physics* **112**, 293 (2003).

[8] V. A. Shneidman, G. M. Nita, *The Journal of Chemical Physics* **121**, 11232 (2004).

[9] S. Frank, D. E. Roberts, P. A. Rikvold, *The Journal of Chemical Physics* **122**, 064705 (2005).

[10] S. Ryu, W. Cai, *Physical Review E* **81**, 030601 (2010).

[11] K. Binder, H. Müller-Krumbhaar, *Physical Review B* **9**, 2328 (1974).

[12] a) P. A. Rikvold, H. Tomita, S. Miyashita, S. W. Sides, *Physical Review E* **49**, 5080 (1994); b) V. A. Shneidman, K. A. Jackson, K. M. Beatty, *Physical Review B* **59**, 3579 (1999).

[13] a) A. Bovier, F. Manzo, *Journal of Statistical Physics* **107**, 757 (2002); b) K. Park, P. A. Rikvold, G. M. Buendía, M. A. Novotny, *Physical Review Letters* **92**, 015701 (2004); c) G. M. Buendía, P. A. Rikvold, K. Park, M. A. Novotny, *The Journal of Chemical Physics* **121**, 4193 (2004); d) V. A. Shneidman, G. M. Nita, *Physical Review Letters* **89**, 025701 (2002); e) K. Brendel, G. T. Barkema, H. van Beijeren, *Physical Review E* **71**, 031601 (2005); f) R. J. Allen, C. Valeriani, S. Tănase-Nicola, P. R. ten Wolde, D. Frenkel, *The Journal of Chemical Physics* **129**, 134704 (2008); g) W. R. Deskins, G. Brown, S. H. Thompson, P. A. Rikvold, *Physical Review B* **84**, 094431 (2011).

[14] B. J. Kooi, *Physical Review B* **77**, 024303 (2008).

[15] a) P. G. Bolhuis, D. Chandler, C. Dellago, P. L. Geissler, *Annual Review of Physical Chemistry* **53**, 291 (2002); b) W. E, W. Ren, E. Vanden-Eijnden, *Physical Review B* **66**, 052301 (2002); c) W. E, W. Ren, E. Vanden-Eijnden, *The Journal of Physical Chemistry B* **109**, 6688 (2005); d) E. Vanden-Eijnden, *Computer Simulations in Condensed Matter Systems: From Materials to Chemical Biology Volume 1*, M. Ferrario, G. Ciccotti, K. Binder, eds. (Springer Berlin Heidelberg, Berlin, Heidelberg, 2006), vol. 703, pp. 453–493.

[16] E. J. Neves, R. H. Schonmann, *Communications in Mathematical Physics* **137**, 209 (1991).

[17] S. Redner, *Journal of Statistical Physics* **29**, 309 (1982).

[18] S. Mertens, M. E. Lautenbacher, *Journal of Statistical Physics* **66**, 669 (1992).

[19] L. Onsager, *Physical Review* **65**, 117 (1944).

[20] R. Houtappel, *Physica A* **16**, 425 (1950).

[21] R. J. Glauber, *Journal of Mathematical Physics* **4**, 294 (1963).

[22] a) R. A. Ramos, P. A. Rikvold, M. A. Novotny, *Physical Review B* **59**, 9053 (1999); b) B. J. Kooi, *Physical Review B* **73**, 054103 (2006).

[23] J. Hoshen, R. Kopelman, *Physical Review B* **14**, 3438 (1976).

[24] I. Jensen, *Journal of Statistical Physics* **102**, 865 (2001).

[25] M. Vöge, A. J. Guttmann, *Theoretical Computer Science* **307**, 433 (2003).

[26] V. A. Shneidman, K. A. Jackson, K. M. Beatty, *The Journal of Chemical Physics* **111**, 6932 (1999).

[27] V. A. Shneidman, R. K. P. Zia, *Physical Review B* **63**, 085410 (2001).

Summary

In the search for ever faster computers and data storage, memories have played an important role. With the invention of the hard disk, the slow and cumbersome punch cards were replaced. Hard disks have evolved greatly in both storage and transfer speeds since then. The last decade flash memories became of great importance, being faster, solid state and more power efficient, and can now be found in almost all modern handheld electronic devices and computers. However, Flash technology is reaching its limits in both scalability and speed. To be able to continue the search for smaller and faster memories phase-change materials have proven to be interesting candidates for the next-generation memories.

Phase-change materials can exist in two phases: the meta-stable amorphous phase and the stable crystalline phase. These two phases have particularly different electrical and optical properties and such differences can be measured and exploited to create a memory device. Crucial for a memory cell is the ability to rapidly switch between different states. To switch the phase-change material to the crystalline phase from the amorphous phase, a phase-change cell only needs to reach a temperature above the glass transition temperature. This will cause the nucleation and growth of crystals in the amorphous material and the cell will become crystalline. To go from the crystalline phase to the amorphous phase, one has to melt the crystalline phase-change material and rapidly cool it afterwards. In this way the liquid phase will be frozen before the material has time to form crystals and a melt-quenched amorphous state is obtained. The switching in phase-change materials is possible on a nanosecond timescale, which makes these materials very suitable for high-speed memories. For comparison, flash memories typical take microseconds to switch, more than 1000 times slower. Although phase-change materials are already widely used in rewritable discs, much is still unknown about their workings. The goal of this work is to fill in a part of that knowledge gap and to provide a description on how these materials can be studied in a direct way and are responding to external influences.

The material properties determining the usability of phase-change material, like the melting temperature, crystallization temperature and activation energies for nucleation and growth, strongly depend on the composition of the alloy. Commonly used alloys for phase-change materials consist of a combination of antimony, germanium and tellurium, in some cases also doped with silver and/or indium. By changing the composition only slightly with several atom percentages, the crucial properties can change dramatically. Without a good overview on how

these properties develop as function of composition it is difficult to predict if a given phase-change material will be suitable for memory applications. In chapter 3 we studied GeSb films in detail and found that the activation energy for growth increases strongly from 1.7 eV to 6.6 eV when increasing the germanium percentage from 6 at.% to 9 at.%. At the same time, the crystallization temperature increases from about 80 °C for Ge_6Sb_{94} to 200 °C for $Ge_{10}Sb_{90}$. Next to these large changes in growth properties, we also found a change in crystal growth morphology. For Ge_6Sb_{94} and Ge_7Sb_{91} a transrotational dendritic crystal structure is the dominant crystal structure. In Ge_8Sb_{92}, Ge_9Sb_{91} and $Ge_{10}Sb_{90}$ we observed the presence of a second growth morphology. One that is isotropic and has a strong texture and grows with the (0001) plane parallel to the surface. The remarkable finding is that, in a certain temperature range, both morphologies can grow simultaneously, but show very large differences in growth rates and activation energies. For example, in Ge_8Sb_{92} the dendritic growth mode grows ∼100 times faster than the isotropic growth at 150 °C external temperature. The presence of these multiple growth morphologies should be taken into consideration when extrapolating measurement data to, for instance, predict the data retention of a phase-change memory at low temperatures. Differences in latent heat, released during the crystallization by both growth morphologies, are considered responsible for the observed differences in the crystallization kinetics for both morphologies.

Studies of the crystal growth properties often rely on indirect observations, for example, by looking at the heat released or by the change in electrical resistance upon crystallization. Only a few alloys are suitable for optical observation as they have a suitable low nucleation rate, resulting in large crystals over 10 µm in diameter. Using a high speed camera we were able in chapter 4 to optically study the crystal growth in a direct manner at high temperatures with growth rates in the order of cm s^{-1}. Using standard isothermal methods the temperatures needed for these measurements cannot be reached before crystallization occurs. By applying additional laser heating during the experiments we were able to reach higher temperatures and get the desired higher growth rates. At these rates and temperatures we see a strong deviation from the Arrhenius-type behavior previously observed with the standard isothermal measurements. Using a viscosity model for supercooled liquids we were able to model the measured rates and to make a prediction of the crystal growth rates and the maximum rate of about (∼15 m s^{-1}) at temperatures near the melting temperature.

A problem in current phase-change memory devices is the differences in characteristics between memory cells in the same device, while in principle they should be identical. A possible cause of these variations can be found in the presence of differences in local tensile or compressive stresses. Due to the decrease in density when switching from crystalline to amorphous, the embedded phase-change cell is put under a compressive stress (when assuming the

initial state to be stress-free). In chapter 5 we demonstrated that the presence of a compressive stress decreases the crystallization temperature (compared to the stress-free case), which would make a memory cell more prone to unwanted switching back to crystalline. Likewise, we showed that the presence of a tensile stress increases the crystallization temperature resulting in an amorphous phase that is more stable. These stresses do not have to be large to have a strong influence. Moderate compressive stresses of ∼70 MPa already have a large effect on the crystal growth resulting in a ∼50 times faster growth rate, while tensile stresses, induced by differences in thermal expansion coefficients, can increase the crystallization temperature by as much as 20 °C.

One of the important benefits of phase-change material memory devices above currently used Flash memory and DRAM is the possibility to downscale the memory cells to below 10 nm feature sizes without immediately reaching fundamental limits. Current memory technologies start to degrade at these small sizes, where phase-change technology still show improved properties. However, when the cell sizes become smaller, the influence of the amorphous-crystalline boundary increases. In chapter 6 we studied the surface potential across this amorphous-crystalline interface using SSPM. Analysis indicated a surface potential for the crystalline phase with respect to the amorphous phase which is on average 60 mV and always larger than 30 mV. This difference in surface potential is due to the p-type semiconducting behavior of the amorphous phase and the nearly metallic behavior of the crystalline phase. This will result in a Schottky barrier at the amorphous/crystalline interface with the associated potential difference. The presence of this barrier has to be taken carefully into account when downscaling phase-change memories, as it influences the electrical characteristics.

Next to experimental studies on the crystal growth, we computationally studied the initial stage of crystal nucleation in chapter 7. By studying the growth and decay of clusters within a two dimensional Ising model on square and triangular lattices, we were able to determine the critical cluster sizes at low temperatures. This was done by enumerating all unique lattice configurations up to $n = 25$ for the triangular lattice and up to $n = 29$ for the square lattice. From these enumerations the critical cluster sizes as function of temperature and external field were calculated for both lattices using two different thermodynamic definitions. Monte Carlo simulations were performed to calculate the critical cluster size using a kinetic definition. We found that the MC results shows good agreement with the 'average' thermodynamic definition as both simulations are based on averaging not only over the most compact clusters, but are also influenced by growth and decay of neighboring cluster sizes. This shows that describing nucleation in general as based on only a 1D Markov chain is too simplified. However, we did find for all three definitions that the most compact clusters are being favored at low temperatures, in correspondence with the Ising model.

Samenvatting

In de zoektocht naar snellere computers en dataopslag spelen geheugens een belangrijke rol. Met de uitvinding van de harde schijf kon de langzame ponskaart eindelijk vervangen worden. Harde schijven zijn sindsdien vele malen verbeterd op zowel het gebied van opslagcapaciteit als overdrachtssnelheden. De afgelopen tien jaar zijn flashgeheugens sterk in opkomst. Deze zijn sneller, hebben geen bewegende onderdelen en een lager energiegebruik en kunnen in bijna elke moderne smartphone gevonden worden. Helaas bereikt de flashtechnologie zijn limieten op het gebied van schaalbaarheid en snelheid. Om de zoektocht naar snellere geheugens voort te kunnen zetten wordt er gekeken naar andere technologieën. Het gebruik van phase-changematerialen is één van die technologieën die bewezen hebben om interessant te zijn als kandidaat voor de volgende generaties geheugens.

Phase-changematerialen kunnen bestaan in twee verschillende fasen: de meta-stabiele amorfe fase en de stabiele kristallijne fase. Deze twee fasen verschillen, onder andere, in elektrische en optische eigenschappen en zulke verschillen kunnen gemeten en gebruikt worden om een geheugen te maken. Cruciaal voor een geheugencel is dat deze snel kan schakelen tussen de verschillende toestanden. Om een phase-changemateriaal te schakelen van de amorfe fase naar de kristallijne fase is slechts een temperatuur boven de glastemperatuur nodig. Dit zorgt er voor dat kristallen kunnen nucleëren en groeien tot de volledige amorfe fase kristallijn is geworden. Om van de kristallijne fase naar de amorfe fase te gaan moet het phase-changemateriaal gesmolten worden en vervolgens zo snel worden afgekoeld dat de vloeibare fase bevriest voordat er kristallen gevormd kunnen worden. Deze twee schakelmechanismes kunnen beide plaatsvinden op een nanosecondentijdschaal. Dit maakt phase-changematerialen uitermate geschikt voor snelle geheugens. Ter vergelijking, flashgeheugen heeft enkele microseconden nodig om te schakelen. Hoewel phase-changematerialen al veelvuldig worden toegepast in herschrijfbare optische schijven, is er nog veel onbekend over de werking. Het doel van het hier gepresenteerde werk is om deze kennis uit te breiden en een beschrijving te geven over hoe, onder andere, kristalgroei in deze materialen bestudeerd kan worden op een directe wijze en hoe de groei reageert op externe invloeden.

De materiaaleigenschappen die de bruikbaarheid van een phase-changemateriaal bepalen, zoals de smelttemperatuur, kristallisatietemperatuur en activeringsenergieën voor nucleatie en groei, hangen sterk af van de compositie van de phase-changelegering. Veelgebruikte legerin-

gen bestaan uit elementen als antimoon, germanium en tellurium, in sommige gevallen gedoteerd met zilver en/of indium. Door de compositie met slechts enkele atoomprocenten te veranderen kunnen de kritische eigenschappen drastisch veranderen. Zonder een goed overzicht over hoe deze eigenschappen afhangen van de compositie, is het moeilijk om te voorspellen of een bepaald phase-changemateriaal ook geschikt is voor een geheugentoepassing. In hoofdstuk 3 hebben we GeSb films in detail bestudeerd en hier is gevonden dat de activeringsenergie voor groei sterk toeneemt van 1.7 eV naar 6.6 eV wanneer het germaniumpercentage wordt verhoogd van 6 at.% naar 9 at.%. Tegelijk neemt de kristallisatietemperatuur toe van ongeveer 80 °C voor Ge_6Sb_{94} naar 200 °C voor $Ge_{10}Sb_{90}$. Naast het verschil in groeieigenschappen vonden we een verandering in groeimorfologie. In Ge_6Sb_{94} en Ge_7Sb_{93} is een transrotationele/dendritische kristalstructuur de dominante structuur. In Ge_8Sb_{92}, Ge_9Sb_{91} en $Ge_{10}Sb_{90}$ observeerden we de aanwezigheid van een tweede groeimorfologie. Deze is isotroop met een sterke textuur en groeit met het (0001) vlak parallel aan het oppervlak. Het opmerkelijke is dat in een bepaald temperatuursgebied beide morfologieën gelijktijdig aanwezig zijn, maar een groot verschil vertonen in groeisnelheden en activeringsenergieën. Bijvoorbeeld, in Ge_8Sb_{92} groeit de dendritische groei ~100 keer sneller dan de isotrope groei bij een externe temperatuur van 150 °C. De aanwezigheid van meerdere groeimorfologieën kan problematisch zijn bij het extrapoleren van meetresultaten om, bijvoorbeeld, de dataretentie te voorspellen op lage temperaturen. Verschillen in latente warmte, die vrijkomt bij beide kristallisatieprocessen, worden beschouwd als de oorzaak voor de gemeten verschillen tussen beide morfologieën.

Studies naar de kristalgroeieigenschappen zijn vaak gebaseerd op indirecte observatie, bijvoorbeeld door te kijken naar de vrijgekomen latente warmte of de verandering van de elektrische weerstand bij kristallisatie. Slechts enkele legeringen zijn geschikt voor directe optische observatie omdat ze een lage nucleatiesnelheid hebben waardoor kristallen van tientallen micrometers in diameter kunnen ontstaan. Met behulp van een hogesnelheidscamera waren we in hoofdstuk 4 in staat om op een directe wijze kristalgroei optisch te bestuderen op hoge temperaturen en met groeisnelheden in de ordegrootte van cm s^{-1}. Met standaard isotherme methodes zijn deze temperaturen niet te bereiken voordat kristallisatie plaatsvindt. Door gebruik te maken van extra warmtetoevoer met behulp van een laser waren we in staat om het phase-changemateriaal te verhitten tot temperaturen die nodig waren om de hoge groeisnelheden te bereiken. Bij deze temperaturen en groeisnelheden zien we een sterke afwijking van het Arrheniusgedrag dat gemeten was bij isotherme metingen. Met behulp van een model voor de viscositeit van supergekoelde vloeistoffen konden we de gemeten groeisnelheden modelleren en een predictie maken van de maximale groeisnelheid van ~15 m s^{-1} bij temperaturen in de buurt van de smelttemperatuur.

Een probleem bij de huidige phase-changegeheugens is het verschil in karakteristieken tus-

sen verschillende geheugencellen in hetzelfde geheugen, terwijl deze in principe identiek zouden moeten zijn. Een mogelijke oorzaak hiervoor zijn variaties in lokale trek- en drukspanningen. Door de afname in dichtheid bij het schakelen van kristallijn naar amorf komen de ingebedde phase-changecellen onder een drukspanning te staan (wanneer aangenomen wordt dat ze initieel stressvrij zijn). In hoofdstuk 5 demonstreerden we dat door de aanwezigheid van een drukspanning de kristallisatietemperatuur afneemt (in vergelijking met de spanningsvrije toestand). Dit zou een geheugencel gevoeliger maken voor ongewenst terugschakelen naar de kristallijne fase. Soortgelijk toonden we aan dat een trekspanning de kristallisatietemperatuur verhoogd wat resulteert in een stabielere amorfe fase. De spanningen hoeven niet groot te zijn om toch al een sterk effect teweeg te brengen. Matige drukspanningen van ∼70 MPa veroorzaken al een ∼50 keer sneller kristalgroei. Trekspanning als gevolg van verschillen in thermische uitzettingscoëfficiënten kunnen de kristallisatietemperatuur al met 20 °C doen afnemen.

Eén van de belangrijkste voordelen van phase-changegeheugen boven flashgeheugen en DRAM is de mogelijkheid om de individuele phase-changecellen tot onder de 10 nm te schalen zonder meteen fundamentele limieten te bereiken. Huidige geheugentechnologieën vertonen problemen bij deze kleine dimensies, terwijl phase-changetechnologie juist verbeterde eigenschappen vertoont. Echter, als de cel kleiner wordt neemt de invloed van het amorf-kristallijn grensvlak toe. In hoofdstuk 6 bestudeerden we de oppervlaktepotentiaal over dit grensvlak met behulp van Kelvin-sondemicroscopie. Uit de analyse bleek dat er potentiaal op de kristallijne fase staat van gemiddeld ∼60 mV en minimaal ∼30 mV ten opzichte van de amorfe fase. Dit verschil in oppervlakte potentiaal komt door het p-type halfgeleidergedrag van de amorfe fase en het metallische gedrag van de kristallijne fase. Dit resulteert in de aanwezigheid van een Schottky barrière aan het grensvlak met een bijbehorend potentiaalverschil. De aanwezigheid van deze barrière moet in acht worden genomen wanneer phase-changegeheugen nog verder verkleind worden vanwege de invloed op de elektrische eigenschappen.

Naast de experimentele studies aan kristalgroei hebben we de initiële fase van kristalnucleatie bestudeerd met behulp van simulaties in hoofdstuk 7. Door het groei- en vervalgedrag van clusters in een tweedimensionaal Ising model te bestuderen op vierkante en driehoekige roosters, waren we in staat de kritische clustergroottes te bepalen op lage temperaturen. Dit is gedaan door alle unieke roosterconfiguraties te berekenen tot $n = 25$ voor het driehoekige rooster en $n = 29$ voor het vierkante rooster. Met deze resultaten kon de kritische clustergrootte als functie van temperatuur en extern veld berekend worden voor twee verschillende thermodynamische definities. Monte-Carlosimulaties werden gebruikt om kritische clustergroottes te bepalen met behulp van een kinetische definitie. De resultaten van de MC-simulaties komen goed overeen met de 'gemiddelde' thermodynamische definitie. Dit komt doordat beide methoden niet alleen middelen over de meeste compacte clusters, maar ook beïnvloed worden

door groei en verval van naburige clusters. Dit toont aan dat de beschrijving van nucleatie in het algemeen, wanneer gebaseerd op een ééndimensionaal Markovketen, te vereenvoudigd is. We hebben echter wel gevonden dat alle drie definities een voorkeur hebben voor de meest compacte clusters op lagere temperaturen, volledig in overeenstemming met het Ising model.

Dankwoord

Na iets meer dan vier jaar is het dan eindelijk zover, de thesis is af! Tegelijk betekent dit het einde van mijn verblijf in Nijenborgh 4, waar ik de afgelopen jaren veel tijd heb doorgebracht en bijzonder veel geleerd heb. Ik had dit waarschijnlijk niet volgehouden zonder de hulp en aanwezigheid van een groot aantal mensen, en ik ga bij dezen een poging wagen om jullie allemaal te bedanken.

Uiteraard wil ik als eerste Bart bedanken voor het mogelijk maken van de PhD-positie en voor het vertrouwen in mij, dat ik dit tot een goed einde zou brengen. De afgelopen jaren kon ik altijd bij je terecht als ik ergens niet uit kwam en was je altijd bereid om uitleg te geven. Met je kennis van materiaalkunde en kristallografie heb je me erg veel geholpen in het begrijpen en verklaren van de resultaten. Ik ben erg blij met de vrijheid die je me gegeven hebt om het onderzoek in een richting te sturen die mij het meest interessant leek maar stel de suggesties die je gaf voor andere richtingen, die erg nuttig bleken, ook zeer op prijs. Bedankt voor de prettige samenwerking en de mooie resultaten die er uit zijn voortgekomen. Ten tweede wil ik ook graag mijn copromotor George Palasantzas bedanken voor de vele discussies over phase-change, elektronica en politiek. Ook je hulp en kennis bij de AFM en SSPM experimenten waren zeer welkom en hebben mooie resultaten opgeleverd.

I would like to thank the members of the reading committee, Lindsey Greer, Beatriz Noheda and Patrick Onck, for their careful reading of the thesis and providing me with valuable comments. None of this research would have been possible without good samples. Therefore, many thanks go to Andrew Pauza for providing me with many samples with phase-change films of the highest quality. I also like to thank Graeme Blake for performing and analyzing XRD measurements on such a short notice. Dirk Gravesteijn wil ik bedanken voor zijn interesse in mijn onderzoek en zijn input vanuit NXP. Verder wil ik Patrick Onck ook bedanken voor de nuttige discussies die we hebben gehad om de invloed van spanningen te begrijpen.

Special thanks go to my paranymphs Orcun en Martijn. Both of you greatly helped me having a good time in Groningen, and with great joy I think back at our joint activities. Orcun, it was a pleasure of working together with you during the last four years and I would like to thank you for your everyday company at the faculty and making late night and weekend experiments loads of fun. Martijn, heel erg bedankt voor je steun de afgelopen jaren, door mij in veel activiteiten te betrekken heb je me veel plezier bezorgd in Groningen. Ook wil ik je bedanken

voor de goede comics, films en muziek die je altijd weet aan te raden.

Natuurlijk wil ik iedereen van onze vakgroep bedanken voor de fijne samenwerking, leuke groepsuitjes, etentjes en gezellige theepauzes. Gert ten Brink wil graag bedanken voor de hulp bij het gebruik van de SEM, de thee om 3 uur, bij vlagen goede ideeën en het altijd daar zijn als je iemand nodig had om tegen aan te schreeuwen. Klaas Bernd voor het doen van vele, vele metingen aan GaSb, Arno voor de AFM en SSPM-metingen, Tobias voor het uitvoeren en analyseren van de lasermetingen, Jasper voor je phase-changekennis, elektronicaskills en de mooie tripjes naar VS. Uiteraard ook de overige leden van de vakgroep: Peter, Rudy, Gopi, Almendo, Robin, Jarda, Jan-Willem, Arjan, Floorke, Machteld, Bart-Jan, Paul, Mehdi, Jamo, Jan en Nolan; bedankt voor de heerlijke gesprekken tijdens de theepauze.

Veel tijd ben ik (gelukkig) kwijt geraakt aan de mooie gekken van T.F.V. 'Professor Francken'. Tijdens mijn studie en promotie heb ik dankzij jullie de nodige ontspanning kunnen vinden in de Franckenkamer. Speciale dank gaat uit naar Detsi, Boon, Ypke, Kathinka, LJ, KB, Edwin, Tobias, Jan-Willem, Peter, Guus, Paul, Rudy, Henk, Ernst, Djim, Sjoerd, Sjieuwe, Jenny, Rens, Irina, Anouk, Paulus, Sven, Blok, Onur, Marten, Thom, Carlos, Hilbert, Anne, Remco, Steven, Tom, Compaijen, Mannold, Thijs, Pelle, Mark, Jakko, Bijl, Boerma, Susan, Bosch, Jabs, Kamerbeek, Victor. Château! Ook buiten de universiteit is er goed geborreld en daarom wil ik, onder andere, Marnix, James, Manasa, Emi, Suzanne, Barbara, Amarins, Jonathan, Hande, Can en Mario bedanken voor de gezellige vrijdagmiddagen en -avonden.

Naast hard werken en drinken is er ook nog af en toe gesport. Ik wil LJ bedanken voor het geniale idee om ons aan te melden bij TJAS, en bedank de leden van Groepje Rood voor de leuke uren op en naast de ijsbaan. Bedankt Jantine, Carolien, Joos (ook voor de zeer gewaardeerde bijdragen voor hoofdstuk 4), Reys en Nienke voor het gezelschap voor, tijdens en na het schaatsen en fietsen.

Graag bedank ik mijn vrienden van thuis thuis voor de vele leuke weekenden die we keer op keer hebben, zelfs nu we door het hele land verspreid zijn: Marten, Jeroen, Willem, Wicher, Anemoon, Jasmijn, Mark. Uiteraard ook Simone voor de goede tijd die we samen hebben gehad.

I would also like to gratefully acknowledge Beata for always being there when a talk, ranging from dead serious to plain ridiculous, was needed. Somehow you always manage to make me smile, which is awesome.

Als laatste wil mijn familie bedanken voor de steun die ze mij altijd hebben gegeven. In het bijzonder pa, ma, Linda en Alex. Jullie hebben mij een prachtige omgeving gegeven om in op te groeien en hebben mij altijd gestimuleerd om door te blijven leren, waarvoor ik jullie erg dankbaar ben. Ik vind het geweldig dat ik altijd op jullie kan rekenen als dat nodig is.

Gert

List of publications

- G. Eising and B. J. Kooi, *Cluster evolution and critical cluster sizes for the square and triangular lattice Ising models using lattice animals and Monte Carlo simulations*, Physical Review B **85**, 214108 (2012).
  DOI: 10.1103/PhysRevB.85.214108.

- H. J. Kroezen, G. Eising, G. ten Brink, G. Palasantzas, B. J. Kooi, and A. Pauza, *Schottky barrier formation at amorphous-crystalline interfaces of GeSb phase change materials*, Applied Physics Letters **100**, 094106 (2012).
  DOI: 10.1063/1.3691179.

- G. Eising, A. Pauza and B. J. Kooi, *Stress-Induced Crystallization of Ge-Doped Sb Phase-Change Thin Films*, Crystal Growth & Design **13**, 220 (2013).
  DOI: 10.1021/cg3013848.

- G. Eising, B. Niebuur, A Pauza and B. J. Kooi, *Competing Crystal Growth in Ge-Sb Phase-Change Films*, Advanced Functional Materials, (2013).
  DOI: 10.1002/adfm.201301242

- G. Eising, T. Van Damme, A Pauza and B. J. Kooi, *Laser Accelerated Isothermal Crystal Growth in Ge-Sb Phase-Change Films*, in preparation.